Matthias Peter Maria Gruber, BSc

Non-equilibrium particle and thermal energy transport in one-dimensional quantum lattice systems

MASTER'S THESIS

to achieve the university degree of

Diplom-Ingenieur

Master's degree programme: Technical Physics

submitted to

Graz University of Technology

Supervisor:
Ao.Univ.-Prof. Dipl.-Phys. Dr.rer.nat. Hans Gerd Evertz

Institute of Theoretical and Computational Physics

Graz, November 2017

To Mama and Papa.

ABSTRACT

In this thesis, particle and thermal energy transport in one-dimensional systems are studied. At first, particle transport through tight-binding and Hubbard chains is considered. The particle current is initiated by coupling an empty and a filled bath to the initially half-filled chain. Due to different fillings in the baths, a particle current emerges and eventually reaches a steady state current. To model the bath spectral function, star and Wilson chain geometries are applied and compared, especially with respect to the growth of the von Neumann entanglement entropy throughout the whole system. In both cases, a linearly growing entanglement entropy is observed.

Furthermore, thermal energy currents through tight-binding and Hubbard chains are studied. Thermal baths in star geometry, obtained through a thermofield approach and initialized at different temperatures, are coupled onto the chains in order to induce a thermal energy current. After a thermalization of the system, the thermal energy current also reaches a steady state. The dependence of this steady state on the temperatures of the two baths is studied as well as the convergence towards this steady state. Steady state currents depending on the temperatures of the left and right bath in the form of $j_E = f(T_L) - f(T_R)$ are observed. In the case of Hubbard chains, the thermalization time is longer than the maximum simulation time which is limited by exponentially increasing bond dimensions.

The time evolution of the systems is performed by applying Time-Evolving Block Decimation (TEBD) as well as the one- and two-site Time-Dependent Variational Principle (TDVP) in the context of Matrix Product States (MPS). It turns out that TDVP needs somewhat smaller matrix bond dimensions but also an order of magnitude more computation time for accurately capturing steady state energy currents. In a recent paper, local observables in an Ising chain at high temperature were accurately described after a local perturbation by applying TDVP time evolution at small bond dimensions. However, the present thesis finds that for accurately capturing a steady state current, small bond dimensions on the order of $\chi = 10$ are insufficient. Generally, the exponential growth of matrix bond dimensions and the linear growth of entanglement, respectively, limit the maximum simulation time.

Zusammenfassung

Diese Masterarbeit behandelt den Teilchentransport sowie den Energietransport in eindimensionalen Systemen. Zuerst wird der Teilchentransport in Tight-binding-Ketten sowie Hubbard-Ketten untersucht. Dieser Teilchenstrom wird durch eine unterschiedliche Besetzung der Bäder ausgelöst, die links und rechts an die, im Anfangszustand halbgefüllte, Kette gekoppelt werden. Durch die unterschiedliche Besetzung der Bäder beginnt ein Strom zu fließen, der schlussendlich einen Gleichgewichtszustand (Steady State) erreicht. Die Badspektralfunktionen werden mit Hilfe von Wilson Ketten oder Sterngeometrien modelliert. Diese beiden Geometrien werden miteinander verglichen, insbesondere im Hinblick auf das Wachstum der Entropie im ganzen System. In beiden Fällen kann ein lineares Wachstum der Entropie beobachtet werden.

Weiters wird auch ein Energiestrom in Form eines Wärmestroms durch Tight-binding und Hubbard-Ketten untersucht. Die hierfür notwendigen thermischen Bäder haben eine Sterngeometrie und werden mit Hilfe eines Thermofield-Ansatzes mit einer endlichen Temperatur simuliert und dann links und rechts an die Kette angekoppelt. Durch die unterschiedliche Temperatur der beiden thermischen Bäder beginnt dann ein Wärmestrom zu fließen. Nachdem sich das System thermalisiert, kann auch bei diesem Wärmestrom ein Steady State Wert erreicht werden. Untersucht wird die Abhängigkeit dieses Wertes von den Temperaturen der Bäder und auch, wie schnell dieser Steady State erreicht werden kann. Es stellt sich heraus, dass der Wert des Gleichgewichtsstroms von den Temperaturen des linken und rechten Bades in der Form $j_E = f(T_L) - f(T_R)$ abhängt. In Hubbard-Ketten ist die Thermalisierungszeit länger als die maximale Simulationszeit, weswegen kein Steady State erreicht werden kann. Die Simulationszeit wird durch das exponentielle Wachstum der maximalen Matrixdimensionen begrenzt.

Die Zeitentwicklung der Systeme wird mit Hilfe des Time-Evolving Block Decimation (TEBD) Algorithmus bzw. mit dem Ein- und Zweiplatz Time-Dependent Variational Principle (TDVP) durchgeführt, wobei beide Algorithmen unter Verwendung von Matrixproduktzuständen (MPS) implementiert werden. Es stellt sich heraus, dass der TDVP Algorithmus mit kleineren Matrixgrößen auskommt, aber auch um eine Größenordnung längere Zeiten für die Berechnung benötigt, um den Steady State Strom genau simulieren zu können. In einem kürzlich erschienenen Paper konnten lokale Observablen, in einer Ising-Kette bei hoher Temperatur, nach einer lokalen Störung bei Zeitentwicklung mit TDVP bei kleinen Matrixdimensionen korrekt dargestellt werden. Die vorliegende Arbeit kommt allerdings zu dem Schluss, dass kleine Matrixdimensionen der Größenordnung $\chi = 10$ nicht in der Lage sind, einen Steady State Wärmestrom korrekt darzustellen. Generell kann beobachtet werden, dass die Matrixdimensionen bei der Zeitentwicklung exponentiell anwachsen bzw. die Entropie linear anwächst, was die maximal mögliche Simulationszeit begrenzt.

Contents

1   Introduction

This thesis deals with non-equilibrium particle and energy transport in one-dimensional systems. Both tight-binding chains as well as Hubbard chains are investigated. These chains are then coupled to baths in order to induce a current.

Although an exact representation of the system in the Hilbert space would need matrix bond dimensions of sizes up to $d^{N/2}$ for a system with N sites and local Hilbert dimension d, the physics of one-dimensional systems can actually be captured accurately with matrix bond dimensions orders of magnitude smaller than $d^{N/2}$. This is possible because the Singular Value Decomposition (SVD) of the matrices of the Matrix Product States (MPS) yields quickly decreasing singular values, making it sufficient to keep the matrix bond dimensions at reasonable sizes which can be simulated numerically.[1] Thus, the concept of MPS constitutes a powerful tool for the simulation of one-dimensional systems.

This thesis investigates both particle and thermal energy currents in one-dimensional systems. In the case of particle current, the current can be induced by an initial difference in occupation numbers between the two baths which causes the particles to flow into the emptier parts and finally reach a steady state current. Alternatively, a bias voltage between the two baths can also be applied to induce a current. In the case of thermal energy current, the current can be induced by coupling thermal baths at different temperatures onto the chain. In the present thesis, the thermal baths were obtained through the concept of a thermofield approach[2] as an alternative to the commonly applied method of purification.[1]

Beside particle and energy currents, the von Neumann entanglement entropy is also studied in this thesis. The entanglement entropy can be obtained easily in the context of MPS from the singular values and is a measure of the entanglement between two subsystems of the whole system. In the context of MPS, the entanglement entropy is of special interest as it is related to the bond dimensions: When the entropy takes its maximum value, it is given by $S_{max} = \ln(\chi)$ which means that a linearly increasing entropy causes exponentially growing bond dimensions χ. In the case of quadratic matrices, the computational cost of an SVD is of order χ^3 and therefore, the exponential growth of bond dimensions constitutes the major limitation of the possible simulation time for the systems discussed in this thesis.

To perform the time evolution of the systems introduced above, two different time evolution algorithms are used in the context of MPS: The Time-Evolving Block Decimation (TEBD) algorithm[3] and the Time-Dependent Variational Principle (TDVP)[4]. In the case of TDVP, a one-site and a two-site algorithm are applied. All three algorithms are used to simulate thermal energy currents in chains and their ability to accurately capture the expected steady state currents with respect to different maximum bond dimensions. TDVP algorithms are expected to need smaller bond dimensions as the algorithm guarantees an optimal representation of an arbitrary state for a given bond dimension.

Chapter 2 of this thesis introduces the Heisenberg and the Hubbard model, which were

applied in one dimension. In chapter 3.1, the concept of Matrix Product States is introduced. In chapters 3.2 and 3.3, the concepts of entanglement entropy and DMRG are discussed in the context of MPS. In chapters 3.4 and 3.5, the time evolving algorithms TEBD and TDVP are introduced and in chapter 3.6, the star geometry as well as the Wilson chain geometry, which were both used to simulate the baths, are explained. Chapters 4 and 5 discuss the concepts of particle and thermal currents in one-dimensional systems. In chapters 4.2 and 5.4, results for particle and thermal currents in one-dimensional chains are shown. Furthermore, all results regarding the entanglement growth and convergence properties of the systems can be found in these chapters. Finally, in chapter 6 the different time evolution algorithms TEBD and TDVP are compared, especially with respect to their ability of accurately capturing the steady state currents for given bond dimensions.

2 Models

In all the formulas in this thesis, atomic units are used i.e.

$$\hbar = m_e = (4\pi\epsilon_0)^{-1} = e = 1$$

2.1 The Heisenberg model

Introductions on the Heisenberg model can be found in references [5–7]. This introduction mainly follows the book by Baxter[5].
The Heisenberg model for a spin $1/2$ chain with N sites is given by the following Hamiltonian:

$$H = -\frac{1}{2}J\sum_{j=1}^{N}\left(\sigma_j^x\sigma_{j+1}^x + \sigma_j^y\sigma_{j+1}^y + \sigma_j^z\sigma_{j+1}^z\right) \tag{1}$$

where J is a constant and σ_j^x, σ_j^y and σ_j^z are the Pauli matrices acting on site j.
If $J > 0$, the energy will be minimized if two neighbouring spins are pointing in different directions. This means that $J > 0$ favours antiferromagnetic order. In the case of $J < 0$, the energy will be minimized if the spins align parallel and therefore the ferromagnetic state is favoured.
The Pauli spin matrices and the unity matrix e are given by

$$e = \begin{pmatrix} 1 & 0 \\ 0 & 1 \end{pmatrix}, \quad \sigma^x = \begin{pmatrix} 0 & 1 \\ 1 & 0 \end{pmatrix}, \quad \sigma^y = \begin{pmatrix} 0 & -i \\ i & 0 \end{pmatrix}, \quad \sigma^z = \begin{pmatrix} 1 & 0 \\ 0 & -1 \end{pmatrix} \tag{2}$$

In direct product notation, where there are N products in each term as the chain has N sites, this gives

$$\begin{aligned}
\sigma_j^x &= e \otimes \cdots \otimes e \otimes \sigma^x \otimes e \otimes \cdots \otimes e \\
\sigma_j^y &= e \otimes \cdots \otimes e \otimes \sigma^y \otimes e \otimes \cdots \otimes e \\
\sigma_j^z &= e \otimes \cdots \otimes e \otimes \sigma^z \otimes e \otimes \cdots \otimes e
\end{aligned} \tag{3}$$

The matrices σ^x, σ^y and σ^z in the equation above appear on site j.
As the Pauli spin matrices are 2×2 matrices, the Hilbert space of the Hamiltonian has dimension 2^N. The Heisenberg model can be seen as a special case of the XYZ model

$$H = -\frac{1}{2}\sum_{j=1}^{N}\left(J_x\sigma_j^x\sigma_{j+1}^x + J_y\sigma_j^y\sigma_{j+1}^y + J_z\sigma_j^z\sigma_{j+1}^z\right) \tag{4}$$

if $J_x = J_y = J_z = J$. Another common representation of the XYZ model uses the matrices

$$S^x = \frac{\sigma^x}{2}, \quad S^y = \frac{\sigma^y}{2}, \quad S^z = \frac{\sigma^z}{2} \tag{5}$$

which fulfil the commutation relation

3

$$\left[S^\alpha, S^\beta \right] = i\epsilon_{\alpha\beta\gamma} S^\gamma \tag{6}$$

A further special case is $J_x = J_y = 0$. In this case, the Hamiltonian H is diagonal and the model reduces to the nearest-neighbour Ising model which can be solved easily. In the case of $J = J_x = J_y \neq J_z = \Delta$, this is the XXZ model. Analogously, the Heisenberg model can be called XXX model and the case of $J_z = 0$ is known as the XY model.

The XY model is related to the Ising model and for finite N, all the eigenvalues can be obtained. This was done by Lieb et al. (1961) and Katsura (1962). The eigenvectors of the XXZ model were given by Bethe in 1931, later in 1966, the Bethe ansatz was proved rigorously by Yang and Yang.

Actually, Bethe's work from 1931 on spin 1/2 Heisenberg chains was the beginning of the history of exactly solvable many-body quantum systems. He was able to reduce the problem of calculating the spectrum of the Hamiltonian to the problem of solving a set of N coupled algebraic equations, the so-called Bethe ansatz equations, where N denotes the number of overturned spins.

2.2 Physical properties of the Heisenberg model

Let us now consider the physical properties which can be simulated with spin 1/2 chains. An overview can e.g. be found in [6] or [8], which this section closely follows.

The Hamiltonian of the physically interesting XXZ model is given by

$$H = \sum_i J_{xy} \left(S_i^x S_{i+1}^x + S_i^y S_{i+1}^y \right) + J_z S_i^z S_{i+1}^z \tag{7}$$

The fact that $J_x = J_y = J_{xy}$ constitutes a rotational symmetry in the xy plane of the system. In the case of the Heisenberg Hamiltonian (see eq. 1), the interaction is completely invariant by rotation. For the XXZ Hamiltonian given in eq. 7, several regimes can be found by making some symmetry considerations: As the Hamiltonian only has interaction between nearest neighbours, one could try to change the interaction from J to $-J$ by changing every other spin from S to $-S$. However, this would only work for classical spins, in the case of quantum spins, this would violate the commutation relations given in eq. 6. The transformations

$$\begin{aligned} S_i^x &\to (-1)^i S_i^x \\ S_i^y &\to (-1)^i S_i^y \\ S_i^z &\to S_i^z \end{aligned} \tag{8}$$

respect these commutation relations but also change J_{xy} to $-J_{xy}$ while J_z remains unchanged. Thus, it is sufficient to only consider $J_{xy} > 0$ and one can identify the following regimes which are determined by the ratio J_z/J_{xy}:

At $J_z = J_{xy}$, there is the antiferromagnetic isotropic point and at $J_z = -J_{xy}$, there is the ferromagnetic isotropic point. For the regimes $J_z/J_{xy} < -1$ and $J_z/J_{xy} > 1$, one gets an Ising ferromagnetic state and an Ising antiferromagnetic state, respectively. The

regime between these two states is called XY, the point $J_z = 0$ is called the pure XY point. Furthermore, the interactions between the spins and a finite magnetic field can be studied by adding a magnetic field H_m in the z direction:

$$H_m = -g\mu_B h \sum_i g\mu_B H S_i^z \tag{9}$$

where h is the magnetic field.

The Heisenberg model works very well for describing magnetic isolators. In isolators, the magnetism is caused by localized magnetic moments in incomplete electron shells ($3d$, $4d$, $4f$ or $5f$). Examples include Ferromagnets, Antiferromagnets and Ferrimagnets. Each of those localized magnetic moments is connected with an angular momentum. The exchange interaction between those magnetic moments can be formulated as an exchange interaction between the respective spins. Thus, the constant J in the Heisenberg model is called the exchange integral. The exchange between the spins simulates the contribution of the matrix elements of the exchange integral of the Coulomb repulsion, which are considered to cause spontaneous magnetization. Although the Heisenberg model describes magnetic isolators very good, it is unable to correctly describe magnetic metals.

2.3 The Hubbard model

Introductions to the Hubbard model can for example be found in references [7] and [8], which this section closely follows.

The Hubbard model is given by:

$$H = \sum_{ij\sigma} t_{ij} c_{i\sigma}^\dagger c_{j\sigma} + U \sum_{i\sigma} n_{i\sigma} n_{i\bar{\sigma}} \tag{10}$$

where $\sigma = \uparrow (\downarrow)$ and $\bar{\sigma} = \downarrow (\uparrow)$. t_{ij} denotes the hopping integral between sites i and j and U is the on-site Coulomb repulsion. $c_{i\sigma}^\dagger$ ($c_{i\sigma}$) creates (annihilates) an electron with spin σ centred on site i and $n_{i\sigma}$ is the number operator given by $n_{i\sigma} = c_{i\sigma}^\dagger c_{i\sigma}$.

In the case of one dimension, a Hubbard chain is considered and the hopping described by the hopping integral t_{ij} can only happen between neighbouring sites on the chain. The one-dimensional Hubbard model on a chain therefore reads

$$H = -\sum_{i\sigma} t_{i,i+1} \left(c_{i\sigma}^\dagger c_{i+1\sigma} + c_{i+1\sigma}^\dagger c_{i\sigma} \right) + U \sum_{i\sigma} n_{i\sigma} n_{i\bar{\sigma}} \tag{11}$$

For $U = 0$, we obtain the tight-binding model which only consists of the kinetic term of the Hubbard Hamiltonian. For a one-dimensional tight-binding chain, the Hamiltonian reads:

$$H = -\sum_{i\sigma} t_{i,i+1} \left(c_{i\sigma}^\dagger c_{i+1\sigma} + c_{i+1\sigma}^\dagger c_{i\sigma} \right) \tag{12}$$

In the simplest case, the hopping integral is the same for all sites i.e. $t_{ij} = t$.

The Hubbard model allows to study the interaction of kinetic energy, Coulomb repulsion, the Pauli principle and lattice structures. Therefore, it is used to study topics like electronic properties of transition metals, Mott transitions or high temperature superconductors.

In 1968, Lieb and Wu discovered that the Bethe ansatz can also be applied to the one-dimensional Hubbard model. By applying Bethe's ansatz, the spectral problem of the Hamiltonian can be reduced to solving a set of algebraic equations, which are nowadays known as the Lieb-Wu equations. In 1972, Takahashi derived integral equations which allowed to determine the Gibbs free energy of the Hubbard model. These integral equations are known as the thermodynamic Bethe ansatz (TBA).

2.4   Physical properties of the Hubbard model

This section closely follows the introduction by Essler et al. in [7].

The Hubbard model was introduced by John Hubbard in order to be able to describe electronic correlations in narrow energy bands and also proposed approximations to model the associated many-body problems.

Consider a three-dimensional solid, consisting of ions and electrons in a crystalline structure. As the ions are much heavier than the electrons, the ions can be described as a static lattice in which the electrons are moving. The dynamics of the electrons are then described by

$$H = \sum_{i=1}^{N} \left(\frac{p_i^2}{2m} + V_I(x_i) \right) + \sum_{1 \leq i < j \leq N} V_C(x_i - x_j) \tag{13}$$

where N is the number of electrons moving in the periodic potential of the ions $V_I(x)$ and the potential of the Coulomb repulsion between the electrons

$$V_C(\mathbf{x}) = \frac{e^2}{\|x\|} \tag{14}$$

Although this model already includes major simplifications, it is still way too complicated to be solved exactly. Therefore, further simplifications have to be applied. One approach is the mean-field approach in which one considers a single particle in an auxiliary potential $V_A(x)$. This contribution is added to the ionic potential $V_I(x)$ in eq. 13 and is then subtracted again in the two-body part $V_C(x_i - x_j)$. After imposing these approximations, the new Hamiltonian gets "second-quantized" in a suitable basis. As the potential is periodic, the eigenfunctions of the one-particle Hamiltonian have Bloch form. Through a Fourier transformation, Wannier functions can be obtained from the Bloch functions. A further transformation expresses the Wannier functions as creation and annihilation operators. All these transformations finally lead to an expression of the Hamiltonian in eq. 13 in second quantized form in the basis of the Wannier functions:

$$H = \sum_{\alpha,i,j,a} t_{ij}^{\alpha} c_{\alpha i,a}^{\dagger} c_{\alpha j,a} + \frac{1}{2} \sum_{\substack{\alpha,\beta,\gamma,\delta \\ i,j,k,l}} \sum_{a,b} U_{ijkl}^{\alpha\beta\gamma\delta} c_{\alpha i,a}^{\dagger} c_{\beta j,b}^{\dagger} c_{\gamma k,b} c_{\delta l,a} \tag{15}$$

where a, b are spin indices, $\alpha, \beta, \gamma, \delta$ are band indices and i, j, k, l are site indices. The hopping matrix is given by t_{ij}^{α} and $U_{ijkl}^{\alpha\beta\gamma\delta}$ denotes the Coulomb interaction, expressed by overlap integrals. Notably, eq. 15 is completely equivalent to eq. 13. Now, the influence of the mutual Coulomb interaction can be minimized by an optimal choice of the auxiliary potential $V_A(x)$. If the interactions are small compared to the hopping matrix elements, they can be set to zero in a first approximation. They can then be considered by perturbation theory within the band theory.

However, when the interaction is not negligible, the Hubbard model is obtained. The case of an intra-atomic Coulomb interaction $U_{iiii}^{\alpha\beta\gamma\delta}$ which is large compared to inter-atomic interaction but not very small compared to the hopping matrix elements is considered to be characteristic for transition and rare earth metals. In situations where the interband interactions are weak and all other bands except e.g. the band $\alpha = 1$ are far away from the Fermi level, then one can replace the actual multi-band Hamiltonian in eq. 15 by a one-band model with effective parameters t_{ij} and U as presented in eq. 10. The hopping matrix elements can be calculated by applying DFT whereas the interaction parameter U is more difficult to calculate and can e.g. be obtained from comparison with an experiment. Although one cannot expect quantitatively correct answers, this model is still able to qualitatively capture some of the electronic features of transition metals.

A further simplification is to assume that the Wannier functions are strongly localized around their respective sites. This so-called tight-binding approximation restricts the hopping matrix to hopping elements between neighbouring sites i.e. only elements of t_{ij} where i and j are neighbouring sites are non-zero.

The previously mentioned band theory is one of the most successful descriptions of electrons in solids. The Hubbard model constitutes the simplest generalization beyond the band theory description of solids but is still capable of describing the gross physical features of systems such as the electronic properties of solids with narrow bands, band magnetism in iron, cobalt and nickel, the Mott metal-insulator transition as well as electronic properties of high-T_C cuprates in the normal state. In general, the Hubbard model can not be solved exactly. However, many properties are calculable in the cases of lattice coordination numbers two and infinity. The first case corresponds to the one-dimensional Hubbard model which is integrable, meaning that many physical properties can be determined exactly. In general, integrable models are rare and mostly occur in one-dimensional systems. Integrable models allow us to understand and characterize many-body physics without having to apply perturbation theory or other approximations. Furthermore, they can also be used as benchmarks for numerical methods.

3   Methods

3.1   Matrix Product States

Matrix Product States (MPS) were used to perform all the calculations presented in this thesis[1]. This section introduces the MPS formalism and closely follows [1].

Let us consider a chain with L sites. Each site has a local spin σ_i. In case of a tight-binding chain, the local dimension $d = 2$:

$$|\sigma_i\rangle = \{|0\rangle, |\uparrow\rangle\} \tag{16}$$

leading to a Hilbert Space with dimension 2^L. In the case of a Hubbard chain, the local dimension $d = 4$:

$$|\sigma_i\rangle = \{|0\rangle, |\downarrow\rangle, |\uparrow\rangle, |\uparrow\downarrow\rangle\} \tag{17}$$

leading to a Hilbert Space with dimension 4^L. The most general pure quantum state on the chain is then given by

$$|\Psi\rangle = \sum_{\sigma_1 \ldots \sigma_L} c_{\sigma_1 \ldots \sigma_L} |\sigma_1, \ldots, \sigma_L\rangle \tag{18}$$

Now we have to introduce the concept of Singular Value Decomposition (SVD).

An SVD guarantees the existence of the decomposition

$$M = USV^{\dagger} \tag{19}$$

where M is an arbitrary matrix of dimensions $(N_A * N_B)$ and

- **U** is of dimension $(N_A * min(N_A, N_B))$ and fulfils $U^{\dagger}U = \mathbb{1}$

- **S** is of dimension $(min(N_A, N_B) * min(N_A, N_B))$ and is a diagonal matrix with the singular values on the diagonal. The singular values s_i are always non-negative and can be chosen so that $s_1 \geq s_2 \geq \cdots \geq s_r > 0$ where s_r is the smallest non-zero singular value. The number of non-zero singular values r is called the Schmidt rank of the matrix.

- **V**† is of dimension $(min(N_A, N_B) * N_B)$ and fulfils $V^{\dagger}V = \mathbb{1}$

The SVD can then be used to perform the Schmidt decomposition of a general quantum state. Any pure state can be written as

$$|\Psi\rangle = \sum_{ij} \Psi_{ij} |i\rangle_A |j\rangle_B \tag{20}$$

where $\{|i\rangle_A\}$ and $\{|j\rangle_B\}$ are orthonormal bases of A and B with dimensions N_A and N_B. Ψ_{ij} can now be considered as a coefficient matrix on which we can perform an SVD:

---

[1]Calculations were performed using the ITensor C++ library (version 1.2), http://itensor.org/

$$|\Psi\rangle = \sum_{ij} \sum_{a=1}^{\chi} U_{ia} S_{aa} V_{ja}^{\star} |i\rangle_A |j\rangle_B \tag{21}$$

where $\chi = min(N_A, N_B)$. Using eq. 21 we can now perform a basis transformation:

$$
\begin{aligned}
|\Psi\rangle &= \sum_{ij} \sum_{a=1}^{\chi} U_{ia} S_{aa} V_{ja}^{\star} |i\rangle_A |j\rangle_B \\
&= \sum_{a=1}^{\chi} \underbrace{S_{aa}}_{\lambda_a} \underbrace{\sum_i U_{ia} |i\rangle_A}_{|a\rangle_A} \underbrace{\sum_j V_{ja}^{\star} |j\rangle_B}_{|a\rangle_B}
\end{aligned}
\tag{22}
$$

$$|\Psi\rangle = \sum_{a=1}^{\chi} \lambda_a |a\rangle_A |a\rangle_B$$

It is sufficient to run the sum over all non-zero singular values up to $r \leq \chi$ and obtain the so-called Schmidt decomposition:

$$|\Psi\rangle = \sum_{a=1}^{r} \lambda_a |a\rangle_A |a\rangle_B \tag{23}$$

The form of the Schmidt decomposition makes it very easy to obtain the reduced density matrices:

$$\hat{\rho}_A = \sum_{a=1}^{r} \lambda_a^2 |a\rangle_A {}_A\langle a| \quad \hat{\rho}_B = \sum_{a=1}^{r} \lambda_a^2 |a\rangle_B {}_B\langle a| \tag{24}$$

The von Neumann entropy of entanglement (SvN) can now be read off directly from the SVD:

$$S_{AB}(|\Psi\rangle) = -Tr(\hat{\rho}_A \log \hat{\rho}_A) = -\sum_{a=1}^{r} \lambda_a^2 \log \lambda_a^2 \tag{25}$$

Furthermore, the SVD can now be used to decompose an arbitrary quantum state into an MPS. Starting from eq. 18, we modify the coefficient vector $c_{\sigma_1 \dots \sigma_L}$ of size d^L by reshaping it into a matrix of size $(d * d^{L-1})$:

$$\Psi_{\sigma_1,(\sigma_2 \dots \sigma_L)} = c_{\sigma_1, \dots, \sigma_L} \tag{26}$$

We can now apply an SVD on this expression:

$$\Psi_{\sigma_1,(\sigma_2, \dots, \sigma_L)} = \sum_{a_1}^{r_1} U_{\sigma_1, a_1} S_{a_1, a_1} (V^{\dagger})_{a_1,(\sigma_2, \dots, \sigma_L)} \equiv \sum_{a_1}^{r_1} U_{\sigma_1, a_1} c_{a_1 \sigma_2, \dots \sigma_L} \tag{27}$$

where we have multiplied S with $V^{\dagger}$ and reshaped it back into a vector.
U can now be decomposed into a collection of d row vectors A^{σ_1} with entries $A_{a_1}^{\sigma_1} = U_{\sigma_1, a_1}$.

Also, $c_{a_1\sigma_2,\ldots\sigma_L}$ is reshaped into a matrix $\Psi_{(a_1\sigma_2),(\sigma_3\ldots\sigma_L)}$ of dimension $(r_1 d * d^{L-2})$ leading to

$$c_{\sigma_1\ldots\sigma_L} = \sum_{a_1}^{r_1} A_{a_1}^{\sigma_1} \Psi_{(a_1\sigma_2),(\sigma_3\ldots\sigma_L)} \tag{28}$$

Another SVD of $\Psi_{(a_1\sigma_2),(\sigma_3\ldots\sigma_L)}$ and similar steps lead to

$$c_{\sigma_1\ldots\sigma_L} = \sum_{a_1}^{r_1}\sum_{a_2}^{r_2} A_{a_1}^{\sigma_1} A_{a_1,a_2}^{\sigma_2} \Psi_{(a_2\sigma_3),(\sigma_4\ldots\sigma_L)} \tag{29}$$

Subsequent application of singular value decompositions finally leads to

$$c_{\sigma_1\ldots\sigma_L} = \sum_{a_1,\ldots,a_{L-1}} A_{a_1}^{\sigma_1} A_{a_1,a_2}^{\sigma_2} \ldots A_{a_{L-2},a_{L-1}}^{\sigma_{L-1}} A_{a_{L-1}}^{\sigma_L} \tag{30}$$

Now we can write the coefficient vector as a product of matrices:

$$c_{\sigma_1\ldots\sigma_L} = A^{\sigma_1} A^{\sigma_2} \ldots A^{\sigma_{L-1}} A^{\sigma_L} \tag{31}$$

By plugging eq. 31 into eq. 18, we finally obtain an exact representation of the arbitrary quantum state as a Matrix Product State:

$$|\Psi\rangle = \sum_{\sigma_1\ldots\sigma_L} A^{\sigma_1} A^{\sigma_2} \ldots A^{\sigma_{L-1}} A^{\sigma_L} |\sigma_1,\ldots,\sigma_L\rangle \tag{32}$$

The dimensions of the A matrices can maximally have the following dimensions:

$$(1 * d), (d * d^2), \ldots, (d^{L/2-1} * d^{L/2}), (d^{L/2} * d^{L/2-1}), \ldots, (d^2 * d), (d * 1) \tag{33}$$

starting with a $(1 * d)$ vector at the first site and ending with a $(d * 1)$ vector at the last site. As one can see, for practical systems, an exact representation would be impossible as the matrix dimensions would blow up exponentially. Therefore, in practical simulations, the maximum bond dimension is significantly smaller than $d^{L/2}$.

The fact that after an SVD the relation $U^\dagger U = \mathbb{1}$ is fulfilled causes the A matrices to be left-normalized which means that

$$\sum_{\sigma_l} A^{\sigma_l \dagger} A^{\sigma_l} = \mathbb{1} \tag{34}$$

An MPS only consisting of left-normalized matrices is called left-canonical.

Left-normalized matrices were the result of subsequent SVD starting on the left on site 1. However, the very same thing can be done the other way around by subsequently performing SVD on the right side of the chain starting on site L. An analogous process as described above results in a matrix product state of the form

$$|\Psi\rangle = \sum_{\sigma_1\ldots\sigma_L} B^{\sigma_1} B^{\sigma_2} \ldots B^{\sigma_{L-1}} B^{\sigma_L} |\sigma_1,\ldots,\sigma_L\rangle \tag{35}$$

However, now we have B matrices which are, due to the fact that $V^\dagger V = \mathbb{1}$, right normalized:

$$\sum_{\sigma_l} B^{\sigma_l} B^{\sigma_l \dagger} = \mathbb{1} \tag{36}$$

An MPS only consisting of right-normalized matrices is called right-canonical.

One could also combine these two representations and construct a so-called mixed-canonical MPS. This is done by applying both decompositions on the right site as well as on the left side. One can start decomposing the coefficient matrix from the left up to site l and then continue by performing decompositions from the right starting on site L by which one obtains A and B matrices, respectively. The mixed-canonical MPS will then have the following form:

$$|\Psi\rangle = \sum_{\sigma_1 \dots \sigma_L} A^{\sigma_1} \dots A^{\sigma_l} S B^{\sigma_{l+1}} \dots B^{\sigma_L} |\sigma_1, \dots, \sigma_L\rangle \tag{37}$$

where A are left-normalized matrices, B are right-normalized matrices and S is a singular value matrix on bond $(l, l+1)$.

In order to efficiently represent and work with MPS, the following graphical representations were introduced: A matrices can be represented in the following way:
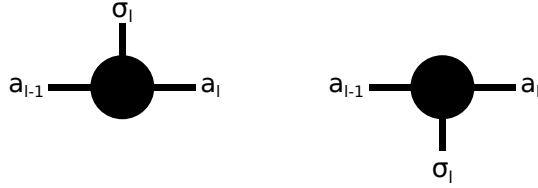

Figure 1: Graphical representation of $A^{\sigma_l}_{a_{l-1}a_l}$ (left) and its conjugate $A^{\sigma_l *}_{a_{l-1}a_l}$ (right).

Here, σ_l denotes the physical (spin) index and a_{l-1} and a_l denote bond indices.

The left-normalization of the A matrices (eq. 34) can be illustrated in the following way:
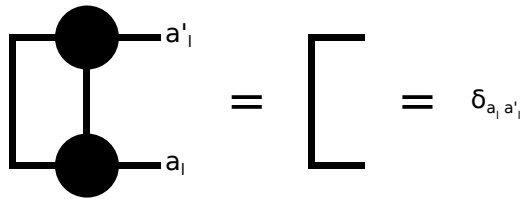

Figure 2: Graphical representation of two left-normalized A matrices that are contracted over their left index and simplify to $\delta_{a_l a'_l}$.

3.2 Entanglement entropy

In the last chapter, the von Neumann entanglement entropy was introduced. This chapter will show that the entropy is an important observable for MPS calculations as it is directly related to the bond dimension of the matrices. The entanglement entropy is one possibility of measuring the quantum entanglement in systems like quantum spin chains. Although there are other measures of entanglement, the entropy is a very convenient choice.[9]

For a system with two subsystems A and B, the von Neumann entropy reads

$$S_A = -\sum_{a=1}^{\chi} \lambda_a^2 \ln \lambda_a^2 = S_B \tag{38}$$

This means that the maximum possible value is given when all singular values λ_a are of equal value, i.e. $\lambda_a^2 = \frac{1}{\chi}$ because $\sum_a \lambda_a^2 = 1$ has to be fulfilled. Therefore, the reduced density matrix $\hat{\rho}_A$ is of the form

$$\hat{\rho}_A = \frac{1}{\chi} \, \mathbb{1} \tag{39}$$

and therefore the maximum value for S_A is given by

$$S_A = -\chi \left(\frac{1}{\chi} \ln \frac{1}{\chi} \right) = \ln \chi \tag{40}$$

During an MPS calculation, the bond dimension χ of the matrices will grow and especially for large systems, an exact representation with bond dimensions up to $d^{L/2}$ is simply not possible. Therefore, the matrices are truncated during the SVD by discarding small singular values λ_a. The truncation can be done in two ways: Either one sets a threshold ϵ (e.g. 10^{-8}) or one can set a maximum bond dimension χ_{max}. All singular values beyond χ_{max} will be discarded. The quality of the approximation can be measured with the so-called discarded weight which is defined as

$$w = 1 - \sum_{a=1}^{\chi_{max}} \lambda_a^2 \tag{41}$$

In order to obtain accurate results, the discarded weight should be in the order of $w = 10^{-8}$. The discarded weight will be small if the singular values λ_a decay quickly. This is the case when the entanglement entropy is small. However, we know that for a given bond dimension χ, the maximum entanglement entropy is given by $\ln(\chi)$. Therefore, we can estimate that the matrix bond dimension one needs is of the size of about

$$\chi_{max} \sim e^{S_A} \tag{42}$$

This means that a linearly increasing entropy can lead to exponentially growing bond dimensions. Unless one wants to sacrifice the accuracy of the calculations, this means that the matrix sizes in the calculations would also have to grow exponentially. However,

the problem with an increasing bond dimension is that this leads to rapidly increasing computational costs:

For a matrix with dimension $(m * n)$, where $m \geq n$, the cost of an SVD is $O(mn^2)$.[1] A simple matrix multiplication of an $(m * n)$ matrix with an $(n * p)$ matrix has a computational cost of the order $O(mnp)$. Therefore, matrix dimensions have to be limited in computational simulations which basically means that at some point, one has to discard relevant singular values which will lead to worse accuracy and eventually to completely useless results. However, in order to keep the truncated weight below a given threshold, an increasing number of states needs to be kept. (see [10]) As they increase the computational costs so rapidly, the simulation time of the system is limited by the (exponentially) increasing bond dimensions. The growing bond dimensions actually were the major limitation for many of the time evolutions performed in this thesis.

The growth of entanglement entropy in real time quench dynamics of the Anderson impurity model was e.g. studied by He and Millis.[11] They considered a semi-circular DOS in a single-impurity Anderson model (SIAM) in the form of a non-interacting chain model, where two chains on a different chemical potential with different hopping parameters are coupled to a single impurity site. However, the hopping parameters within each of the two chains remain constant. By adjusting the different chemical potentials, the DOS of the two chains can be varied: When the DOS were touching only at one energy point, the entropy was growing logarithmically, whereas in the case of overlapping DOS, a linear entropy growth could be observed. When the system was gapped, the entropy growth saturated.

In the case of chain geometries, there is also a hopping between the bath sites whereas in a star geometry bath, hopping is only onto the system possible. For general initial states, the star geometry has a better entropy behaviour than the chain geometry. However, a star geometry alone is not a guarantee for logarithmic entropy growth as the order of the bath orbitals in the MPS does matter: Only for a star geometry in which the bath sites are ordered by energy, a linearly growing entanglement entropy could be observed. In other cases, where the order of energies was random, the entropy growth was similar to the entropy growth for chain geometry baths. For all simulations in this thesis, the star geometry bath sites were ordered by energy.

The entanglement growth in XXZ spin chains was studied e.g. by Alba and Heidrich-Meisner.[12] They considered so-called geometric quenches, in which two separate chains are prepared in different states and put together at $t = 0$. In this case, the left chain was in the ground state whereas in the right chain all spins were up spins. In the open chain XX model, the following entanglement entropy growth could be observed: The entanglement would grow until a certain plateau is reached. Then the entropy decreases and increases again onto a plateau with a higher value and so on.

3.3 DMRG

This section introduces the Density Matrix Renormalization Group (DMRG) (invented by White in 1992 [13]) in the context of MPS and closely follows [1] and [14].

Now that we have introduced Matrix Product States, this concept can be generalized and also applied to operators. This can be done by writing the coefficients of operators as

$$\langle \sigma | \hat{O} | \sigma' \rangle = \sum_{\sigma\sigma'} M^{\sigma_1 \sigma_1'} M^{\sigma_2 \sigma_2'} \dots M^{\sigma_{L-1} \sigma_{L-1}'} M^{\sigma_L \sigma_L'} \tag{43}$$

These M matrices represent the coefficients of the operator in the same way like the A and B matrices represent the coefficients of an MPS. Therefore, we can obtain the representation of an operator as a Matrix Product Operator (MPO):

$$\hat{O} = \sum_{\sigma\sigma'} M^{\sigma_1 \sigma_1'} M^{\sigma_2 \sigma_2'} \dots M^{\sigma_{L-1} \sigma_{L-1}'} M^{\sigma_L \sigma_L'} | \sigma_1, \dots, \sigma_L \rangle \langle \sigma_1', \dots, \sigma_L' | \tag{44}$$

In fact, every operator can be brought in the form of eq. 44. One simply starts from the representation with a coefficient matrix like in eq. 45 and then performs a decomposition into matrices just like it was done for an MPS before.

$$\hat{O} = \sum_{\sigma_1, \dots, \sigma_L, \sigma_1', \dots, \sigma_L'} c_{(\sigma_1, \dots, \sigma_L), (\sigma_1', \dots, \sigma_L')} | \sigma_1, \dots, \sigma_L \rangle \langle \sigma_1', \dots, \sigma_L' | \tag{45}$$

Now we can calculate expressions like $\langle \Psi | \hat{O} | \Psi \rangle$ in the context of Matrix Products by using MPS and MPO. The calculation of this expectation value amounts to the contraction of the full network of MPS and MPO matrices. This can also be done in a graphical way. MPOs are depicted as squares resulting in the following graphical depiction of $\langle \Psi | \hat{O} | \Psi \rangle$:
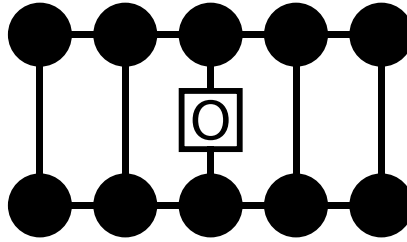

Figure 3: Graphical representation of $\langle \Psi | \hat{O} | \Psi \rangle$, where $\hat{O}$ is a local operator acting on one site.

After a contraction of the right- and left-normalized matrices, just like in fig. 2, this expression simplifies to fig. 4:
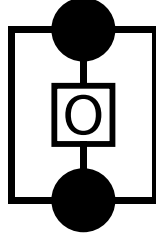
Figure 4: Graphical representation of $\langle\Psi|\,\hat{O}\,|\Psi\rangle$ after the contraction of the right- and left-normalized matrices. $\hat{O}$ is a local operator acting on one site.

Having now introduced MPS and MPO, we can understand DMRG in the context of Matrix Products.

Fig. 5 shows a tensor network with an MPO acting on all sites that will then get contracted during DMRG:
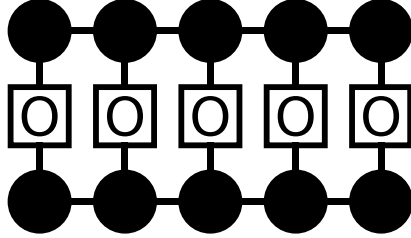

Figure 5: Graphical representation of the expectation value $\langle\Psi|\,\hat{O}\,|\Psi\rangle$ of a tensor network with an MPO acting on all sites of the system.

As the MPS matrices can be left- or right-normalized, a general MPS matrix will be denoted as X_l^σ, MPO matrices are denoted as $M^{\sigma\sigma'}$. If we start contracting the whole network from the left, we first obtain

$$E_1 = \sum_{\sigma_1\sigma_1'} X^{\sigma_1} M^{\sigma_1\sigma_1'} \bar{X}^{\sigma_1'} \tag{46}$$

The very same thing can be done starting from the right:

$$F_L = \sum_{\sigma_L\sigma_L'} X^{\sigma_L} M^{\sigma_L\sigma_L'} \bar{X}^{\sigma_L'} \tag{47}$$

For a general site n, the corresponding matrices are given by

$$
\begin{aligned}
E_n = E^{\beta_n}_{\alpha_n\alpha_n'} \quad &= \sum_{\alpha_{n-1}\sigma_n} X^{\sigma_n}_{\alpha_{n-1}\alpha_n} \sum_{\beta_{n-1}\sigma_n'} M^{\sigma_n\sigma_n'}_{\beta_{n-1}\beta_n} \sum_{\alpha_{n-1}'} E^{\beta_{n-1}}_{\alpha_{n-1}\alpha_{n-1}'} \bar{X}^{\sigma_n'}_{\alpha_{n-1}'\alpha_n'} \\
F_n = F^{\beta_{n-1}}_{\alpha_{n-1}\alpha_{n-1}'} &= \sum_{\alpha_n\sigma_n} X^{\sigma_n}_{\alpha_{n-1}\alpha_n} \sum_{\beta_n\sigma_n'} M^{\sigma_n\sigma_n'}_{\beta_{n-1}\beta_n} \sum_{\alpha_n'} F^{\beta_n}_{\alpha_n\alpha_n'} \bar{X}^{\sigma_n'}_{\alpha_{n-1}'\alpha_n'}
\end{aligned}
\tag{48}
$$

DMRG can now be used to calculate the ground state energy of a system. The calculation of the ground state energy corresponds to minimizing the functional

$$\mathcal{H} = \frac{\langle \Psi | H | \Psi \rangle}{\langle \Psi | \Psi \rangle} \tag{49}$$

where $|\Psi\rangle$ is an MPS of the form

$$|\Psi\rangle = \sum_{\{\sigma_i\}} X^{\sigma_1} X^{\sigma_2} \dots X^{\sigma_{L-1}} X^{\sigma_L} |\{\sigma_i\}\rangle \tag{50}$$

We also demand that $|\Psi\rangle$ is normalized. This condition can be incorporated by using a Lagrange multiplier λ:

$$\mathcal{H} \rightarrow \tilde{\mathcal{H}} = \langle \Psi | H | \Psi \rangle - \lambda(\langle \Psi | \Psi \rangle - 1) \tag{51}$$

Minimizing this functional will result in the ground state wave function $|\Psi_0\rangle$:

$$\min_{|\Psi\rangle} \tilde{\mathcal{H}} \rightarrow |\Psi_0\rangle \tag{52}$$

To perform the minimization, one picks out a single site n and keeps the matrices of all other sites fixed. The overlap therefore reads

$$\langle \Psi | \Psi \rangle = \sum_{\{\sigma\}\{\alpha,\alpha'\}} \underbrace{X^{\sigma_1}_{\alpha_1} \bar{X}^{\sigma_1}_{\alpha'_1} \dots X^{\sigma_{n-1}}_{\alpha_{n-2}\alpha_{n-1}} \bar{X}^{\sigma_{n-1}}_{\alpha'_{n-2}\alpha'_{n-1}}}_{\Psi^L_{\alpha_{n-1}\alpha'_{n-1}}} X^{\sigma_n}_{\alpha_{n-1}\alpha_n} \dots$$

$$\bar{X}^{\sigma_n}_{\alpha'_{n-1}\alpha'_n} \underbrace{X^{\sigma_{n+1}}_{\alpha_n\alpha_{n+1}} \bar{X}^{\sigma_{n+1}}_{\alpha'_n\alpha'_{n+1}} \dots X^{\sigma_N}_{\alpha_N} \bar{X}^{\sigma_N}_{\alpha'_N}}_{\Psi^R_{\alpha_n\alpha'_n}} \tag{53}$$

Therefore, the minimization problem in eq. 51 can be written as

$$\tilde{\mathcal{H}} = \sum_{\substack{\beta_n \alpha_n \alpha'_n \sigma'_n \\ \beta_{n-1} \alpha_{n-1} \alpha'_{n-1} \sigma_n}} E^{\beta_{n-1}}_{\alpha_{n-1}\alpha'_{n-1}} X^{\sigma_n}_{\alpha_{n-1}\alpha_n} M^{\sigma_n \sigma'_n}_{\beta_{n-1}\beta_n} \bar{X}^{\sigma'_n}_{\alpha'_{n-1}\alpha'_n} F^{\beta_n}_{\alpha_n\alpha'_n} -$$

$$\lambda \left(\sum_{\substack{\alpha_n \alpha'_n \sigma'_n \\ \alpha_{n-1} \alpha'_{n-1} \sigma_n}} \Psi^L_{\alpha_{n-1}\alpha'_{n-1}} X^{\sigma_n}_{\alpha_{n-1}\alpha_n} \bar{X}^{\sigma'_n}_{\alpha'_{n-1}\alpha'_n} \delta_{\sigma_n \sigma'_n} \Psi^R_{\alpha_n\alpha'_n} - 1 \right) \tag{54}$$

To find the minimum of eq. 54 with respect to $X^{\sigma'_n}_{\alpha'_{n-1}\alpha'_n}$, the derivative by $\bar{X}^{\sigma'_n}_{\alpha'_{n-1}\alpha'_n}$ is set to zero. This results in the following equation:

$$\nabla_{\bar{X}_{\alpha'}} \tilde{\mathcal{H}} = \sum_\alpha \left(h_{\alpha'\alpha} - \lambda \sum_\alpha N_{\alpha'\alpha} \right) X_\alpha \overset{!}{=} 0$$

$$h_{\alpha'\alpha} = \sum_{\beta_{n-1}\beta_n} E^{\beta_{n-1}}_{\alpha_{n-1}\alpha'_{n-1}} M^{\sigma_n \sigma'_n}_{\beta_{n-1}\beta_n} F^{\beta_n}_{\alpha_n \alpha'_n} \tag{55}$$

$$N_{\alpha'\alpha} = \Psi^L_{\alpha_{n-1}\alpha'_{n-1}} \Psi^R_{\alpha_n \alpha'_n} \delta_{\sigma_n \sigma'_n}$$

This equation can be significantly simplified by using a mixed-canonical state in the way that all X matrices on sites $k < n$ are left-normalized A matrices and all X matrices on sites $l > m$ are right-normalized B matrices. By doing so, one achieves that $\Psi^L_{\alpha_{n-1}\alpha'_{n-1}} \rightarrow \delta_{\alpha_{n-1}\alpha'_{n-1}}$ and $\Psi^R_{\alpha_n \alpha'_n} \rightarrow \delta_{\alpha_n \alpha'_n}$. Therefore, eq. 55 simplifies to

$$\sum_{\alpha'} h_{\alpha'\alpha} X_\alpha = \lambda X_\alpha$$

$$h_{\alpha'\alpha} = \sum_{\beta_{n-1}\beta_n} L^{\beta_{n-1}}_{\alpha_{n-1}\alpha'_{n-1}} M^{\sigma_n \sigma'_n}_{\beta_{n-1}\beta_n} R^{\beta_n}_{\alpha_n \alpha'_n} \tag{56}$$

This system can now be solved using for example a Lanczos eigensolver. It is important to note that $h_{\alpha'\alpha}$ never has to be explicitly built up due to its product structure. Now, one can search for the ground state in the following way (a more detailed description can be found in [14]):

At first, the MPS consisting only of right-normalized B matrices is initialized with random numbers and normalized. Then, all R_n expressions are calculated by running from right to left. Then, the first L matrix L_0 on the left side is calculated. For the first step, this is a scalar. Starting from the left, one then sweeps from left to right until site $N-1$: On each site, eq. 56 is solved and after the eigensolver is converged, the resulting matrix X is brought into a left-normalized form A via SVD. L_n can then be obtained by contracting the new A matrix to the last L_{n-1} expression.

After that, one sweeps from right to left, starting on site N until site 2 is reached. Again, the eigenvalue problem is solved on each site, but now the obtained X matrix is brought into a right-orthonormal form B by applying an SVD. R_n is then gained by contracting the new B matrix to the last R_{n+1} expression.

Now one checks whether the ground state energy has converged. If not, another sweep is done until the system is converged or a certain criterion is reached.

3.4 Time-Evolving Block Decimation

The time-evolving block decimation (TEBD) algorithm was introduced by G. Vidal.[3, 15] This section closely follows [3].
We start from an MPS as introduced in chap. 3.1:

$$|\Psi\rangle = \sum_{\sigma_1 \ldots \sigma_L} A^{\sigma_1} A^{\sigma_2} \ldots A^{\sigma_{L-1}} A^{\sigma_L} |\sigma_1, \ldots, \sigma_L\rangle$$

However, we will now introduce a certain representation of the matrices, the so-called canonical form:

$$A^{\sigma_{i+1}}_{\alpha_i \alpha_{i+1}} = \lambda^{[i]}_{\alpha_i} \Gamma^{\sigma_{i+1}}_{\alpha_i \alpha_{i+1}} \tag{57}$$

consisting of L tensors $\{\Gamma^{\sigma_1} \ldots \Gamma^{\sigma_L}\}$ and $L-1$ vectors $\{\lambda^{[1]} \ldots \lambda^{[L-1]}\}$. The resulting MPS therefore has the following form:

$$|\Psi\rangle = \sum_{\sigma_1 \ldots \sigma_L} c_{\sigma_1 \ldots \sigma_L} |\sigma_1, \ldots, \sigma_L\rangle \tag{58}$$

where $c_{\sigma_1 \ldots \sigma_L}$ is given by

$$c_{\sigma_1 \ldots \sigma_L} = \sum_{\alpha_1 \ldots \alpha_{L-1}} \Gamma^{\sigma_1}_{\alpha_1} \lambda^{[1]}_{\alpha_1} \Gamma^{\sigma_2}_{\alpha_1 \alpha_2} \lambda^{[2]}_{\alpha_2} \ldots \Gamma^{\sigma_L}_{\alpha_{L-1}} \tag{59}$$

We will now consider a Hamiltonian which acts on two sites i.e. H is a sum of two-site Hamiltonians $h_{i,i+1}$. As we have a unitary time evolution, the following Lemma by Vidal [3] is valid:
"Updating the Γ's and λ's of state $|\Psi\rangle$ after a unitary operation V acts on qubits l and $l+1$ involves transforming only Γ^{σ_l}, $\lambda^{[l]}$ and $\Gamma^{\sigma_{l+1}}$. This can be achieved with $\mathcal{O}(\chi^3)$ basic operations."[2]
The algorithm to update the MPS now works in the following way:
At first, the system is split up into 4 subsystems:

$$\mathcal{H} = \mathcal{J} \otimes \mathcal{H}_C \otimes \mathcal{H}_D \otimes \mathcal{K} \tag{60}$$

$\mathcal{H}_C$ and $\mathcal{H}_D$ correspond to the sites l and $l+1$, respectively. $\mathcal{J}$ denotes all sites $1 \ldots l-1$ and $\mathcal{K}$ denotes all sites $l+2 \ldots L$.
$\mathcal{J}$ is spanned by the χ eigenvectors of the reduced density matrix

$$\rho^{[1 \ldots (l-1)]} = \sum_{\alpha} |\alpha\rangle \langle\alpha| \tag{61}$$

and, similarly, $\mathcal{K}$ is spanned by the χ eigenvectors of the reduced density matrix

$$\rho^{[(l+2) \ldots L]} = \sum_{\gamma} |\gamma\rangle \langle\gamma| \tag{62}$$

---

[2]Please note that here, χ is the number of product states

Thus, the whole system can be represented in the following way:

$$|\Psi\rangle = \sum_{\alpha,\beta,\gamma=1}^{\chi} \sum_{i,j=0}^{1} \Gamma_{\alpha\beta}^{[C]i} \lambda_\beta \Gamma_{\beta\gamma}^{[D]j} |\alpha i j \gamma\rangle \tag{63}$$

We will now apply the unitary operation V acting only on sites l and $l+1$. When doing so, according to the Lemma by Vidal from above, we only have to update $\Gamma^{[C]}$, λ and $\Gamma^{[D]}$. The result $|\Psi'\rangle = V|\Psi\rangle$ can be expanded in the following way:

$$|\Psi'\rangle = \sum_{\alpha,\gamma=1}^{\chi} \sum_{i,j=0}^{1} \Theta_{\alpha\gamma}^{ij} |\alpha i j \gamma\rangle \tag{64}$$

where

$$\Theta_{\alpha\gamma}^{ij} = \sum_\beta \sum_{kl} V_{kl}^{ij} \Gamma_{\alpha\beta}^{[C]k} \lambda_\beta \Gamma_{\beta\gamma}^{[D]l} \tag{65}$$

Now, the updated matrices have to be evaluated. At first, $\rho'^{[D\mathcal{K}]}$ is diagonalized

$$\rho'^{[D\mathcal{K}]} = Tr_{\mathcal{J}C} |\Psi'\rangle \langle\Psi'| = \sum_{j,j',\gamma,\gamma'} \left(\sum_{\alpha,i} \langle\alpha|\alpha\rangle \Theta_{\alpha\gamma}^{ij} \left(\Theta_{\alpha\gamma'}^{ij'}\right)^* \right) |j\gamma\rangle \langle j'\gamma'| \tag{66}$$

and the obtained eigenvectors $\left\{ |\phi_\beta'^{[D\mathcal{K}]}\rangle \right\}$ can be expanded in terms of $\{|j\gamma\rangle\}$

$$|\phi_\beta'^{[D\mathcal{K}]}\rangle = \sum_{j,\gamma} \Gamma_{\beta\gamma}'^{[D]j} |j\gamma\rangle \tag{67}$$

from which we can obtain the updated $\Gamma'^{[D]}$.
The eigenvectors of $\rho'^{[\mathcal{J}C]}$ and λ' follow from

$$\lambda_\beta' |\phi_\beta'^{[\mathcal{J}C]}\rangle = \langle\phi_\beta'^{[D\mathcal{K}]}|\Psi'\rangle =$$
$$\sum_{i,j,\alpha,\gamma} \left(\Gamma_{\beta\gamma}'^{[D]j}\right)^* \Theta_{\alpha\gamma}^{ij} \langle\gamma|\gamma\rangle |\alpha i\rangle \tag{68}$$

By expanding each $|\phi_\beta'^{[\mathcal{J}C]}\rangle$ into

$$|\phi_\beta'^{[\mathcal{J}C]}\rangle = \sum_{i\alpha} \Gamma_{\alpha\beta}'^{[C]i} |\alpha i\rangle \tag{69}$$

we also obtain $\Gamma'^{[C]}$. The detailed proof can be found in [3].

In order to perform the time evolution, a Trotter-Suzuki expansion of the time evolution operator e^{-iHt} has to be applied:
Let us assume a Hamiltonian consisting of nearest neighbour interactions only i.e.

$H = \sum_i h_{i,i+1}$ where $h_{i,i+1}$ describes interaction between sites i and $i+1$. The simulation time is discretized as $t = N_t \Delta t$. H can now be split into even and odd parts:

$$H = H_{even} + H_{odd} = \sum_{i,even} h_{i,i+1} + \sum_{i,odd} h_{i,i+1} \tag{70}$$

where all even $h_{i,i+1}$ commute with each other as well as all odd $h_{i,i+1}$ commute with each other but in general

$$[H_{even}, H_{odd}] \neq 0 \tag{71}$$

A first order Trotter-Suzuki decomposition is then given by

$$e^{-iHt} = \left[e^{-i(H_{even}+H_{odd})\Delta t} \right]^{t/\Delta t} \approx \left[e^{-iH_{even}\Delta t} e^{-iH_{odd}\Delta t} \right]^{t/\Delta t} \tag{72}$$

which leads to an error of $O((\Delta t)^2)$:

$$e^{-iH\Delta t} = e^{-iH_{even}\Delta t} e^{-iH_{odd}\Delta t} + O([H_{even}, H_{odd}] (\Delta t)^2) \tag{73}$$

The second order order Trotter-Suzuki decomposition is given by

$$e^{-iHt} \approx \left[e^{-iH_{even}\Delta t/2} e^{-iH_{odd}\Delta t} e^{-iH_{even}\Delta t/2} \right]^{t/\Delta t} \tag{74}$$

and leads to an error of $O((\Delta t)^3)$:

$$e^{-iH\Delta t} = e^{-iH_{even}\Delta t/2} e^{-iH_{odd}\Delta t} e^{-iH_{even}\Delta t/2} + O([H_{even}, H_{odd}] (\Delta t)^3) \tag{75}$$

The error occurs due to eq. 71. Finally, H_{even} and H_{odd} can be split up into $h_{i,i+1}$ which can then be applied according to the TEBD algorithm above:

$$\begin{aligned} e^{-iH_{even}\Delta t} &= \prod_{i,even} e^{-ih_{i,i+1}\Delta t} \\ e^{-iH_{odd}\Delta t} &= \prod_{i,odd} e^{-ih_{i,i+1}\Delta t} \end{aligned} \tag{76}$$

3.5 Time-Dependent Variational Principle

3.5.1 Time evolution with TDVP

This section closely follows[4].
Haegeman et al.[4] presented an alternative to TEBD for the time evolution of MPS:
The time-dependent variational principle (TDVP). The basic idea of TDVP is to project
the right-hand side of the Schrödinger equation, $\hat{H}\ket{\Psi}$, onto the tangent space, so that
the evolution never leaves the manifold. Contrary to TEBD, the TDVP algorithm is
well-suited for long-range Hamiltonians and works independently of the Hamiltonian.
The algorithm presented in [4] is based on a Lie-Trotter splitting of the tangent space
vector and is similar to DMRG. As the TDVP projects the evolution onto the manifold
of MPS with fixed bond dimension, there is no need for a truncation step.
First of all, it is important to mention that a physical state is invariant under a gauge
transformation of the form

$$A^s(n) \rightarrow A^s_G(n) = G(n-1)^{-1}A^s(n)G(n) \tag{77}$$

This gauge freedom can especially be used for MPS by using left-orthonormal $(A^s_l(n))$
and right-orthonormal $(A^s_R(n))$ matrices (see chap. 3.1). Therefore, by applying an SVD,
a one-site center block can be decomposed into a right- or left-orthonormal form:

$$A^s_C(n) = C(n-1)A^s_R(n) = A^s_L(n)C(n) \tag{78}$$

By doing so, the MPS can be written in a mixed canonical form with an orthogonality
center at site n so that all matrices on site $s > n$ are right-orthonormal and all matrices
on sites $s < n$ are left-orthonormal.

The algorithm itself can be understood in a geometric fashion: The right-hand side
of the Schrödinger equation is projected onto the tangent space of the MPS manifold
$\mathcal{M}_{MPS}$ by applying an orthogonal projection:

$$\frac{d\ket{\Psi(A)}}{dt} = -i\hat{P}_{T_{\ket{\Psi(A)}}\mathcal{M}_{MPS}}\hat{H}\ket{\Psi(A)} \tag{79}$$

where $\hat{P}_{T_{\ket{\Psi(A)}}\mathcal{M}_{MPS}}$ is the tangent space projector. This projector can be applied to an
arbitrary state in the Hilbert space and can be written in the form

$$\hat{P}_{T_{\ket{\Psi(A)}}\mathcal{M}_{MPS}} = \sum_{n=1}^{N} \hat{P}_L^{[1:n-1]} \otimes \mathbb{1}_n \otimes \hat{P}_R^{[n+1:N]} - \sum_{n=1}^{N-1} \hat{P}_L^{[1:n]} \otimes \hat{P}_R^{[n+1:N]} \tag{80}$$

where

$$\hat{P}_L^{[1:n]} = \sum_{\alpha=1}^{D} \ket{\phi_{L,\alpha}^{[1:n]}}\bra{\phi_{L,\alpha}^{[1:n]}} \tag{81}$$

$$\hat{P}_R^{[n:N]} = \sum_{\beta=1}^{D} |\phi_{R,\beta}^{[n:N]}\rangle \langle \phi_{R,\beta}^{[n:N]}| \tag{82}$$

As mentioned above, this projector projects an arbitrary state onto the MPS tangent space. This space is spanned by the partial derivatives of $|\Psi(A)\rangle$ with respect to all entries $A_{\alpha,\beta}^s(n)$ for all sites $n = 1, \ldots, N$. By introducing the collective index $i = (\alpha, s, \beta, n)$ and a general variation B^i, the general form of an MPS tangent vector can be written as

$$B^i |\partial_i \psi\rangle = \sum_{n=1}^{N} \sum_{\{s_n\}=1}^{d} = A^{s_1}(1) \ldots B^{s_n}(n) \ldots A^{s_N}(N) |s_1 \ldots s_n \ldots s_N\rangle \tag{83}$$

Because of the gauge invariance of the A matrices (see eq. 77), the B matrices have to follow identical transformation laws and follow the same gauge fixing conditions. By applying left and right orthonormalization in every term of eq. 83, the following expression for the tangent vector can be obtained:

$$|\Theta[B]\rangle = \sum_{n=1}^{N} \sum_{\{\alpha,\beta,s_n\}} B_{\alpha,\beta}^{s_n}(n) |\phi_{L,\alpha}^{[1:n-1]}\rangle |s_n\rangle \langle \phi_{R,\beta}^{[n+1:N]}| \tag{84}$$

In this representation,

$$B^s(n) = X(n-1)A_R^s(n) - A_L^s(n)X(n) \tag{85}$$

By imposing the "left gauge fixing condition" $\sum_s A_L^s(n)B^s(n) = 0$, one can ensure that the overlap of two tangent vectors will only have diagonal contributions:

$$\langle \Theta[B_1] | \Theta[B_2]\rangle = \sum_{n=1}^{N} \sum_{s_n} Tr\left[B_1^{s_n}(n)^\dagger B_2^{s_n}(n)\right] \tag{86}$$

This corresponds to the standard Euclidean inner product and therefore to the choice of an orthonormal basis. The "left gauge fixing condition" is necessary since the bases introduced for the projection operator (see eqs. 81 and 82) are actually not orthonormal as the bases are overcomplete.

When the tangent space projector $\hat{P}_{T_{|\Psi(A)\rangle}\mathcal{M}_{MPS}}$ is applied onto an arbitrary vector $|\Xi\rangle$ of the Hilbert space, the resulting vector $\hat{P}_{T_{|\Psi(A)\rangle}\mathcal{M}_{MPS}} |\Xi\rangle$ is an element of the tangent space of the manifold $\mathcal{M}_{MPS}$. Therefore, this vector can be represented in the form $|\Theta[B]\rangle$. The standard Euclidean inner product (see eq. 86) of the Hilbert space guarantees that the equation $|\Theta[B]\rangle = \hat{P}_{T_{|\Psi(A)\rangle}\mathcal{M}_{MPS}} |\Xi\rangle$ is also a solution of the minimization problem

$$\min_B \||\Theta[B]\rangle - |\Xi\rangle\|^2 \tag{87}$$

This guarantees an optimal representation of the arbitrary vector $|\Xi\rangle$ in the new basis.

In the following chapters, the one-site and the two-site TDVP algorithm are introduced. In this context, the so-called one-site effective Hamiltonian $H(n)$ as well as the zero-site effective Hamiltonian $K(n)$ are used. Those effective Hamiltonians can be best understood if they are introduced in their graphical representation. The one-site effective Hamiltonian $H(n)$ has the following form:
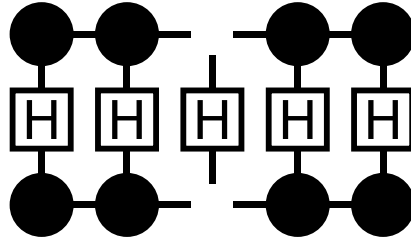
Figure 6: Graphical representation of the one-site effective Hamiltonian $H(n)$. In this depiction, the center site is also the orthogonality center, i.e. all matrices on the right are right-normalized and all matrices on the left are left-normalized.

After a contraction of the matrices left and right of the orthogonality center, $H(n)$ assumes the following form:
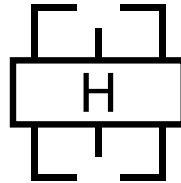
Figure 7: Graphical representation of the one-site effective Hamiltonian $H(n)$ after the contraction of left- and right-normalized matrices

Starting from the one-site effective Hamiltonian $H(n)$, the zero-site effective Hamiltonian can be easily calculated in the following way:
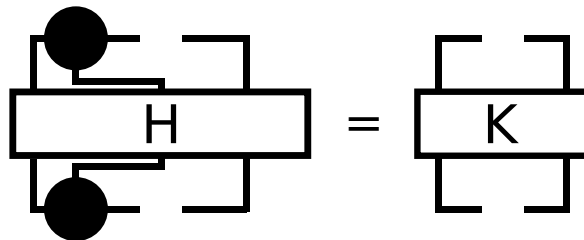
Figure 8: Graphical representation of the zero-site effective Hamiltonian $K(n)$ obtained from $H(n)$ through contraction.

3.5.2 One-site TDVP

While eq. 79 is an equation in the total Hilbert space, the differential equation obtained for a single term can be integrated exactly. If one applies the projector $\hat{P}_L^{[1:n-1]} \otimes \mathbb{1}_n \otimes \hat{P}_R^{[n+1:N]}$ and sets the orthogonality center on site n, the exact time evolution of $A_C(n)$ can be written as

$$A_C(n,t) = e^{-iH(n)t} A_C(n,0) \tag{88}$$

In a similar way, the projector $-\hat{P}_L^{[1:n]} \otimes \hat{P}_R^{[n+1:N]}$ can be integrated by making $C(n)$ time dependent:

$$C(n,t) = e^{iK(n)t} C(n,0) \tag{89}$$

However, in contrary to the time evolution of $A_C(n)$ using the one-site effective Hamiltonian $H(n)$, the evolution of $C(n)$ can be interpreted as an evolution back in time applying the zero-site effective Hamiltonian $K(n)$. The integration can be done with a Lanczos exponentiation algorithm. For the time evolution, the following integration scheme has to be applied:

- evolve $A_C(n)$ according to eq. 88 for a timestep Δt

- factorize the updated $A_C^s(n) \to A_L^s(n)C(n)$

- evolve $C(n)$ back in time according to eq. 89 and then

- absorb it into the next site $C(n)A_R^s(n+1) \to A_C^s(n+1)$

This algorithm is similar to the single-site DMRG algorithm. However, the optimization is replaced with a time evolution and an extra time evolution step of $C(n)$ was added. The algorithm above depicts a sweep from left to right with timestep Δt. In practice, a timestep of $\Delta t/2$ is used for both a sweep from left to right and a sweep from right to left which together form a complete sweep. A single integration step then consists of such a complete sweep and evolves the system in time for a total timestep from time t to $t + \Delta t$. A more detailed description of both algorithms as well as a derivation can be found in [4].

As both $H(n)$ and $K(n)$ are Hermitian, the resulting time evolution will have exact norm and energy conservation (if the Hamiltonian is time-independent). The very same integration scheme can also be used for imaginary time evolution ($t \to -i\tau$) in order to find ground states, although the algorithm has to be varied or $\Delta\tau \to \infty$ in order to obtain the actual ground state. For $\Delta\tau \to \infty$, the algorithm is identical to the variational MPS formulation of the one-site finite-size DMRG algorithm.

3.5.3 Two-site TDVP

In the case of the two-site algorithm [16], two successive sites are updated simultaneously. In order to do so, a block of those two neighbouring sites is formed and after the time evolution factorized into two individual tensors again by applying an SVD. Therefore, the bond dimension can be chosen depending on the Schmidt coefficients. In contrast to the one-site algorithm, this allows to dynamically change the bond dimension, whereas for one-site TDVP, the bond dimension on every bond is fixed.

In order to apply a two-site algorithm, the tangent space vector in eq. 79 has to be replaced by a projector onto the linear space of two-site variations. This state is spanned by the states:

$$
\sum_{n=1}^{N-1} \sum_{\{s_n\}=1}^{d} A^{s_1}(1) \dots A^{s_{n-1}}(n-1) B^{s_n s_{n+1}}(n:n+1) \dots
$$
$$
A^{s_{n+2}}(n+2) \dots A^{s_N}(N) |s_1 \dots s_n \dots s_N\rangle
\tag{90}
$$

For the time evolution, the following integration scheme has to be applied:

- evolve a two-site center block $A_C(n:n+1)$ according to the effective Hamiltonian $H(n:n+1)$

- factor the block into $A_C^{s_n s_{n+1}}(n:n+1) \to A_L^{s_n}(n) A_C^{s_{n+1}}(n+1)$

- evolve $A_C^{s_{n+1}}(n+1)$ backwards in time according to $H(n+1)$ and then

- absorb it into the next two-site block: $A_C^{s_{n+1}}(n+1) A_C^{s_{n+2}}(n+2) \to$
$A_C^{s_{n+1} s_{n+2}}(n+1:n+2)$

A more detailed description of both algorithms as well as a derivation can be found in [4]. To sum up, Haegeman et al. have introduced a time integration scheme for the TDVP in the context of MPS. The algorithm allows the time evolution of an MPS system for an arbitrary Hamiltonian and is especially suitable for Hamiltonians with long-range interactions. Such Hamiltonians can for example be given in the form of an MPO.

3.5.4 Long time simulation of local observables

The TDVP algorithm is especially interesting in the context of local observables as it was recently shown by Leviatan et al.[17].

In their paper, they deal with the problem of the rapid growth of entanglement entropy in time evolutions. In the context of MPS, this results in exponentially increasing bond dimensions. Therefore, the computation time at the desired accuracy is limited and they describe the following way to deal with this problem:

At first, they observed that quantum thermalizing systems are governed at long times by emergent classical hydrodynamics. This hydrodynamic behaviour is dictated by conservation laws and a small number of parameters and therefore, they do not expect that

the dynamics of local observables depend on the detailed long range entanglement structure of the micro-state. The decisive challenge is to truncate the growing entanglement entropy in such a way that the information on local observables is conserved. Several attempts to control the growth of the entanglement entropy were made but none of them could avoid the problem of an exponentially growing bond dimension. Therefore, a different approach was proposed:

Instead of trying to capture the exact dynamics of the system, it was tried to truncate the entanglement growth with a systematic approximation. This was done by applying the one-site TDVP algorithm by Haegeman et al. [4] which was introduced above. By limiting the maximum matrix bond dimension to χ, the maximum entanglement entropy is given by $\log \chi$. Of course, this means that the whole MPS is not anywhere near to being exactly represented. However, as Leviatan et al. argue: "A crucial feature for our purpose is that the TDVP respects conservation laws regardless of the truncation." This would for example not be given in the case of the TEBD algorithm. However, in the case of TDVP, non-linear classical dynamics are generated which guarantee that the hydrodynamic behaviour of local observables emerges at long times even if only small bond dimensions are kept. These hydrodynamics are expected to be determined by quantum processes that occur on short scales and can therefore be captured by MPS with finite bond dimensions.

To prove their point, the approach is tested on an Ising chain with both longitudinal and transverse fields:

$$H = J \sum_{i=0}^{N-1} S_i^x S_{i+1}^x + h_x \sum_{i=0}^{N} S_i^x + h_z \sum_{i=0}^{N} S_i^z \tag{91}$$

Simulations were performed for a chain with 101 sites (i.e. $N = 100$) and the constants $J = 4$, $h_x = 1$, and $h_z = -2.1$. A one-site TDVP algorithm was applied, starting from an initial state of random product states with the direction of the spin on each site chosen independently from a uniform distribution on the Bloch sphere. The ensemble is quenched by applying the single site operator $S_{N/2}^+$ on the middle site of the chain (followed by normalization), to every state in the ensemble. The one-site TDVP algorithm is then applied with a given fixed bond dimension χ. Very small bond dimensions like $\chi = 2, 4, 8$ or 16 were used. This guarantees that the entanglement entropy soon reaches a plateau at the maximum value which is given by $\log_2 \chi$ and does not grow any further. Indeed, the relaxation of the local operator $S_{N/2}^z$ shows the same behaviour for all different bond dimensions. Especially for large times, the expectation value $\langle S_{N/2}^z(t) \rangle$ converges to the same value for all different χ. This is what they call the "hydrodynamic long time tail" and this supports their essential point that long time thermalization dynamics of thermalizing closed quantum systems can indeed be captured accurately using low entanglement states. Hereby, the crucial feature of TDVP is that it satisfies energy conservation and other conservation rules. Thus, quantities that are generated by quantum processes on a short scale can captured accurately even for tiny bond dimensions like $\chi = 2$.

3.6 Star and Chain Geometry of Baths

This section introduces the implementation of baths with different bath geometries and closely follows [18].

The bath is defined by its spectral function. In this thesis, two different approaches were used to simulate the bath spectral function: The star geometry and the Wilson chain geometry.[19, 20] The DOS is defined as

$$D(\omega) = -\frac{1}{\pi} Im(\Lambda(\omega)) \tag{92}$$

where $\Lambda(\omega)$ is the bath spectral function. The hybridization term of the Hamiltonian H_{hyb} couples the bath to the impurity. In our case, the impurity is given by a tight-binding or Hubbard chain and the left (right) bath couples to the first (last) site of this chain. For the left bath, H_{hyb} would be given by

$$H_{hyb} = \sum_{l=1}^{L_b} \sum_{\sigma} \left(V_l c_{0\sigma}^\dagger c_{l\sigma} + H.c. \right) \tag{93}$$

where $c_{0\sigma}^\dagger$ $(c_{0\sigma})$ denotes a creator (annihilator) on the first site of the chain and $c_{l\sigma}^\dagger$ $(c_{l\sigma})$ denotes a creator (annihilator) on a bath site. The bath itself is given by

$$H_{bath} = \sum_{l=1}^{L_b} \sum_{\sigma} \epsilon_l c_{l\sigma}^\dagger c_{l\sigma} \tag{94}$$

The potential energy is given by

$$H_{pot} = \sum_{l=1}^{L_b} \sum_{\sigma} \tilde{\epsilon}_l c_{l\sigma}^\dagger c_{l\sigma} \tag{95}$$

and the kinetic energy is given by

$$H_{kin} = \sum_{l=1}^{L_b-1} \sum_{\sigma} \left(\tilde{V}_l c_{l+1\sigma}^\dagger c_{l\sigma} + H.c. \right) \tag{96}$$

In the case of a star geometry, the spectral function is given by

$$\Lambda^{star}(\omega) = \sum_{l=1}^{L_b} \frac{|V_l|^2}{\omega - \epsilon_l + iO^+} = Re(\Lambda^{star}) + i \sum_{l=1}^{L_b} |V_l|^2 \, \delta(\omega - \epsilon_l) \tag{97}$$

Comparing eq. 92 with eq. 97 leads to

$$D(\omega) = -\frac{1}{\pi} \sum_{l=1}^{L_b} |V_l|^2 \, \delta(\omega - \epsilon_l) \tag{98}$$

Therefore, the coupling parameters V_l can be obtained from

$$V_l^2 = \int_{I_l} d\omega \left[-\frac{1}{\pi} Im(\Lambda(\omega)) \right] \tag{99}$$

with bath discretization intervals $I_l = [\omega_l, \omega_{l+1}]$. For the simulations in this thesis, a linear discretization was used although other discretizations, like for example a logarithmic one, are also possible.
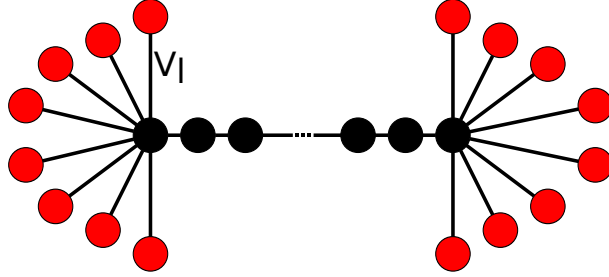

Figure 9: Graphical representation of a system in chain geometry (black sites) coupled to two baths in star geometry (red sites). Each bath site has an on-site energy ϵ_l and couples to the chain with a coupling constant V_l

After obtaining the parameters for the star geometry, the problem can be mapped to chain geometry in the following way:
If one denotes the bath orbital sites as $|c_l\rangle$, the first orbital of the chain is defined as

$$|\tilde{c}_1\rangle = \frac{1}{\tilde{V}_0} \sum_{l=1}^{L_b} V_l |c_l\rangle$$
$$\tilde{V}_0 = \sqrt{\sum_l |V_l|^2} \tag{100}$$

By using a Lanczos algorithm, H_{bath} and H_{hyb} are represented in their Gram-Schmidt orthogonalized Krylov basis $\{|\tilde{c}_l\rangle\}$. H_{hyb} is already diagonal in this basis and has its only non-zero component for $\langle\tilde{c}_1| H_{hyb} |\tilde{c}_1\rangle$. Therefore, only H_{bath} has to be considered in the following Lanczos recursion

$$\tilde{\epsilon}_n = \langle\tilde{c}_n| H_{bath} |\tilde{c}_n\rangle$$
$$|r_n\rangle = H_{bath} |\tilde{c}_n\rangle - \tilde{\epsilon}_n |\tilde{c}_n\rangle - \tilde{V}_{n-1} |\tilde{c}_{n-1}\rangle$$
$$\tilde{V}_n = |\langle r_n|r_n\rangle|^{\frac{1}{2}} \tag{101}$$
$$|\tilde{c}_{n+1}\rangle = \frac{1}{\tilde{V}_n} |r_n\rangle \,, \text{for } n = 2, \ldots, L_b - 1$$

In the case of $n = 1$, only the definition of $|r_n\rangle$ changes to

$$|r_1\rangle = H_{bath} |\tilde{c}_1\rangle - \tilde{\epsilon}_1 |\tilde{c}_1\rangle \tag{102}$$

Methods

The equation
identities of
transformati

where

The transfor

$$(U)_{l,n=1} = (\langle c_l | c_n \rangle)_{l,n=1} = \begin{pmatrix} & & \\ \vdots & \vdots & \ddots \\ V_{L_b}/\tilde{V}_0 & & \end{pmatrix} \tag{105}$$

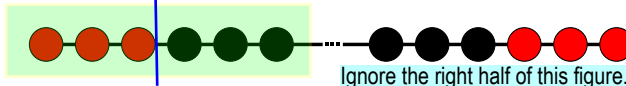and relates the two basis sets via $|\tilde{c}_n\rangle = \sum_l U^\dagger_{nl} |c_l\rangle$.

Figure 10: Graphical representation of a system in chain geometry (black sites) coupled to two baths in chain geometry (red sites). The bath sites couple with each other but only one bath site couples to the system.

Using the methods above, the following algorithm was applied to perform the time evolution. Let us first consider a star geometry bath: At first, the chain was separated into 3 different parts: left bath, middle chain and right bath. The corresponding Hamiltonian reads:

$$H = H_{left} + H_{middle} + H_{right} = H_l + H_m + H_r \tag{106}$$

A first Trotter-Suzuki decomposition leads to the following representation of the time evolution operator:

$$e^{-iH\Delta t} \approx e^{-iH_m\Delta t/2} e^{-iH_l\Delta t} e^{-iH_r\Delta t} e^{-iH_m\Delta t/2} \tag{107}$$

A second Trotter-Suzuki decomposition was performed within the middle by decomposing the middle into even and odd sites:

$$e^{-iH_m\Delta t} \approx e^{-iH_{m,even}\Delta t/2} e^{-iH_{m,odd}\Delta t} e^{-iH_{m,even}\Delta t/2} \tag{108}$$

Thus, the time evolution operator for a star geometry system reads:

$$e^{-iH\Delta t} \approx e^{-iH_{m,e}\Delta t/4} e^{-iH_{m,o}\Delta t/2} e^{-iH_{m,e}\Delta t/4} \dots$$
$$e^{-iH_l\Delta t} e^{-iH_r\Delta t} e^{-iH_{m,e}\Delta t/4} e^{-iH_{m,o}\Delta t/2} e^{-iH_{m,e}\Delta t/4} \tag{109}$$

For the time evolution, two-site time evolution gates of the form $h_{i,i+1}$ were applied. In the case of <mark>star</mark> geometry, the first (last) site on the middle chain is connected to all sites of the left (right) bath. However, in the simulation, the bath sites are still on a chain. As the time evolution gate only acts on neighbouring sites, a <mark>swap</mark> gate was applied which swapped the first (last) side of the middle chain through the left (right) bath to obtain the interactions of the whole bath with the middle chain as introduced in [21].

In the case of a chain geometry bath, no special treatment of the baths is necessary, as the baths are having the same geometry as the middle. Therefore, the whole system can be seen as one chain and only has to be decomposed into even and odd sites:

$$e^{-iH\Delta t} \approx e^{-iH_{even}\Delta t/2} e^{-iH_{odd}\Delta t} e^{-iH_{even}\Delta t/2} \tag{110}$$

The actual Hamiltonians applied during the time evolution can be found in the following chapters 4 and 5.

4 Particle Current

4.1 Particle Transport

This chapter at first introduces the concept of particle current and then gives an overview of some relevant papers. An overview of relevant literature can also be found in [10] and [22].

We will now use the methods introduced above to model particle transport through a one-dimensional tight-binding (and later Hubbard) chain. The tight-binding chain is connected to two baths, one on the left and one on the right. By applying the methods introduced in chap. 3.6, one can now model the bath according to the desired DOS. In this thesis, half-circular and constant DOS were used.

Considering a tight-binding chain with constant hopping parameters

$$H = -t \sum_i \left(c_i^\dagger c_{i+1} + c_{i+1}^\dagger c_i \right), \tag{111}$$

we now want to calculate the (particle) current going through the tight-binding chain. If we define the particle current on site i as $\dot{n}_i$, the following calculation can be obtained:

$$
\begin{aligned}
\dot{n}_i &= \frac{\partial n}{\partial t} \\
&= i\,[H, n_i] \\
&= -it \left(\left[c_i^\dagger c_{i+1}, n_i \right] + \left[c_{i+1}^\dagger c_i, n_i \right] \right) \\
&= -it \left(c_i^\dagger [c_{i+1}, n_i] + [c_i^\dagger, n_i] c_{i+1} + c_{i+1}^\dagger [c_i, n_i] + [c_{i+1}^\dagger, n_i] c_i \right) \\
&= -it \left(\underbrace{[c_i^\dagger, n_i]}_{-c_i^\dagger} c_{i+1} + c_{i+1}^\dagger \underbrace{[c_i, n_i]}_{c_i} \right)
\end{aligned}
\tag{112}
$$

$$\boxed{\dot{n}_i = it \left(c_i^\dagger c_{i+1} - c_{i+1}^\dagger c_i \right)}$$

In all further discussions and figures, a current from left to right will be considered a positive current. The current is induced by starting with a higher occupation in the left bath than in the right bath.
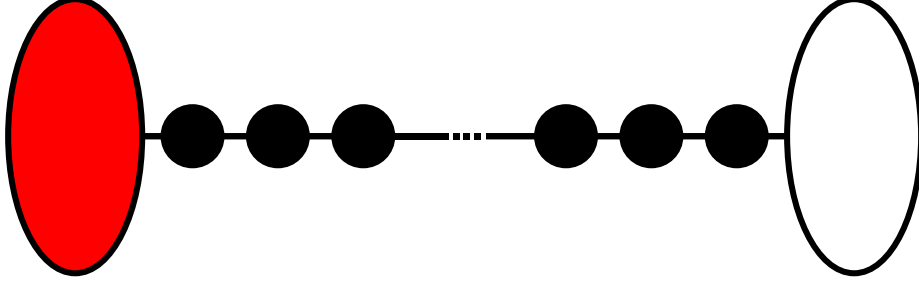
Figure 11: Graphical representation of a possible initial state of the whole system. The left bath is completely filled whereas the right bath is initially empty. The sites on the tight-binding chain are initially half-filled. The baths as well as the chain are initially in a ground state.

Fig. 11 shows a graphical representation of the system in its initial state. Before the time evolution, a ground state search using DMRG is applied on all 3 parts separately. Of course, if the bath is initially completely filled or completely empty, a DMRG ground state search would not change a thing but for a particle current, there only has to be a different filling in the baths and the initial state does not necessarily have to be completely filled or empty.

In the case of a star geometry, the ground state is actually easy to find: The bath sites have no interaction with each other and therefore, the ground state of the bath is only determined by the on-site energies which means that all particles in the system will be initially placed on the sites with the lowest on-site energies. In the middle chain, the ground state search leads to an equally filled chain where the occupation is 0.5 on all sites.

The whole system is described by the following Hamiltonian:

$$H = H_{left} + H_{middle} + H_{right} \tag{113}$$

The left and the right bath are similar as the corresponding Hamiltonians have a term that couples to the chain and an on site energy term:

$$
\begin{aligned}
H_{left} &= \sum_l V_l \left(c_l^\dagger c_{I,1} + c_{I,1}^\dagger c_l \right) + \sum_l \epsilon_l n_l \\
H_{right} &= \sum_l V_l \left(c_l^\dagger c_{I,L} + c_{I,L}^\dagger c_l \right) + \sum_l \epsilon_l n_l
\end{aligned}
\tag{114}
$$

where $c_{I,1}$ ($c_{I,L}$) is the annihilation operator acting on the first (last) site of the middle chain. The subscript I stands for impurity and the ϵ_l denote the on-site energies. The middle is given by a tight-binding chain:

$$H_{middle} = -t \sum_{j=1}^{L-1} \left(c_{I,j}^\dagger c_{I,j+1} + c_{I,j+1}^\dagger c_{I,j} \right) \tag{115}$$

In the case of a Hubbard chain, the following term would have to be added to H_{middle}:

$$H_U = \sum_{j=1}^{L} U n_{I,j\uparrow} n_{I,j\downarrow} \tag{116}$$

Another possibility to obtain a current is introducing an electric potential by adding a different chemical potential to the two baths. Within the system, the chemical potential increases linearly. Therefore, it is not necessary to variate the filling of the baths and the whole chain (left bath, middle and right bath) can be initialized with half filling as it was done in [23]:

Heidrich-Meisner et al. considered a chain separated into two leads and an interaction region in the middle which is connected to those two leads. On the left lead, a constant chemical potential of $V_i = -V/2$ was added and on the right lead, a constant chemical potential of $V_i = V/2$ was added. In the interacting region in the middle, which was given by a Hubbard chain, the chemical potential V_i was increasing linearly with i. By doing so, they could simulate an electric field acting in the interacting part and V is a bias voltage between the two leads. Then, they measured the current (as defined in eq. 112) between the interacting region and the left and right lead, respectively. They then average over these two currents and call the result the symmetrized tunnel current. A quasisteady state regime could be observed where the symmetrized tunnel current would at first oscillate and eventually reach a steady state value. The period of the oscillations decreases with increasing voltage V. Apart from these oscillations, the current reaches a constant value.

Heidrich-Meisner et al. also observe that the time window over which the steady state current can be sustained is limited in a finite system, depending on both the length of the system and the length of the interacting region. A perturbation induced by the bias voltage will travel through the leads, will be reflected on the edges and then travel back to the interacting region. As soon as the perturbation reaches the interacting region, it will also perturb the quasisteady state currents.

Similar calculations were performed for single [10] and double quantum dots.[24]

The system with two quantum dots consisted of two dots which were both connected to two leads. The leads were tight-binding chains with a chemical potential and fully symmetric tunnel couplings were considered i.e. the constant hopping parameter t in the leads was the same as the hopping parameter between the leads and the quantum dots. Again, the current between the two leads was obtained by averaging over the currents between the dots and the left lead and the dots and the right lead. Measuring this current, the current at first undergoes transient dynamics but later, a steady state current could be observed. Finite size effects could also be observed as the steady state would eventually decrease after a certain time, depending on the size of the system.

This behaviour of the current is similar to the case of a single quantum dot. In [10], the set-up was similar: Two leads in the form of tight-binding chains, connected to a single quantum dot. On the dot, there were a chemical potential and a Coulomb repulsion U acting on the dot. The current would again increase at small times and then reach a steady state value in the form of a plateau in time. The steady state value

of the current depends on the number of sites in the leads as well as on the bias voltage V.

4.2 Results

Here we are looking at a particle current flowing through a tight-binding chain which is coupled to a bath on both sides. The tight-binding Hamiltonian for a chain was introduced in eq. 12 and for a constant hopping parameter t, it reads

$$H = -t \sum_{i\sigma} \left(c_{i\sigma}^\dagger c_{i+1\sigma} + c_{i+1\sigma}^\dagger c_{i\sigma} \right)$$

whereas the particle current on site i (see eq. 112) is given by

$$\dot{n}_i = it \left(c_i^\dagger c_{i+1} - c_{i+1}^\dagger c_i \right)$$

In some cases the right bath can be neglected as we are only looking at the particle current flowing from the left bath into the tight-binding chain.

At the beginning, the chain is half-filled and one of the baths is filled with more particles than the other one. For example, the left bath is completely filled whereas the right bath is completely empty. This causes a potential difference between the two baths. Unless otherwise stated, initially the left bath was completely filled and the right bath was completely empty for all simulations, leading to a particle flow from the left bath through the system into the right bath which will be depicted as a positive current.

The baths were either simulated using a star geometry or a Wilson chain geometry as introduced in chap. 3.6. Regarding the DOS of the bath, a constant DOS or a semi-circular DOS were chosen. Besides Wilson chains, a chain geometry bath with a constant hopping parameter t on all sites was also investigated. Before the simulation, the ground state of all 3 parts was calculated by applying DMRG to all 3 parts separately. The ground state of the tight-binding chain in the middle would always be an evenly half-filled state. This was not the case for Wilson chains as the hopping parameter is different between all sides. In the case of a star geometry bath, as the bath sites are not connected, all the particles would be located at the sites with the lowest on-site energies in the ground state.

4.2.1 Comparison of Star and Chain Geometry

A system with a tight-binding chain with 40 sites and 2 baths with 20 sites was simulated. As the same system was simulated using two different bath geometries, the tight-binding chain should undergo the same time evolution in both cases. Indeed, the absolute difference in occupation numbers in the systems of the two simulations had a maximum error in the order of 10^{-3}. Although, the baths of course significantly vary: In the case of a star geometry bath, only particles with the suitable on-site energy, depending on the energy dispersion of the system, will flow from the bath into the system. The energy range from which the particles are taken reaches from $\epsilon = 0$ to $\epsilon = 2$. This can be understood as the energy range of the tight-binding chain ranges from -2 to 2 (for $t = 1$) and the tight-binding chain is initially half-filled. Therefore, there are initially no particles with energies ranging from 0 to 2 in the chain and particles with exactly these

energes will be taken out of the bath. This fact also limits the possible simulation time as at some point, the bath sites within the given energy range will be emptied. In the case of chain geometry baths, the limited simulation time can be understood by the fact that, due to the finite size of the chain, there will be reflections from the wall at the end of the bath. As soon as these reflections reach the tight-binding chain, the results get distorted.

The simulated bath is represented by a normalized, semi-circular DOS with a bandwidth ranging from -3 to 3. The results for chain and star geometry baths can be found in the following figures: The occupation numbers are depicted in fig. 12 and fig. 13.
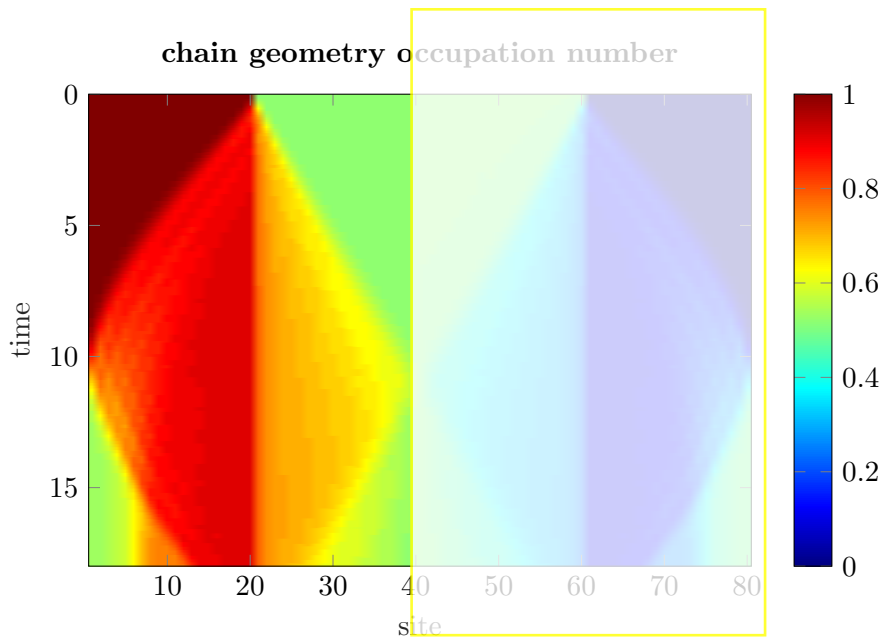
Figure 12: Occupation number for chain geometry baths with a semi-circular DOS and a bandwidth ranging from -3 to 3. The baths both have 20 sites and the system has 40 sites.

star geometry occupation number
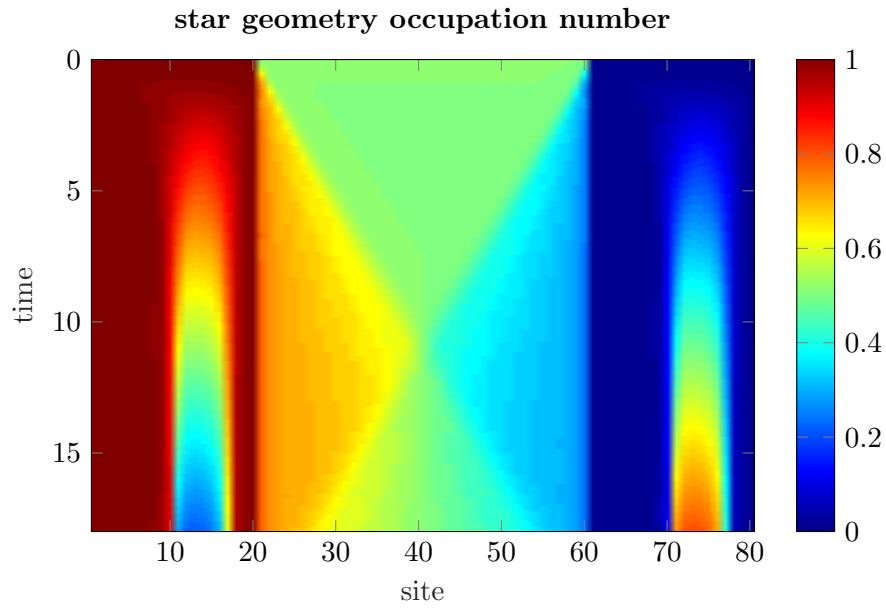
Figure 13: Occupation number for star geometry baths with a semi-circular DOS and a bandwidth ranging from -3 to 3. The baths both have 20 sites and the system has 40 sites.

In both cases, one can observe a linear increasing entropy at the first bond of the middle chain. (see fig. 14 and 15).
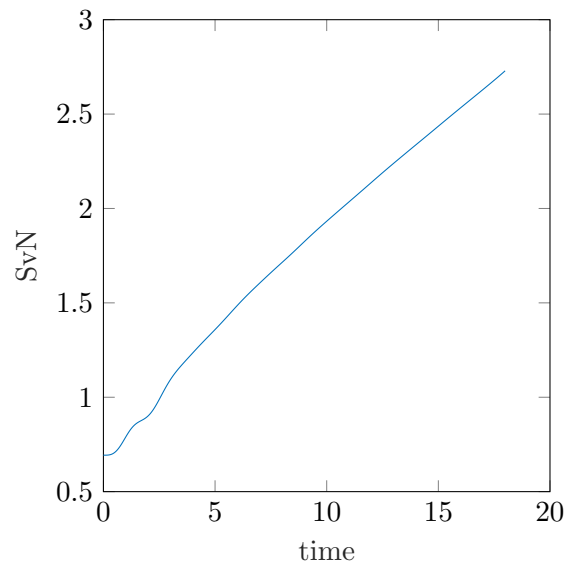

Figure 14: Entanglement entropy at the first bond of the middle chain for a chain geometry bath.
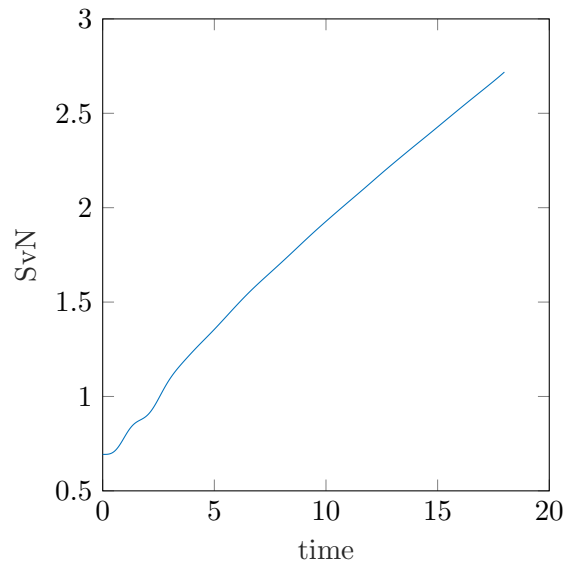
(hopping in left part is different from middle part --> linear growth of S(t))

Figure 15: Entanglement entropy at the first bond of the middle chain for a star geometry bath.

The SvN entanglement entropy on all bonds can be seen in fig. 16 and fig. 17. As one can see, the entanglement entropy spreads into the baths and the tight-binding chain and is especially high at the transition between the baths and the tight-binding chain. In the tight-binding chain however, the entanglement entropies have to be the same for both bath geometries. One can also see that the spreading of the entanglement entropy in the baths in fig. 16 looks similar to the "edge of propagation" of the occupation numbers depicted in fig. 12. Therefore, the spreading of entanglement entropy can be seen as the propagation of quasiparticles.
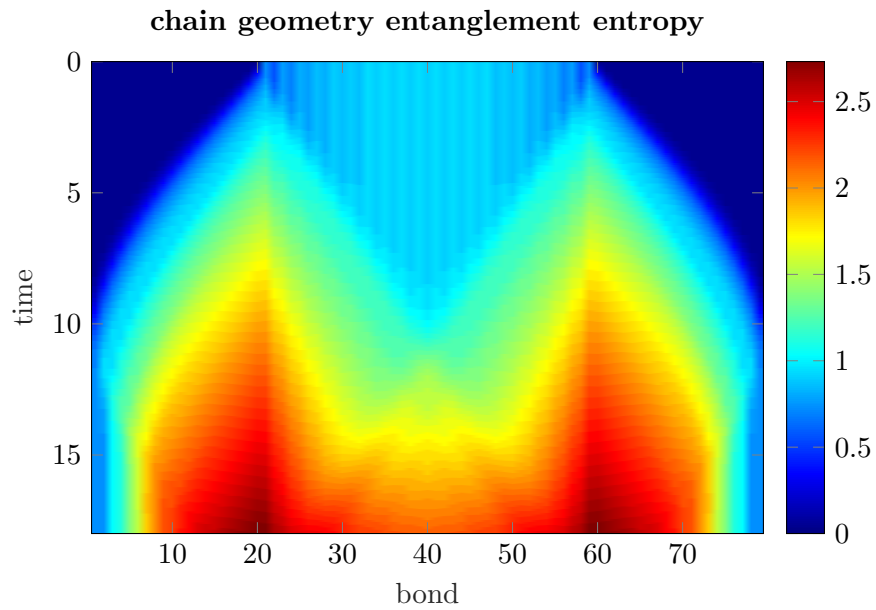
chain geometry entanglement entropy

Figure 16: Entanglement entropy on all bonds for a chain geometry bath. The baths both have 20 sites and the system has 40 sites.

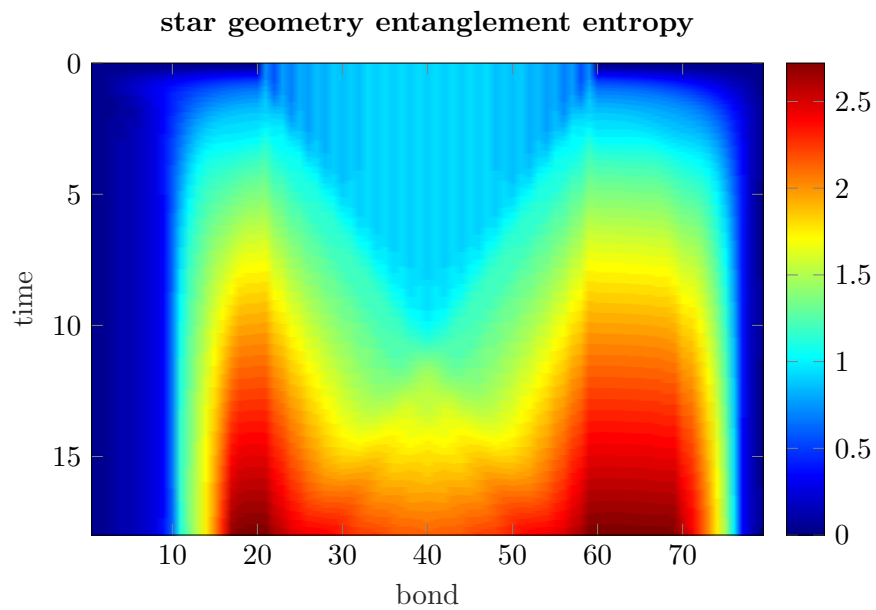**star geometry entanglement entropy**

Figure 17: Entanglement entropy on all bonds for a star geometry bath. The baths both have 20 sites and the system has 40 sites.

4.2.2 Comparison of Wilson and Constant Chain Parameters

Another behaviour of the entanglement entropy can be observed if one uses a chain geometry bath with a constant hopping parameter t for all bath sites instead of a Wilson chain. Here, a constant hopping parameter of $t = 1$ was applied between all sites in both the bath and the middle chain which both had the same size of about 70 sites. This basically gives one large tight-binding chain, where bath and system only differ by their initial filling. Here, only the flow of the particles from the left bath into the tight-binding chain was observed.

In this case, the entanglement entropy does not increase linearly as it can be seen in fig. 19 and fig. 20. Instead, the entanglement entropy increases slower in time and eventually even decreases again. One can also see the change in the hopping parameter of the bath if one looks at the occupation numbers depicted in fig. 22: The propagation speed of the particles in the bath is constant and therefore, the "edge of propagation" is straight and not curved as in fig. 12. This can be understood qualitatively if one looks at the occupation numbers for the Wilson chain geometry bath depicted in fig. 12 and the corresponding hopping parameters in the left bath which can be found in fig. 18.
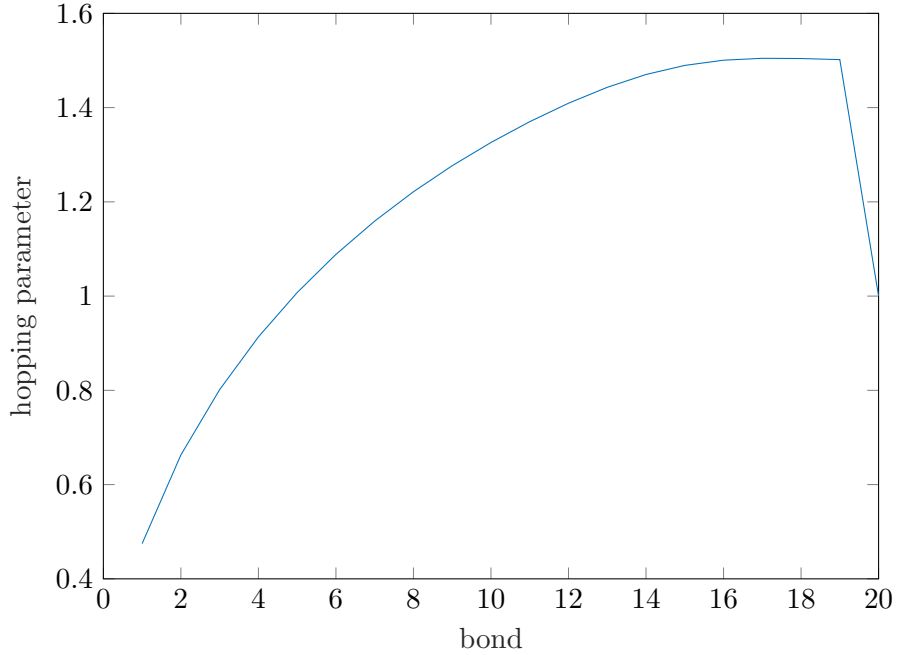

Figure 18: Hopping parameters of the Wilson chain of the left bath in fig. 12 on all bonds of the bath.

From eq. 100, it follows that the first hopping parameter in the Wilson chain is $t = 1$ as the area if the DOS was chosen normalized. The hopping parameters then decrease from around $t = 1.5$ which leads to slower particle velocities at the outer sites of the chain.

The entanglement entropy on all bonds can be seen in fig. 21. Due to the constant hopping parameter t in the chain as well as in the bath, the entanglement entropy also spreads linearly, similar to the occupation number in fig. 22.
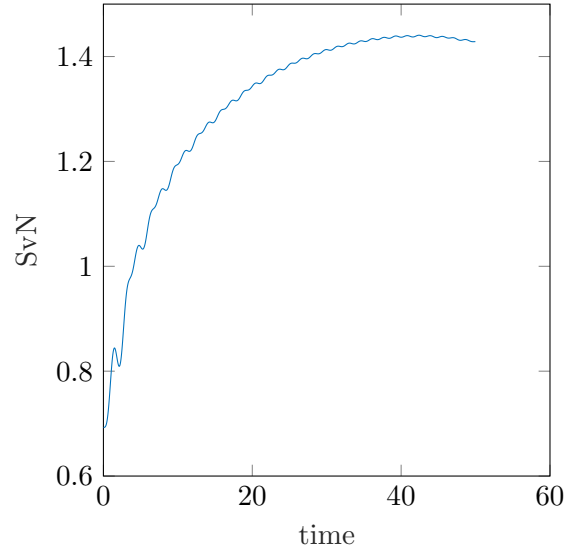

Figure 19: Entanglement entropy at the first bond of the chain. ==Both bath and middle chain are tight-binding chains with a constant hopping parameter of $t = 1$.==

--> **log**. growth of S(t)

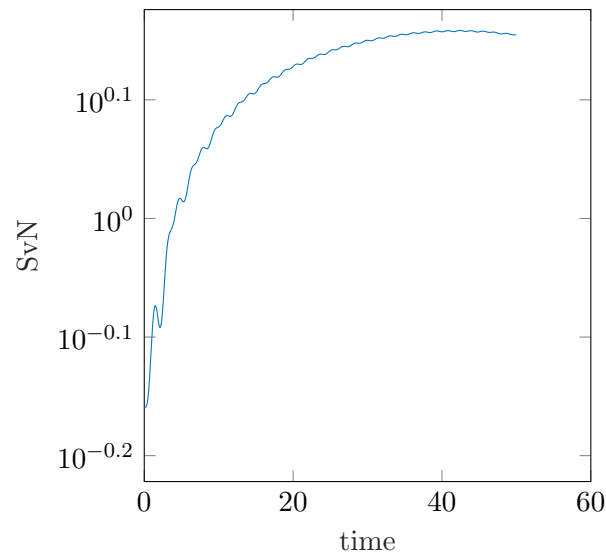Easier to see by plotting S(t) against log t

Figure 20: Semi logarithmic plot of the entanglement entropy at the first bond of the chain. Both bath and middle chain are tight-binding chains with a constant hopping parameter of $t = 1$.
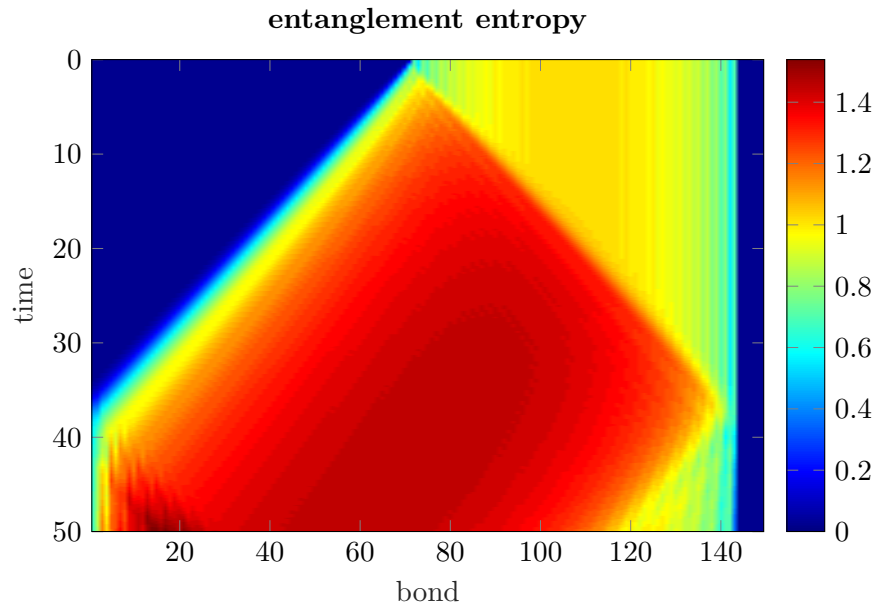
Figure 21: Entanglement entropy on all bonds of the whole system. Both bath and middle chain are tight-binding chains with a constant hopping parameter of $t = 1$. The bath on the left has 72 sites.
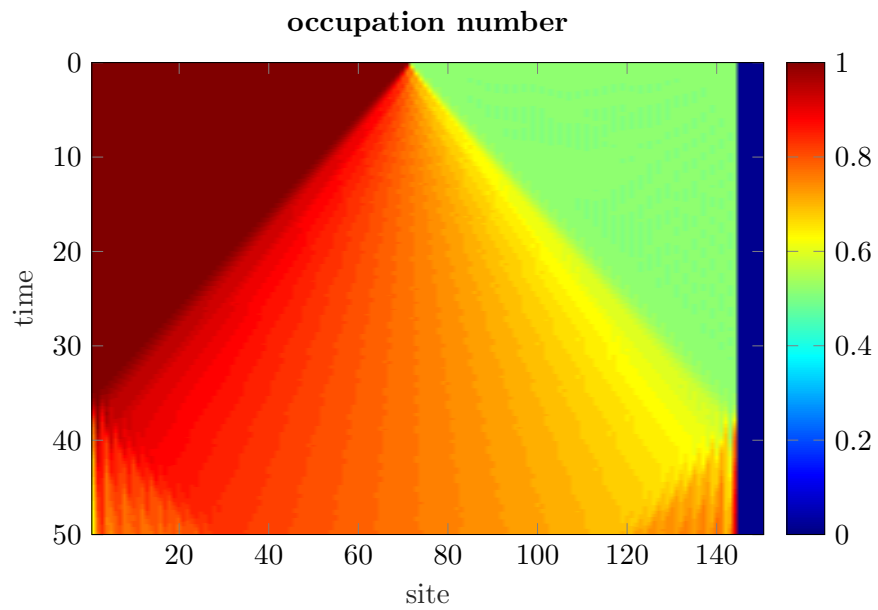

Figure 22: Occupation number for a system where both the left bath and the middle chain have a constant hopping parameter $t = 1$. The bath on the left has 72 sites.

4.2.3 Comparison of a Semi-Circular and a Constant DOS

For a given bandwidth, one can choose different DOS. In this thesis, a semi-circular and a constant DOS were considered. At first, this was done for a star geometry with only a left bath with 35 sites and a middle chain ranging from site 36 to site 108. In both cases, the entanglement entropy increases linearly on the first site of the chain (site 36) as one can see in fig. 23.
In fig. 24 one can see that the occupation numbers are different: When a semi-circular DOS is applied, the DOS at the relevant on-site energies (0 to 2), where particles are taken out of the bath, is larger. Therefore, these sites couple stronger to the chain and more particles are flowing into the tight-binding chain.
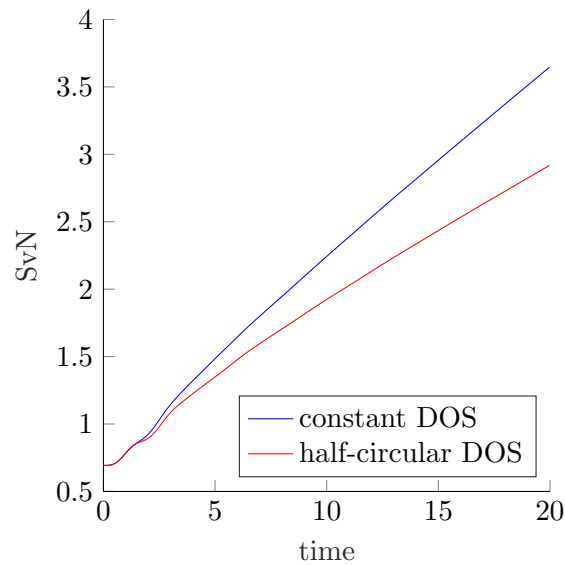

Figure 23: Entanglement entropy for both a constant and a semi-circular DOS with bandwidth 3 in the left bath and star geometry.
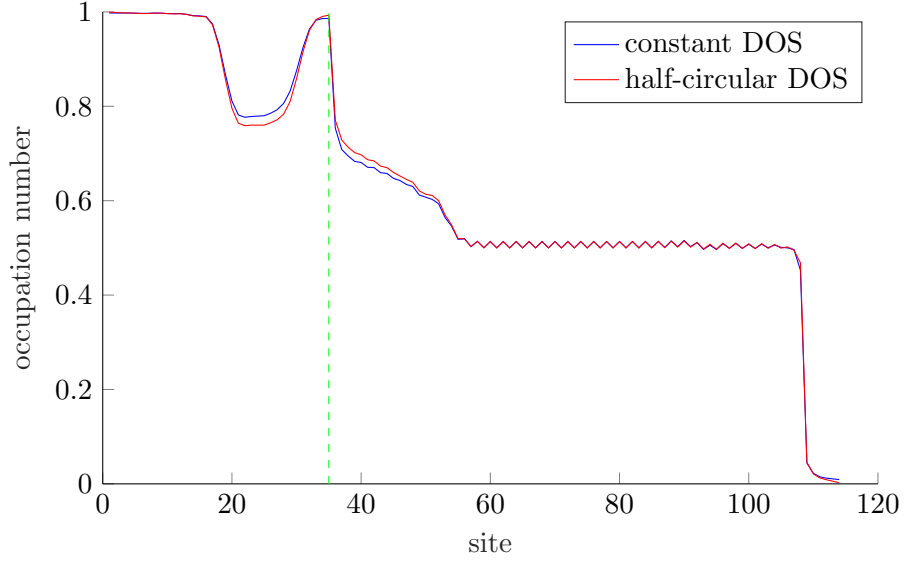
Figure 24: Occupation number for all sites at $t = 10$. The left bath has star geometry and a semi-circular and constant DOS, respectively. The vertical green line denotes the transition between bath and chain.

The same thing was done again but for a chain geometry. Again, a constant DOS and a semi-circular DOS were used for the bath with 35 sites and a tight-binding chain from sites 36 to 108 coupled to it. Fig. 25 shows the entanglement entropy on the first bond of the chain for both the constant DOS and the semi-circular DOS of the chain geometry bath. This figure is similar to fig. 23, where the same system, but a star geometry bath, was simulated: In both cases, a linearly increasing entanglement entropy can be seen. Regarding the occupation numbers, the chain geometry bath shows a different picture in fig. 26: Now, particles are taken out from all sites across the bath which leads to different occupation numbers in the left bath. However, the occupation numbers in the middle chain must be the same as both the star and the chain geometry represent the same bath coupled to the tight-binding chain.
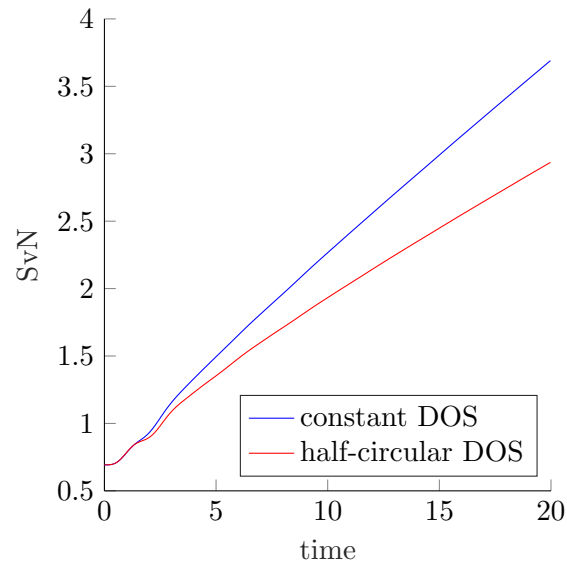
Figure 25: Entanglement entropy for both a constant and a semi-circular DOS with bandwidth 3 in the left bath and chain geometry.
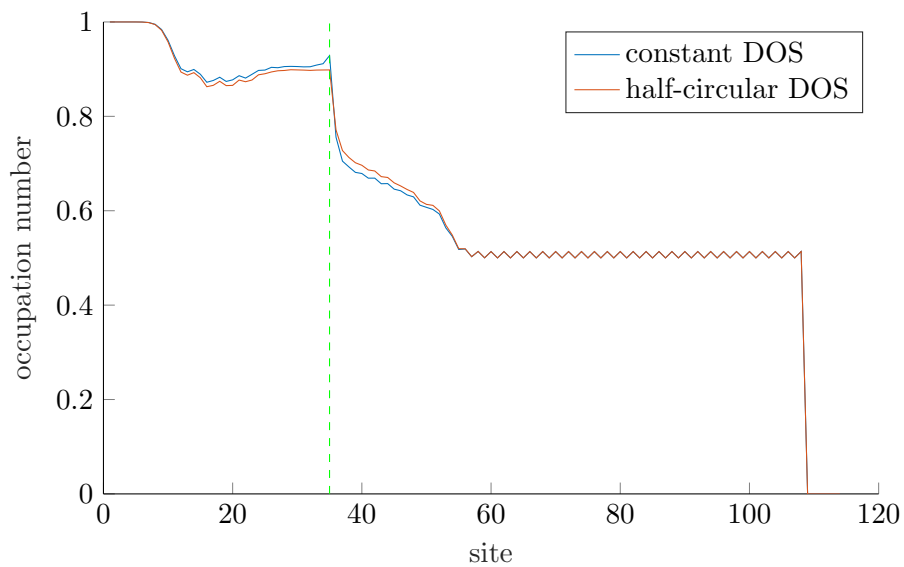

Figure 26: Occupation number for all sites at $t = 10$. The left bath has chain geometry and a semi-circular and constant DOS, respectively. The vertical green line denotes the transition between bath and chain.

4.2.4   Steady State Current

The current flowing through the tight-binding chain eventually converges towards a steady state. The amplitude of this steady state is the same for all sites in the chain and depends on the area of the DOS. Calculations were performed for two systems with a constant DOS and a bandwidth ranging from -6 to 6. However, the second DOS was not normalized and had twice the area of the first one. Therefore, a larger value for the steady state current could be observed in fig. 27.
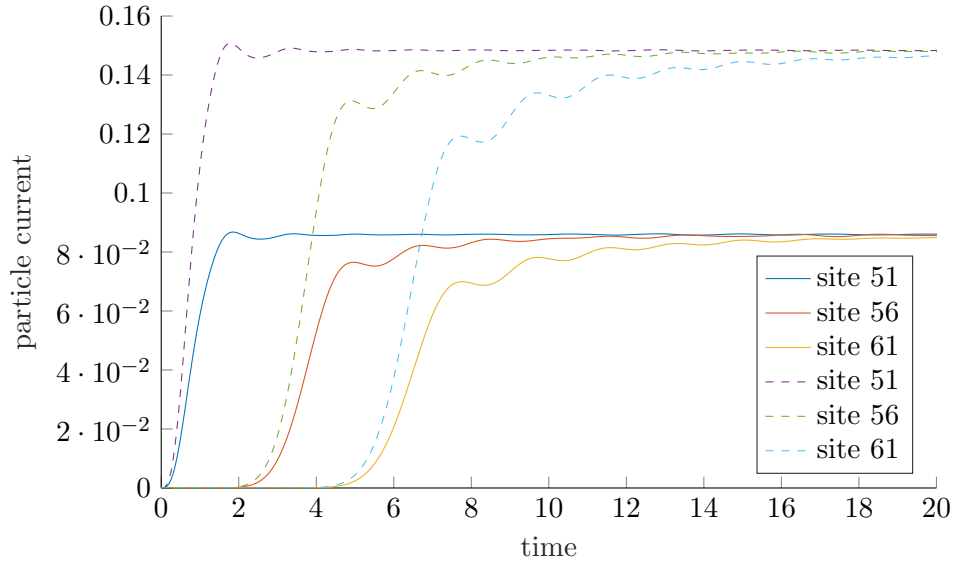

Figure 27: Steady state current in the tight-binding chain on sites 51, 56 and 61. The chain has 100 sites and is coupled to two star geometry baths with 50 sites. The DOS is constant ranging from -6 to 6 and has an area of 1 (solid lines) and 2 (dashed lines). For a larger area of the DOS and therefore larger coupling parameters, the steady state current is also higher.

The same holds true for the number of particles on the same sites: It will also increase until a certain steady state value is achieved which is again dependent on the area of the DOS. However, the particle number steady state is not the same for all sites in the chain. The results can be found in fig. 28
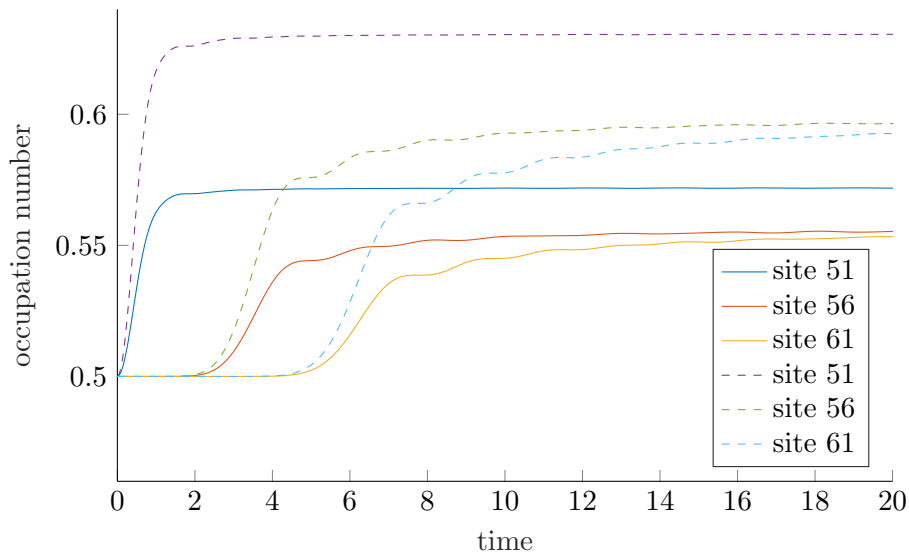
46

Figure 28: Steady state occupation number in the tight-binding chain on sites 51, 56 and 61. The chain has 100 sites and is coupled to two star geometry baths with 50 sites. The DOS is constant ranging from -6 to 6 and has an area of 1 (solid lines) and 2 (dashed lines). For a larger area of the DOS and therefore larger coupling parameters, the steady state occupation number is also higher.

4.2.5   Convergence

For both the chain and the star geometry, the convergence of the entanglement entropy was observed for different bath sizes and bandwidths D.

In the case of a Wilson chain geometry bath, a tight-binding chain with 100 sites was coupled to a left bath with 50, 100 and 150 sites. In order to ensure the same discretization of the on-site energies, the bandwidth D of the constant DOS also had to be changed to $D = 3$, 6 and 9, respectively. The calculations can be found in fig. 29 and show that for $D = 6$, the calculations are already well converged. For a fixed D, the baths with size 50, 100 and 150 coincide.

Figure 29: Entanglement entropy on the first bond of a tight-binding chain with 100 sites for a left bath in chain geometry with 50, 100 and 150 bath sites and $D = 3$, 6 and 9. While bath sizes larger than 50 sites have no visible impact on the entanglement entropy, a bandwidth of $D = 3$ is insufficient.

The same was done in the case of star geometry baths. However, beside the discretization of the on-site energies, in the case of star geometry baths, one must also consider that increased coupling parameters result in a higher particle flow and different entropies. Therefore, the coupling parameters also had to be scaled according to the bandwidth D. The tight-binding chain with 100 sites was coupled to baths with 51,102 and 153 sites. Also, a clear difference between the bath with 101 and with 102 bath sites can be seen in fig. 30.
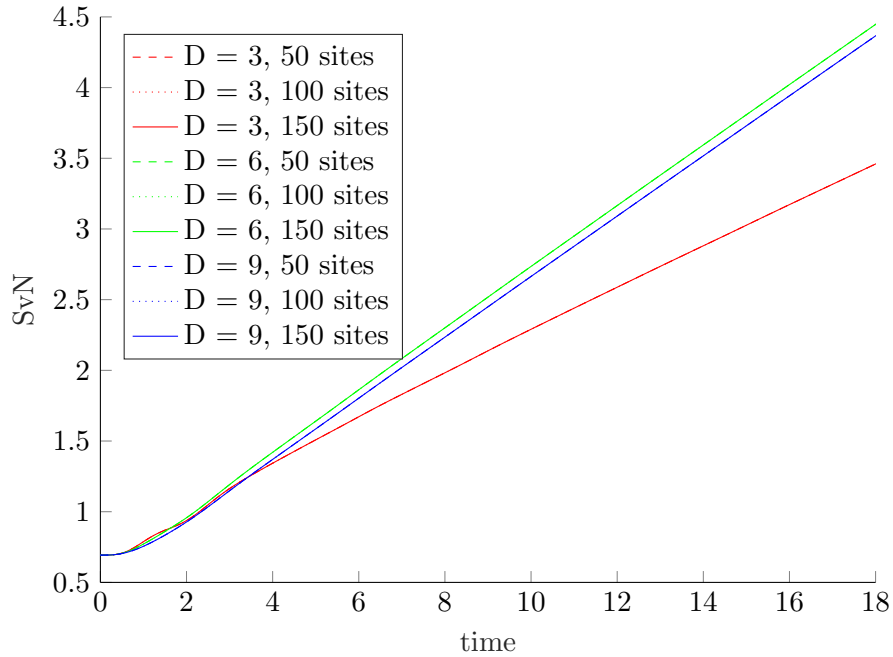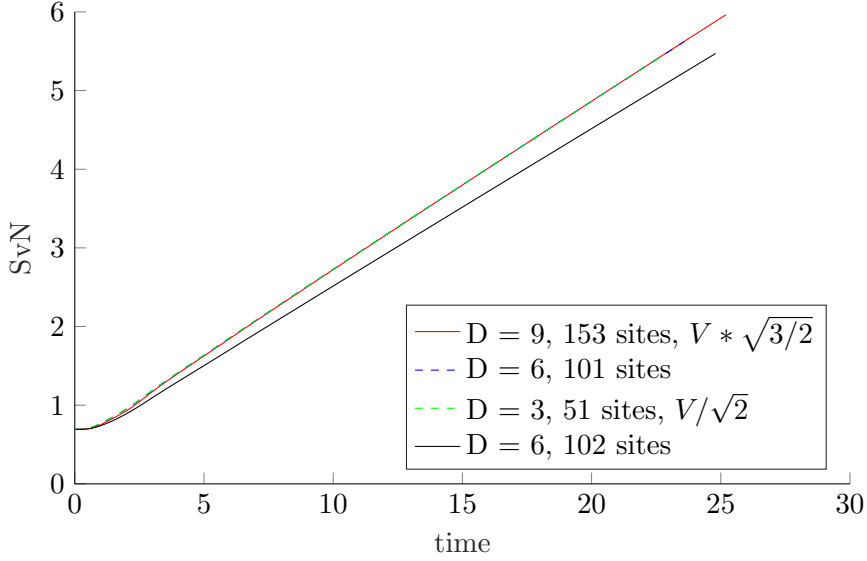
Figure 30: Entanglement entropy on the first bond of a tight-binding chain with 100 sites for a left bath in star geometry with 51, 101, 102 and 153 bath sites and $D = 3, 6, 6$ and 9. In order the achieve comparable results, the coupling parameters V also have to be scaled.

4.2.6 Current Induced by a Chemical Potential Gradient

One can also obtain a current by introducing an electric potential by adding a chemical potential. The chemical potential has to be different between the two baths and rises linearly in the tight-binding chain.[23] In that case, the whole chain is initially half-filled as the potential difference is now not achieved by different fillings of the baths. However, now a Hubbard chain as introduced in eq. 11 was coupled to the baths:

$$H = -t'' \sum_{i\sigma} \left(c_{i\sigma}^\dagger c_{i+1\sigma} + c_{i+1\sigma}^\dagger c_{i\sigma} \right) + U \sum_{i\sigma} n_{i\sigma} n_{i\bar{\sigma}}$$

In both baths, a hopping parameter of $t' = 1$ was chosen. In the Hubbard chain, the hopping parameter was set to $t'' = 0.2$ and an on-site repulsion of $U = 1$ was chosen. The on-site energy in the left (right) bath was set to $\epsilon = -1$ ($\epsilon = +1$). In the middle region, the on-site energy was increasing linearly from -1 to 1 and an additional on-site energy $\epsilon_0 = -U/2 = -1/2$ was added to achieve half-filling. The time evolution leads to the following behaviour of the entanglement entropy on all bonds (see fig. 31). These results are in very good agreement with the results from [23].
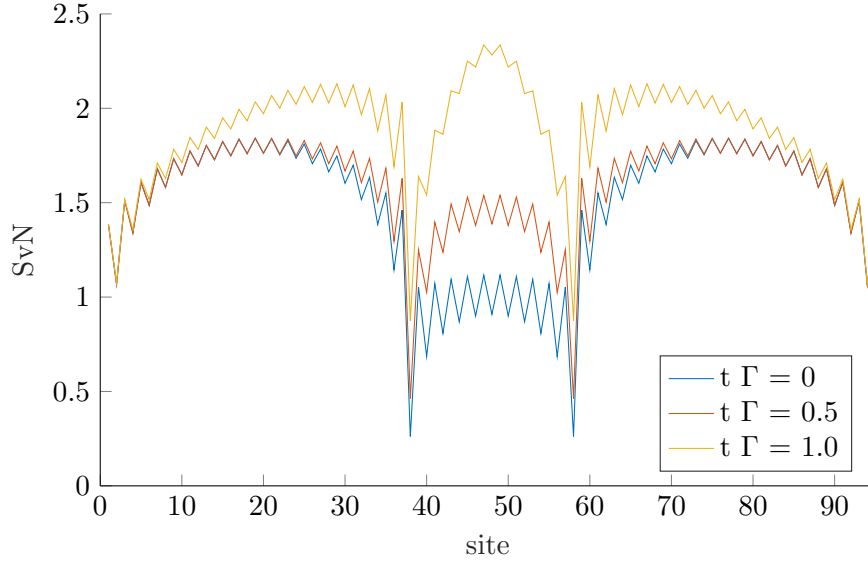
Figure 31: Entanglement entropy at different times tΓ ($\Gamma = 2t''^2$) for all bonds.

For the same simulation, the particle current was also measured and can be found in fig. 32. The behaviour of the current is also in good agreement with [23] as a steady state current is reached at $t\Gamma = 1$.
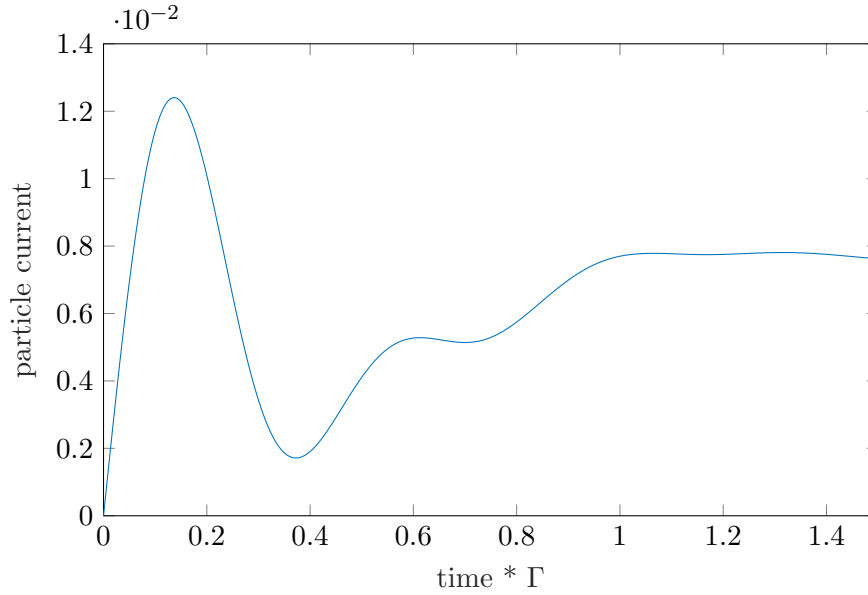
Figure 32: Particle current going through the Hubbard chain, obtained by averaging over the current going through the first and the last site of the system. The current was induced by a bias voltage $\Delta V = 2$ between the baths and the Hubbard chain has a hopping parameter $t'' = 0.2$ and a Coulomb repulsion $U = 1$.

5 Thermal Current

5.1 Thermal Transport

This chapter covers thermal energy transport in one-dimensional systems. At first, the concept of a local energy current is defined for a Fermi-Hubbard model. Then, the approach of Karrasch[22] to study thermal currents in the Fermi-Hubbard model is presented, closely following his paper. Finally, an overview of both theoretical and experimental results regarding thermal current in Hubbard and Spin 1/2 chains is given. The Hamiltonian for the Fermi-Hubbard model is given by a sum of local terms:

$$H = \sum_n h_n \tag{117}$$

with the local terms

$$
\begin{aligned}
h_n = & -\frac{t_0}{2}(c_{n\uparrow}^\dagger c_{n+1\uparrow} + c_{n\downarrow}^\dagger c_{n+1\downarrow} + H.c.) + \\
& \frac{U}{2}(\tilde{n}_{n\uparrow}\tilde{n}_{n\downarrow} + \tilde{n}_{n+1\uparrow}\tilde{n}_{n+1\downarrow}) + \\
& V(\tilde{n}_{n\uparrow} + \tilde{n}_{n\downarrow})(\tilde{n}_{n+1\uparrow} + \tilde{n}_{n+1\downarrow})
\end{aligned}
\tag{118}
$$

where $c_{n\sigma}$ ($c_{n\sigma}^\dagger$) is the annihilation (creation) operator for a fermion on site n with spin σ and $\tilde{n}_{n\sigma} = c_{n\sigma}^\dagger c_{n\sigma} - 1/2$. U and V denote the on-site Coulomb and nearest-neighbour interactions, respectively. However, in this thesis we will mostly consider only a tight-binding chain where $U = 0$ and $V = 0$. Finally, we will also switch an on-site Coulomb repulsion $U \neq 0$ on. The hopping matrix element t_0 was set to 1 and all quantities like the energy current or the time are given in units of t_0. The local energy current is defined by

$$j_{E,n} = i[h_{n+1}, h_n] \tag{119}$$

Considering only the tight-binding contribution in eq. 118, the thermal energy current is given by

$$j_{E,n} = \sum_\sigma i\frac{t_0^2}{4}(c_{n+2\sigma}^\dagger c_{n\sigma} - H.c.) \tag{120}$$

The explicit calculation can be found in Appendix A.5.
In the case of a non-zero on-site Coulomb interaction U, a tedious calculation[3] leads to the following thermal energy current:

---

[3]The calculation was performed explicitly and works similar to the calculation for the tight-binding contribution as shown in Appendix A.5.

$$j_{E,n} = \sum_\sigma i\frac{t_0^2}{4}(c_{n+2\sigma}^\dagger c_{n\sigma} - H.c.) +$$
$$\sum_\sigma i\frac{Ut_0}{4}(c_{n\sigma}^\dagger c_{n+1\sigma} + c_{n+1\sigma}^\dagger c_{n+2\sigma} - H.c.)\,\tilde{n}_{n+1\bar\sigma} \tag{121}$$

where $\bar\sigma = \uparrow$ if $\sigma = \downarrow$ and vice versa.

Eqs. 120 and 121 are in perfect agreement with [25].

In order to establish a temperature gradient, one can divide the chain into a left and right part represented by density matrices ρ_L and ρ_R which were initialized as thermal density matrices with different temperatures T_L and T_R:

$$\rho_L \sim e^{-H/T_L}, \quad \rho_R \sim e^{-H/T_R} \tag{122}$$

and

$$\rho_0 = \rho_L \otimes \rho_R \tag{123}$$

However, Karrasch took a numerically more advantageous way and modelled the bond between the two parts of the chain smoothly by introducing

$$\rho_0 \sim e^{-\tilde{H}} \tag{124}$$

where the temperature gradient is established by defining $\tilde{H}$ as

$$\tilde{H} = \begin{cases} H/T_L, & n \leq 0 \\ H/T_R, & n > 0 \end{cases} \tag{125}$$

As expected, Karrasch could observe that the energy current $\langle j_E(t)\rangle$ converges towards a non-zero steady state value in the case of $V = 0$. If there are non-vanishing nearest-neighbour interactions, the current decays to zero. He also found that this steady state current has the following dependence on T_L and T_R:

$$\lim_{t\to\infty} \langle j_E(t)\rangle = f(T_L) - f(T_R) \tag{126}$$

Karrasch observed such steady state currents for a flow between two baths with different temperatures as well as from a bath into vacuum. He showed that a steady state current flowing out of the left part of the chain, which was initialized in equilibrium at T_L, can be approximately described by a universal function of its temperature:

$$\lim_{t\to\infty} \langle j_E(t)\rangle = f(T_L) + C \tag{127}$$

If the right part of the system is also a thermal system with initial temperature T_R, then this constant is given by $C = -f(T_R)$ which gives eq. 126.

Earlier, the non-equilibrium transport in spin chains was also studied by Karrasch et

al.[26]. They considered an XXZ spin 1/2 chain where the integrability was broken by two perturbations. DMRG methods were applied in order to establish a temperature gradient in the initial state. They found that the (thermal) energy current of the system, which is driven by this temperature gradient, would relax fast into a finite steady state value if the Drude weight D is non-zero. Similar to [22] and the results in this thesis, the steady state current takes the form

$$J_E(T_L, T_R) = f(T_L) - f(T_R) \tag{128}$$

where T_L is the initial temperature of the left part of the chain and T_R is the initial temperature of the right part of the chain. This was obtained by separating the whole chain into two semi-infinite chains. In the initial state, both semi-infinite chains are in thermal (grand-canonical) equilibrium at temperatures T_L and T_R. These states are represented by density matrices. Eq. 128 implies that the non-equilibrium thermal transport in this system is entirely determined by linear response as the function f can simply be obtained by integration of the equilibrium conductance $\partial_T f$. Thus, the value of the steady state (thermal) energy current is completely determined by the linear thermal conductance.

A similar system was discussed in [27]. In this case, a spin chain with local Hamiltonians of the form

$$h_n = J_n \left(S_n^x S_{n+1}^x + S_n^y S_{n+1}^y + \Delta_n S_n^z S_{n+1}^z \right) + b_n \left(S_n^z - S_{n+1}^z \right) \tag{129}$$

was studied. In order to investigate the finite-temperature transport properties of this system, DMRG was applied and the thermal statistical operator was obtained via purification. Similar to the ideas above, the whole chain was again divided into a left and right part with equilibrium temperatures T_L and T_R, respectively, in the initial state. To enable the interaction, two approaches were shown: The two parts could either be coupled directly at time $t = 0$ or via an interacting resonant level model (IRLM). The calculations were also performed by applying MPS where a rapid growth of the matrix bond dimensions during the time evolution was observed. For the steady state current, the same relation as stated in eq. 128 was observed. They also investigated the dependence of the steady state (thermal) energy current from the matrix dimension and the discarded weight, respectively: Too small matrix bond dimensions lead to high truncation errors. As these discarded weights get larger and larger, the steady state gets represented worse and worse. Instead of a constant current, stronger and stronger oscillations around the steady state value can be observed as the truncation errors increase. For longer times, a (too small) fixed bond dimension will eventually lead to completely wrong results. To tackle this problem of rapidly increasing bond dimensions, they reduce the growth of entanglement by "time-evolving the auxiliary degrees of freedom which purify the thermal statistical operator."

Both particle and energy transfer in an XXZ chain were studied by Vasseur et al.[28]. They studied the rates of energy and particle densities moving through systems with temperature and chemical potential differences. In the initial state, the XXZ spin chain

was separated into two parts: A left part with μ_L and T_L as well as a right part with μ_R and T_R. After some oscillations at the beginning, the energy current $j_E(t)$ finally converges towards a steady state energy current as the oscillations quickly decrease.

One-dimensional thermal transport initiated by a linear response can also be realized in quasi-1D spin systems.[22] Experiments investigating the energy transport in spin-chain and spin-ladder materials with antiferromagnetic coupling are discussed in [29]. In this paper, Sologubenko et al. state that recent experimental results, especially in spin 1/2 chains, are consistent with theoretical results which claim a ballistic form of transport. One-dimensional spin 1/2 systems are also experimentally studied in [30] where Hlubek et al. investigate high purity samples of $SrCuO_2$ which is a chain cuprate that is considered to be an excellent realization of the spin 1/2 Heisenberg chain: The magnetic susceptibility of $SrCuO_2$ single crystals was quantitatively compared to theoretical calculations and showed excellent agreement.[31] Hlubek et al. studied the scattering processes in the system and found that only extrinsic scattering processes played a role in the limitation of the magnetic heat conductivity. This is a manifestation of the ballistic nature of the thermal energy transport in the spin 1/2 Heisenberg chain. Quantum spin 1/2 chains were also considered in [32], where XX spin chains were coupled to an XX chain and an XY chain which both had different temperatures. The heat currents were studied by applying a non-equilibrium Green's-function formalism. They also studied the effect of magnetic fields acting on those thermal reservoirs and found that when a magnetic field is applied at the end chains, one can observe different magnitudes for the thermal current depending on the direction in which the temperature difference is applied. They call this the "thermal-diode effect". Actually, the experimental measurement of the thermal conductivity of a system is way harder than measuring e.g. the electrical current. This might be a reason why it took until the last few years until experimental studies, investigating thermal conductivity with respect to system size in low dimensional systems, were realized. These experiments became possible due to the advances in nanophysics, making it feasible to realize systems like nanowires or nanotubes, suspended between thermal reservoirs.[33]
In [34], finite temperature charge transport is simulated and a ballistic charge transport behaviour is observed in the one-dimensional Hubbard model. A nonintegrable model in the form of a mass-imbalanced Hubbard chain is also considered. However, thermal transport in the one-dimensional Hubbard model is ballistic at any finite temperature $T > 0$. [25, 35] An approach via DMRG was chosen by Karrasch et al. in [35], where they study the thermal conductivity of the 1D Fermi-Hubbard model at finite temperatures. For the integrable case, they can confirm ballistic transport. If the integrability is broken through nearest-neighbour interaction, this leads to diffusive energy transport. Concerning an experimental realization of the charge and energy transport in Fermi-Hubbard models, they mention quantum gas microscope experiments as performed in [36]. Ultracold ^{40}K atoms were also considered in [37], where they studied a 2D Fermi Hubbard model and were able to observe metallic, Mott-insulating and band-insulating states. They were also able to measure the entropy per particle and suggest that the

Mott insulator could provide a well-controlled initial state for studying one-dimensional Hubbard chains.

In the present thesis, thermal currents flowing through tight-binding and Hubbard chains are studied. The thermal energy currents are initiated by coupling thermal baths at different temperatures onto both sides of the chain. These thermal baths are modelled by applying the thermofield approach.[2]

5.2 Purification

The method of purification is the usual approach to obtain finite temperature states. The method is described in [1], which this section closely follows.

The purification works for an arbitrary mixed state with physical space P formed from orthonormal states:

$$\rho_P = \sum_a s_a^2 |a\rangle_P {}_P \langle a| \tag{130}$$

This state can now be interpreted as the result of a partial trace over a Schmidt decomposition of a pure state on PQ, where Q is an auxiliary space:

$$|\Psi\rangle = \sum_a s_a |a\rangle_P |a\rangle_Q \quad \Rightarrow \quad \rho_P = Tr_Q |\Psi\rangle \langle \Psi| \tag{131}$$

However, the introduction of the auxiliary space Q means that the Hilbert space has to be locally doubled:
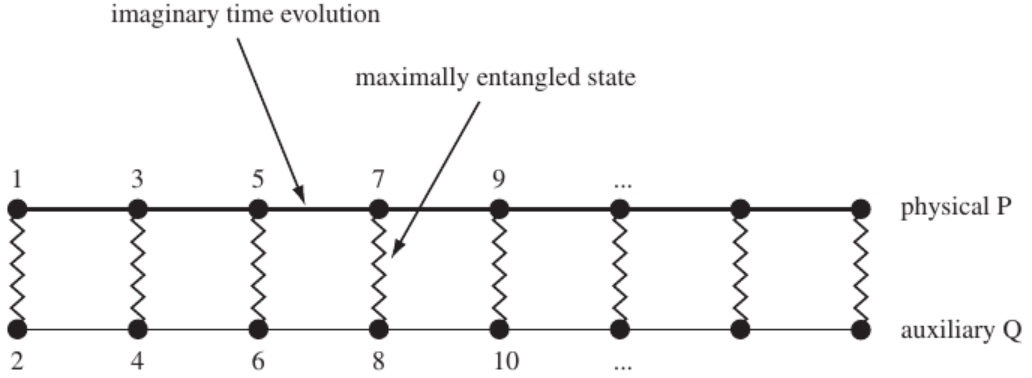

Figure 33: Graphical representation of the local Hilbert space doubling where P is the physical space and Q is the auxiliary space. This figure was taken from [1].

The thermal density operator is given by

$$\rho_\beta = Z(\beta)^{-1} e^{-\beta H}, \quad Z(\beta) = Tr_\rho e^{-\beta H} \tag{132}$$

and can be written as

$$\rho_\beta = Z(\beta)^{-1} e^{-\beta H} = Z(\beta)^{-1} e^{-\beta H/2} \, \mathbb{1} \, e^{-\beta H/2} \tag{133}$$

Now, the identity matrix $\mathbb{1}$ can be interpreted as $Z(0)\rho_0$, the infinite temperature density operator times the infinite temperature partition function. If we assume that we know the purification of ρ_0 as an MPS $|\Psi_{\beta=0}\rangle$, we can write

$$\rho_\beta = \frac{Z(0)}{Z(\beta)} e^{-\beta H/2} Tr_Q \left|\Psi_0\right\rangle \left\langle\Psi_0\right| e^{-\beta H/2}$$

$$= \frac{Z(0)}{Z(\beta)} Tr_Q e^{-\beta H/2} \left|\Psi_0\right\rangle \left\langle\Psi_0\right| e^{-\beta H/2} \tag{134}$$

As Q is only an auxiliary space, Tr_Q can be pulled out in front and one can see that there has an imaginary time evolution to be done:

$$\left|\Psi_\beta\right\rangle = e^{-\beta H/2} \left|\Psi_0\right\rangle \tag{135}$$

Therefore, the remaining task is to find $\left|\Psi_0\right\rangle$, perform an imaginary time evolution and then calculate expectation values as for a pure state. A time evolution at finite temperature can now be applied on $\left|\Psi_\beta\right\rangle$.

5.3 Thermofield Approach

This section closely follows [2], in which de Vega and Bañuls applied the concept of a thermofield approach to simulate the evolution of open quantum systems coupled to baths at finite temperature. This approach was then used in the present thesis as an alternative to purification to model thermal baths. By applying this approach, one can efficiently simulate the evolution of fermionic (or bosonic) systems coupled to thermal reservoirs. Notably, this can be done without a previous preparation by purification which would include an imaginary time evolution and in the context of MPS, one can initialize the thermal bath as a product state.

Consider an environment of harmonic oscillators with annihilation (creation) operators b_k ($b_k^\dagger$) and frequencies ω_k. The Open Quantum System (OQS) couples with strength g_k. The complete Hamiltonian reads

$$H_{tot} = H_S + H_B + \sum_k g_k(L^\dagger b_k + b_k^\dagger L) \tag{136}$$

with the Hamiltonian of the OQS H_S, $H_B = \sum_k \omega_k b_k^\dagger b_k$ and L the coupling operator acting on the OQS Hilbert space. Then, an auxiliary, decoupled environment with annihilation (creation) operators c_k ($c_k^\dagger$) is added. This leads to the total Hamiltonian of the form

$$\hat{H}_{tot} = H_{tot} - \sum_k \omega_k c_k^\dagger c_k \tag{137}$$

Assuming that both environments are initially in a thermal state at the inverse temperature β, a thermal Bogoliubov transformation is applied. For fermionic reservoirs, this transformation reads

$$a_{1k} = e^{-iG} b_k e^{iG} = \cos(\theta_k) b_k - \sin(\theta_k) c_k^\dagger$$

$$a_{2k} = e^{-iG} c_k e^{iG} = \cos(\theta_k) c_k + \sin(\theta_k) b_k^\dagger \tag{138}$$

Here, $G = i \sum_k \theta_k (b_k^\dagger c_k^\dagger - c_k b_k)$ where θ_k is temperature dependent

$$\cos(\theta_k) = \sqrt{1 - n_k}$$
$$\sin(\theta_k) = \sqrt{n_k} \tag{139}$$

with $n_k = 1/(e^{\beta \omega_k} + 1)$, the number of excitations in mode k. The explicit calculation of eqs. 138 can be found in appendix. A.2.

Using this transformation, the following Hamiltonian is obtained

$$\tilde{H}_{tot} = H_S + \sum_k \omega_k (a_{1k}^\dagger a_{1k} - a_{2k}^\dagger a_{2k}) +$$
$$\sum_k g_{1k}(L^\dagger a_{1k} + a_{1k}^\dagger L) + \sum_k g_{2k}(L a_{2k} + a_{2k}^\dagger L^\dagger) \tag{140}$$

with $g_{1k} = g_k \cos(\theta_k)$ and $g_{2k} = -g_k \sin(\theta_k)$. The mathematical calculation can be found in appendix A.3 and shows that using these transformations, H_{tot} can actually be transformed into $\tilde{H}_{tot}$.

However, this version of $\tilde{H}_{tot}$ does not conserve the particle number. Therefore, a particle hole transformation for the auxiliary bath a_{2k} was applied. This transforms the last part of the Hamiltonian in the following way:

$$L a_{2k} + a_{2k}^\dagger L^\dagger \Longrightarrow L a_{2k}^\dagger + a_{2k} L^\dagger = -(a_{2k}^\dagger L + L^\dagger a_{2k}) \tag{141}$$

Therefore, in the thermal vacuum, the sites of the bath a_{1k} are completely empty whereas the sites of the auxiliary bath a_{2k} are completely filled in the initial state.

By using this transformation, one gets a thermal vacuum. This thermal vacuum reads

$$|\Omega\rangle = e^{-iG} |\Omega_0\rangle \tag{142}$$

where $|\Omega_0\rangle$ is the vacuum for the b_k and c_k modes. Comparing eq. 142 with eq. 138, one can immediately see that $|\Omega\rangle$ is indeed a vacuum state for the a_{1k} and a_{2k} modes.

Another representation of the thermal vacuum is, up to normalization, given by

$$|\Omega\rangle \propto e^{-\beta H_B/2} |I\rangle \tag{143}$$

with $|I\rangle = \sum_n |n\rangle_b |n\rangle_c$ being the maximally entangled state between the real and the auxiliary environments with their eigenstates $|n\rangle_b$ and $|n\rangle_c$. In the case of fermions, this state is given by $|I\rangle = |0\rangle_b |0\rangle_c + |1\rangle_b |1\rangle_c$. For this representation however, it is not so clear that this is also a representation of the thermal vacuum. The mathematical calculation can be found in appendix A.4.

The approach described above was also tested in [2] on a fermionic environment in which a quantum dot was coupled to an electronic reservoir at finite temperature. Spin expectation values were calculated and successfully tested against tDMRG results: The dynamics of the quantum system were coupled to the thermal reservoir and could be

integrated both in the case of fermionic and bosonic systems. This was done in a pure state formalism but without the need of a previous preparation of the thermal state with imaginary time evolution. Instead, the thermal Bogoliubov transformation described above was applied. The time evolution of the system was done by applying MPS techniques.

Another useful application for the thermofield approach can be found in [38], where Schwarz et al. use the thermofield approach to study steady state non-equilibrium systems in the context of NRG. Usually, NRG faces some limitations in the case of steady-state non-equilibrium systems e.g. if a bias voltage is applied. Comparing their results with several benchmarks, they could show that these limitations can be overcome if the thermal baths are described with the thermofield approach. By combining the thermofield approach with a NRG-DMRG quench, one can obtain quantitatively reliable results for quantum impurity models in steady state non-equilibrium.

5.4   Results

This section considers a thermal energy current flowing through an initially empty tight-binding chain. Later, also a Hubbard chain will be considered. The energy current is given by the commutator of local Hamiltonians as introduced in eq. 118

$$
h_n = -\frac{t_0}{2}(c_{n\uparrow}^\dagger c_{n+1\uparrow} + c_{n\downarrow}^\dagger c_{n+1\downarrow} + H.c.) +
$$
$$
\frac{U}{2}(\tilde{n}_{n\uparrow}\tilde{n}_{n\downarrow} + \tilde{n}_{n+1\uparrow}\tilde{n}_{n+1\downarrow}) +
$$
$$
V(\tilde{n}_{n\uparrow} + \tilde{n}_{n\downarrow})(\tilde{n}_{n+1\uparrow} + \tilde{n}_{n+1\downarrow})
$$

and a rather tedious calculation (for $V = 0$) leads to the energy current as introduced in eq. 121

$$
j_{E,n} = \sum_\sigma i\frac{t_0^2}{4}(c_{n+2\sigma}^\dagger c_{n\sigma} - H.c.) +
$$
$$
\sum_\sigma i\frac{Ut_0}{4}(c_{n\sigma}^\dagger c_{n+1\sigma} + c_{n+1\sigma}^\dagger c_{n+2\sigma} - H.c.)\,\tilde{n}_{n+1\bar{\sigma}}
$$

In order to obtain such a thermal energy current, thermal baths were coupled to the chain on both sides. The thermal baths were obtained through a thermofield approach as introduced in chap. 5.3:
One starts with a bath in star geometry. By introducing an auxiliary bath for each thermal bath and performing a Bogoliubov transformation, one obtains a thermal vacuum containing the information of the temperature of the bath. After performing a particle hole transformation, the bath (a_{1k}) still is initially completely empty but the auxiliary bath (a_{2k}) is initially completely filled. Both baths couple to the chain and these coupling parameters are temperature dependent.
The DOS of the bath was chosen constant. However, the convergence rate towards the steady state thermal energy current was strongly depending on the area of the DOS. For certain values, the thermal current would converge quite fast towards the steady state current whereas for higher or lower areas, the current showed strong oscillations. In the following results, a DOS area which guarantees fast convergence was chosen.
The calculations were performed applying both TEBD and TDVP as introduced in chapters 3.4 and 3.5. Simulations applying TEBD showed an exponentially increasing bond dimension with time. Therefore, the total simulation time was limited. Applying TDVP made it possible to obtain equally accurate results but using smaller bond dimensions. The one-site TDVP algorithm will be denoted as TDVP1 and similarly, the two-site TDVP algorithm will be denoted as TDVP2.
As the time until the system chain is in equilibrium strongly depends on the length of the chain, calculations were, unless otherwise noted, performed for a chain length of 3 as this is the minimum length required to measure the thermal current as defined in eq. 121.

5.4.1 Fixed Temperature in Right Bath

Like in [22], the thermal current for different temperatures in the left bath was calculated. The temperature of the right bath was kept constant at $\beta_R = 0$ and $\beta_R = 1$, respectively. The tight-binding chain in the middle had 3 sites and was connected to the two 50 sites large baths with different temperatures. The thermal current was always measured on the first site of the impurity (site 51). The results can be found in fig. 34 and are in very good agreement with the results from [22], which can also be seen in fig. 35.
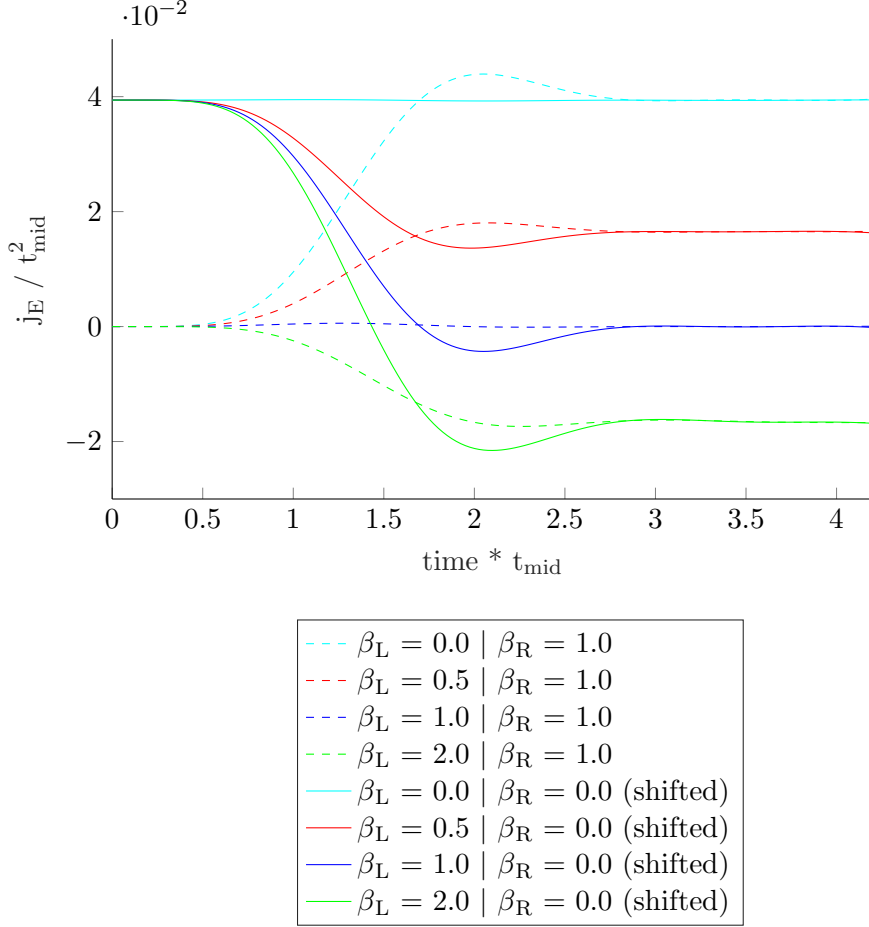

Figure 34: Thermal current for constant $\beta_R = 0$ and $\beta_R = 1$ with different β_L. After shifting the curves with the same $\beta_R = 0$ vertically, they all converge towards the same steady state current as the curve with the same β_L and $\beta_R = 1$. The time evolution was performed by applying TDVP2.

The occupation number plot for one of the simulations from fig. 34 with $\beta_L = 0.5$ and $\beta_R = 0.0$ can be found in fig. 36. The occupation number of the baths clearly shows the thermal vacuum: The bath is initially empty and the auxiliary bath is initially filled

as a particle hole transformation was performed. The chain in the middle eventually reaches a steady state where all sites are half-filled. Fig. 35 shows the results obtained by Karrasch in [22], where he also simulated the thermal current flux for the integrable model and β_R was fixed to $\beta_R = 0, 1, 2$. However, he uses a model with an interaction strength of $U = 1$ and $U = 4$ (see eq. 118) in fig. 35 (a),(b) and (c),(d), respectively.
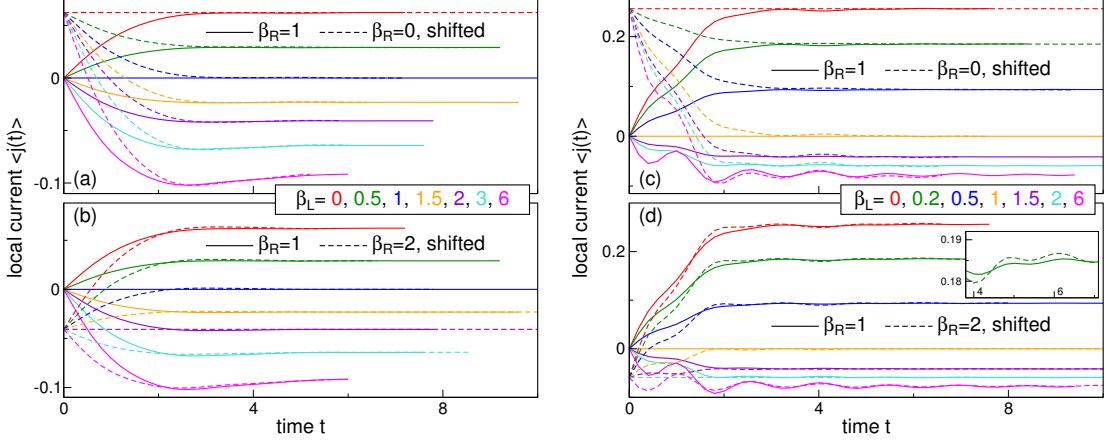

Figure 35: Results for the thermal flux between baths at different temperatures from Karrasch[22]. The results are calculated for the integrable model with interaction $U = 1$ in (a),(b) and $U = 4$ in (c),(d). However, Karrasch applies the method of purification to obtain the thermal baths in contrast to the thermofield approach which was chosen in this thesis. Still, there is a very good qualitative agreement with fig. 34 regarding the steady state behaviour of the thermal current: The currents for a certain β_R are shifted vertically until they overlap with the steady state values for a different β_R and the respective values for β_L. All currents are shifted for the same value.
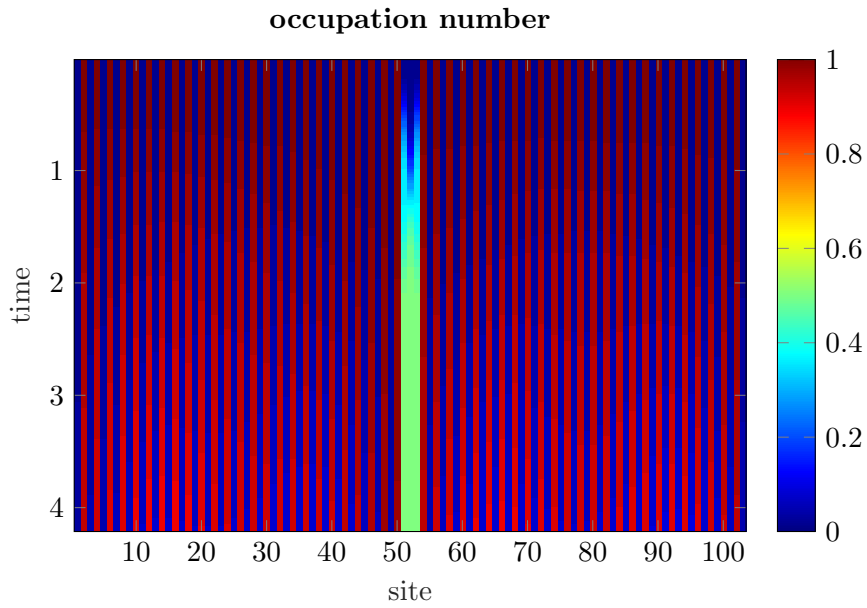
occupation number

Figure 36: Occupation number on all sites for the thermal system with $\beta_L = 0.5$ and $\beta_R = 0.0$. The initially full bath sites get emptied as the middle chain converges towards half-filling and some particles also flow into the empty bath sites.

5.4.2 Convergence

The simulation time is limited by the size of the baths as finite size effects occur and destroy the steady state. As mentioned before, the time it takes the system to go into the steady state thermal energy current strongly depends on the area of the constant DOS. For all the calculations above, an area that achieves optimal convergence was chosen for the DOS. In fig. 37, the dashed line depicts the area with the fastest convergence towards the steady state. Fig. 37 also shows that, compared to the optimal value which was found to be $A = 2.25$, both too large as well as too small areas cause large oscillations in the thermal energy current, making it impossible to obtain a steady state within reachable simulation time.
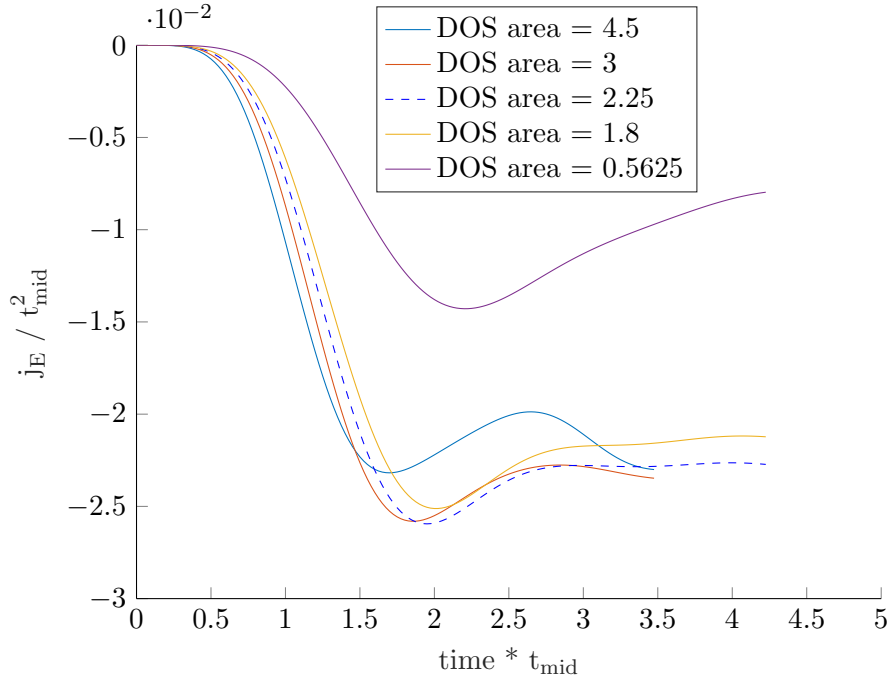
Figure 37: Comparison of the thermal current for different baths which only differ in the area of the constant DOS.

5.4.3 Hubbard Chain Simulations

The very same model as above can also be applied to a Hubbard chain instead of a tight-binding chain. However, introducing also spin down particles makes the problem of an exponentially increasing bond dimension even worse. These bond dimensions limit the maximum simulation time even stronger than for the case of a tight-binding chain. In order to obtain reliable results, the truncation errors were monitored and as they exceeded 10^{-8} because of the exponentially growing bond dimensions, the simulation was aborted.

Here, a Hubbard chain of length 3 was coupled to two baths with 30 sites and temperatures $\beta_L = 0.0$ and $\beta_R = 0.4$. The chain not only had a hopping parameter $t = 1$ but also on-site Coulomb repulsions of $U = 1, 4$ and 8. The initial state of the chain was empty but in this case, the full sites in the auxiliary bath a_{2k} are now filled not only with a spin up electron but also with a spin down electron. In this TEBD time evolution, the maximum bond dimension of 4200 was reached at around $t = 1.7$, leading to maximum truncation errors larger than 10^{-8} soon afterwards. The semi-logarithmic plot in fig. 38 shows the exponential growth of the bond dimension.
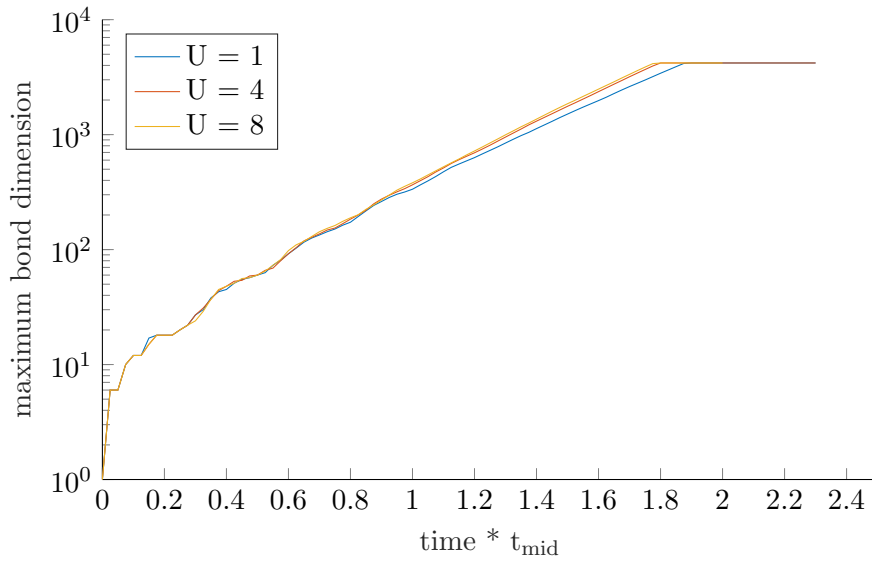
Figure 38: Semi-logarithmic plot of the maximum bond dimension growing with time clearly showing the exponential growth of the bond dimension for a system with a Hubbard chain with $U = 1, 4$ and 8. At around $t = 1.7$, the maximum bond dimension of 4200 was already reached and soon afterwards, truncation errors larger than 10^{-8} were observed.

The thermal current, which was calculated with eq. 121, can be seen in fig. 39. Obviously, the steady state has not been reached before the simulation had to be stopped due to exploding bond dimensions and truncation errors, respectively.
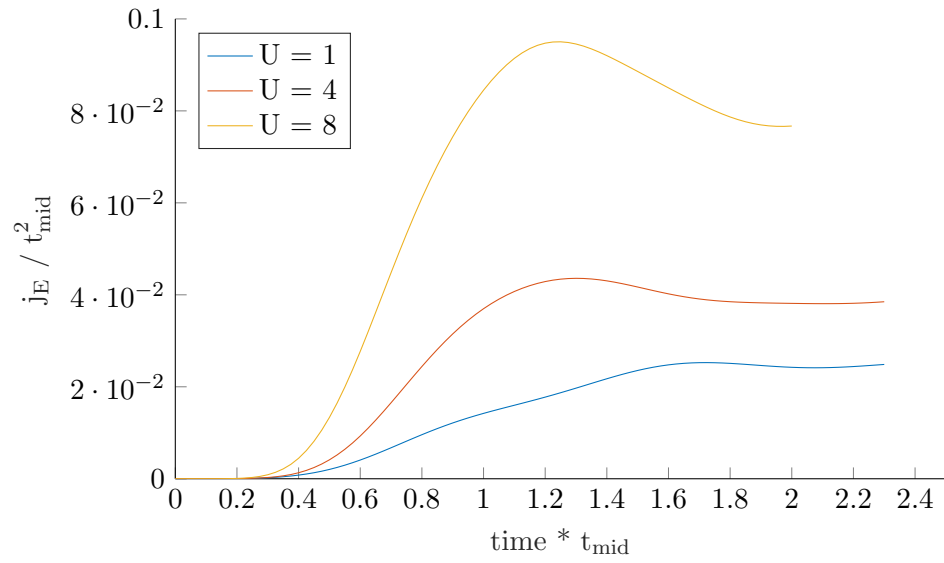
Figure 39: Thermal current for a Hubbard chain of length 3 with two baths with 30 sites at inverse temperatures $\beta_L = 0.0$ and $\beta_R = 0.4$. The simulation time is limited by the exponentially growing bond dimensions and therefore no steady state could be reached.

6 Comparison of TEBD and TDVP

The reason to apply TDVP were the exponentially increasing bond dimensions we faced in time evolutions applying TEBD. In [17], Leviatan et al. present very surprising results for time evolutions applying TDVP: They report that certain local quantities are conserved during time evolution, even for very small bond dimensions in the order of $\chi = 10$. Thus, TDVP was applied in the present thesis to investigate whether thermal energy current can also be accurately described with such small bond dimensions.

At first, the two-site TDVP algorithm TDVP2 was tested against TEBD results in the well known simulation which can be seen in fig. 34. Fig. 40 shows that both algorithms obtain correct results for a system with 50 bath sites at inverse temperatures $\beta_L = 0.5$ and $\beta_R = 0.0$ in the respective thermal baths.
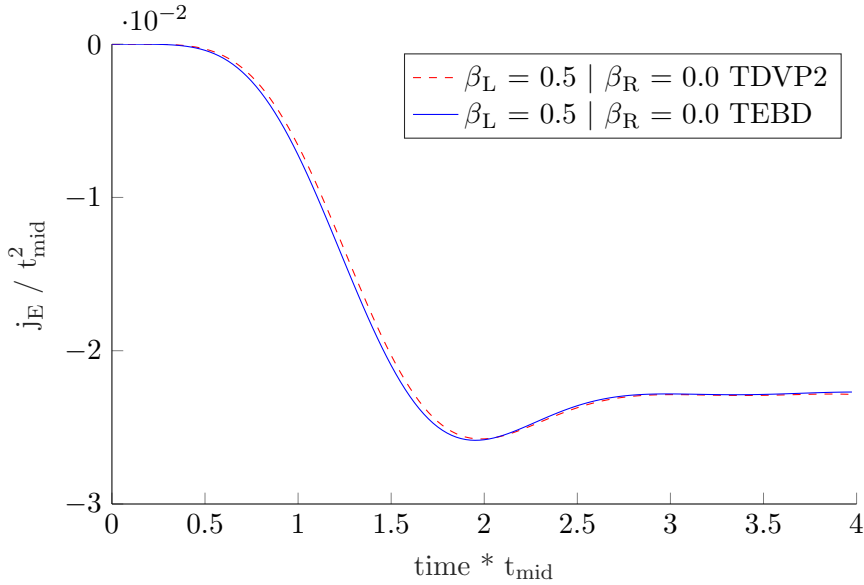

Figure 40: Comparison of the thermal current for the same system achieved by using TDVP2 and TEBD. The results show very good agreement although TDVP2 needs smaller bond dimensions. (see fig. 41)

The maximum bond dimension for this simulation can be found in fig. 41. Interestingly, TDVP2 almost immediately reaches the maximum bond dimension of 300. The TEBD algorithm at first starts at way lower bond dimensions. However, due to the exponentially increasing bond dimensions, TEBD eventually needs much higher bond dimensions. Therefore, the TDVP2 algorithm was tested for very small bond dimensions to investigate how small maximum bond dimensions can get while the thermal current is still accurately represented.
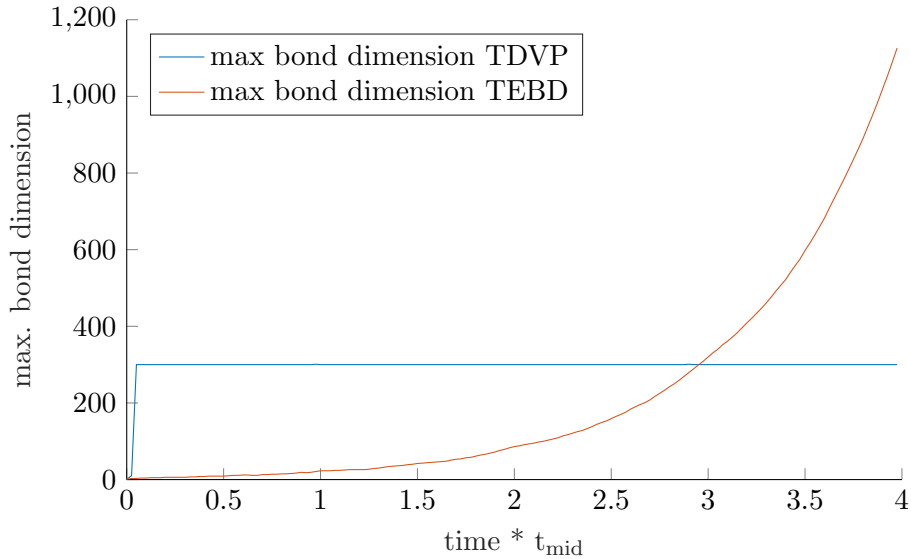
Figure 41: Maximum bond dimension of the simulation depicted in fig. 40 for TEBD and TDVP2.

6.1   Accuracy at small bond dimensions

According to the paper by Leviatan et al.[17], TDVP is able to satisfy certain conservation laws and is therefore able to accurately describe observables, which depend on quantum processes on small scales, even for very small bond dimensions. This approach was at first tested for the two-site TDVP algorithm described in chap. 3.5.3. Here, the relevant observable was the thermal energy current in a tight-binding chain. The simulation was started with $\beta_L = 0.5$ and $\beta_R = 0.0$, both baths consisted of 30 sites. Obviously, quite high temperatures are applied which goes well together with [17] as they also consider systems at high temperatures. The results can be seen in fig. 42 and show that the thermal current is not conserved by the TDVP2 algorithm for small bond dimensions. At very short times, all currents are aligned. As time goes on, the result for the simulation with $\chi = 5$ diverges around $t = 0.5$. Just before $t = 2$, the result for $\chi = 10$ also clearly diverges from the other results and the same is happening to the $\chi = 20$ result at $t = 3$. This clearly shows that the insufficient bond dimension χ causes the thermal current to deviate from the exact result. The smaller the bond dimension is, the earlier the results get useless. Of course, a higher bond dimension results in a more accurate description for longer times as a completely unrestrictedly growing bond dimension would lead to the exact result (with respect to truncation errors, other errors arise due to the Trotter-Suzuki decomposition). Strong oscillations can be seen and the currents are even changing their sign. Even the largest bond dimension of $\chi = 60$ is not large enough to reach the thermal current steady state.
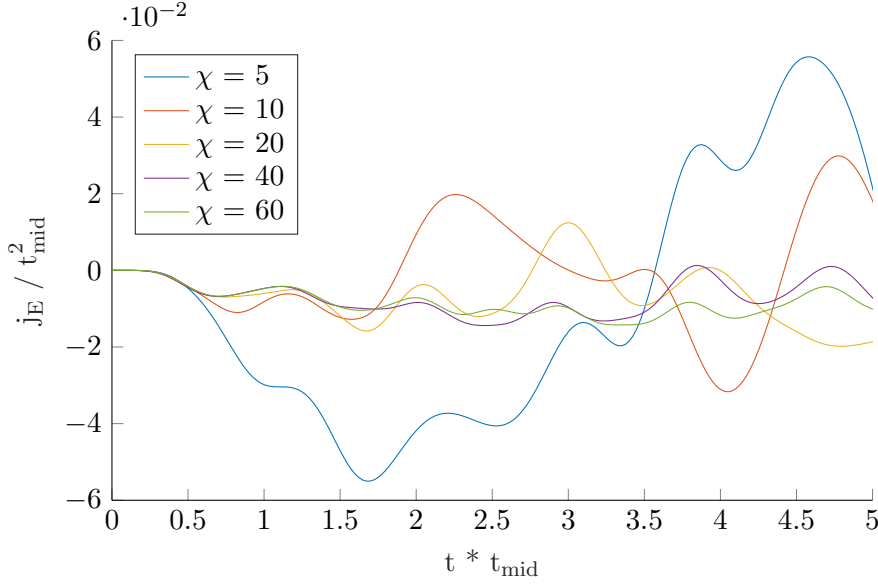
Figure 42: Thermal current for a system with $\beta_L = 0.5$ and $\beta_R = 0.0$ simulated with TDVP2 at very low bond dimensions. Clearly, no steady state current is reached.

The results for very small bond dimensions seem to be completely useless even after very short times. For longer times there is as well no indication whatsoever that those thermal currents would eventually converge towards the same value. This contrasts with the results by Leviatan et al., especially with their idea of a "hydrodynamic long time tail". The thermal current for longer times can bee seen in fig. 48 in chap. A.6 but shows no qualitative difference: The thermal currents for different bond dimensions are oscillating, even reach positive values although a negative steady state current is expected.

As it seemed that the TDVP2 algorithm actually did not conserve the thermal current for small bond dimensions, TEBD, one-site and two-site TDVP were all tested on a smaller system with only 12 bath sites. At first, all three algorithms were applied at sufficient bond dimensions. In the case of TEBD, the truncation error was monitored and the simulation was stopped when the error became larger than 10^{-8}. This usually happened shortly after the maximum bond dimension was reached. In the case of TDVP, the maximum bond dimension was soon reached in the case of two-site TDVP, similar to fig. 41. In the case of one-site TDVP, the bond dimension was given and fixed from the beginning. We found that, in order to run the simulation properly, the first two steps of the one-site TDVP time evolution had to be done with two-site TDVP. The convergence of the results could be checked by repeating the calculation with a higher maximum bond dimension or by comparing the results to TEBD runs for the same initial conditions. Furthermore, the steady state current also turned out to be a good indicator for the convergence of the calculation as the steady state is very sensitive to inaccuracy. Very soon after the calculation gets inaccurate, the measured thermal energy current

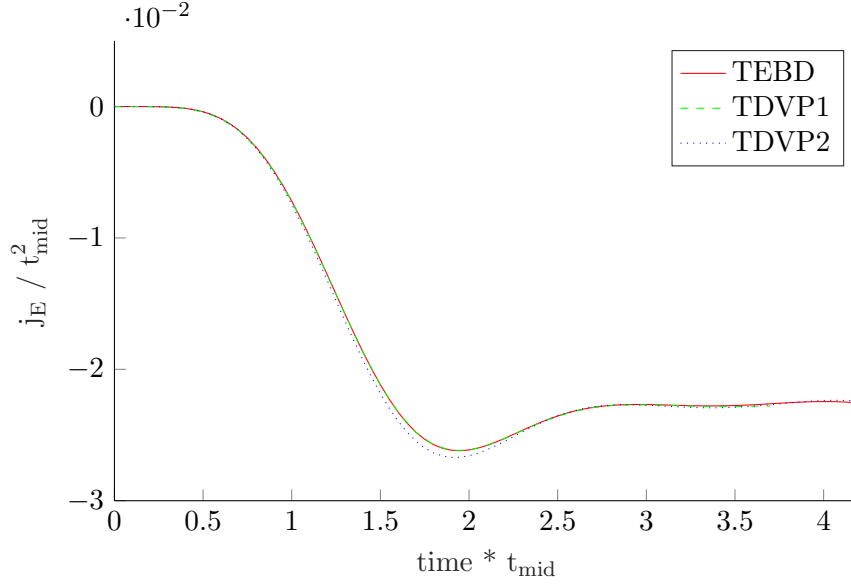will significantly diverge from the steady state value.

Figure 43: Thermal current for a small test system with 12 bath sites ($\beta_L = 0.5$ and $\beta_R = 0.0$) and 3 sites in the middle chain. The thermal current was calculated with TEBD, TDVP1 with a bond dimension of 150 and TDVP2 with a maximum bond dimension of 300.

Fig. 43 shows the thermal current calculated with 3 different time evolution algorithms: TEBD, TDVP1 and TDVP2. While the TEBD reaches matrix dimensions of more than 800 at time $t = 4$, the TDVP simulations run with smaller bond dimensions at the same accuracy and also obtain the correct steady state current.

Now the question arises, whether the steady state thermal energy current of this small system could still be captured for very small bond dimensions in the case of either TDVP1 or TDVP2. Therefore, the simulation was done again, at first for TDVP2 with relatively small maximum bond dimensions ranging from 20 to 300. The results can be seen in fig. 44
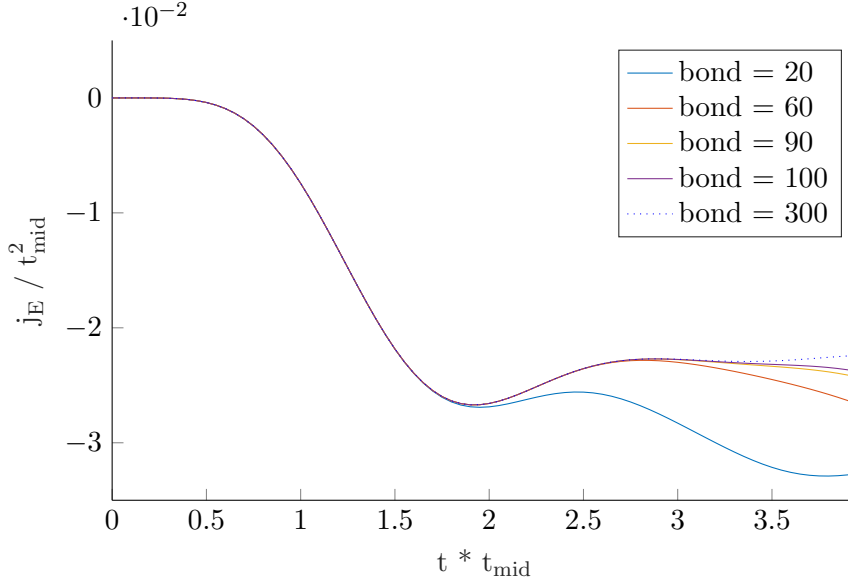
Figure 44: Thermal current for a small test system with 12 bath sites ($\beta_L = 0.5$ and $\beta_R = 0.0$) and 3 sites in the middle chain. The thermal current was calculated with TDVP2 with maximum bond dimensions 20, 60, 90 and 100 and 300.

As one can see, there is no conservation of the steady state current. For small times, all simulations coincide, but for larger times, the small bond dimensions are insufficient to capture the steady state current and the results are getting inaccurate.

However, in [17] there was a one-site TDVP algorithm applied. The major difference between TDVP2 and TDVP1 is that in TDVP2, two sites are time evolved together and later separated by applying an SVD. The appliance of an SVD includes truncation and one could assume that this truncation might destroy the conserving properties of the TDVP algorithm. The results for small bond dimensions using the TDVP1 algorithm can be found in fig. 45.
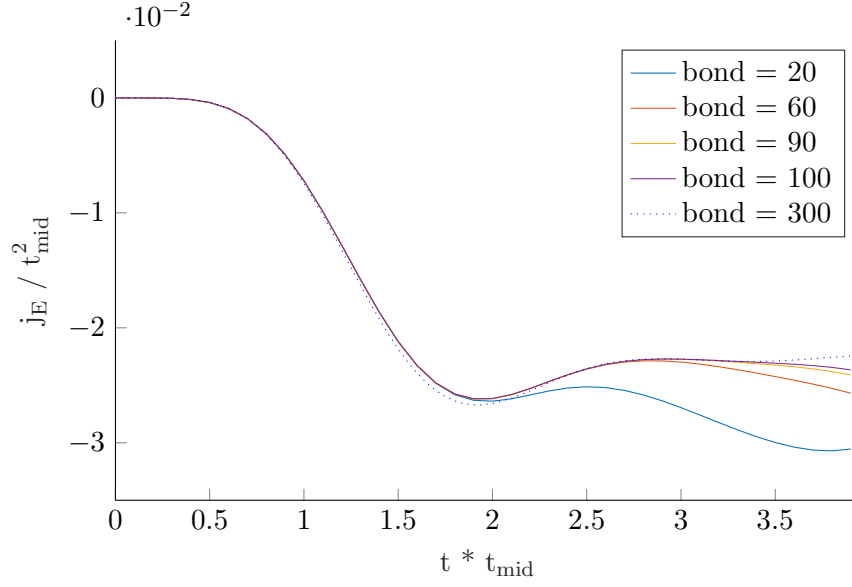
Figure 45: Thermal current for a small test system with 12 bath sites ($\beta_L = 0.5$ and $\beta_R = 0.0$) and 3 sites in the middle chain. The thermal current was calculated with TDVP1 with bond dimensions 20, 60, 90, 100 and 300.

Fig. 45 clearly shows that also for the one-site TDVP algorithm, the thermal current is not a conserved quantity for small bond dimensions. For longer times, the calculations just get more inaccurate, similar to the two-site TDVP algorithm as depicted in fig. 44. One can also see that for the same bond dimension, TDVP1 and TDVP2 obtain results for the steady state current which have the same accuracy.

Both figs. 44 and 45 clearly show that, although the simulation is quite accurate for some time, to simulate the steady state current at larger times, one needs matrix dimensions significantly larger than the ones used in [17], where Leviatan et al. performed time evolutions with very small bond dimensions ranging from $\chi = 2$ to $\chi = 16$.

As a comparison, the same system was now also simulated by applying TEBD at several bond dimensions. The results can bee seen in fig. 46.
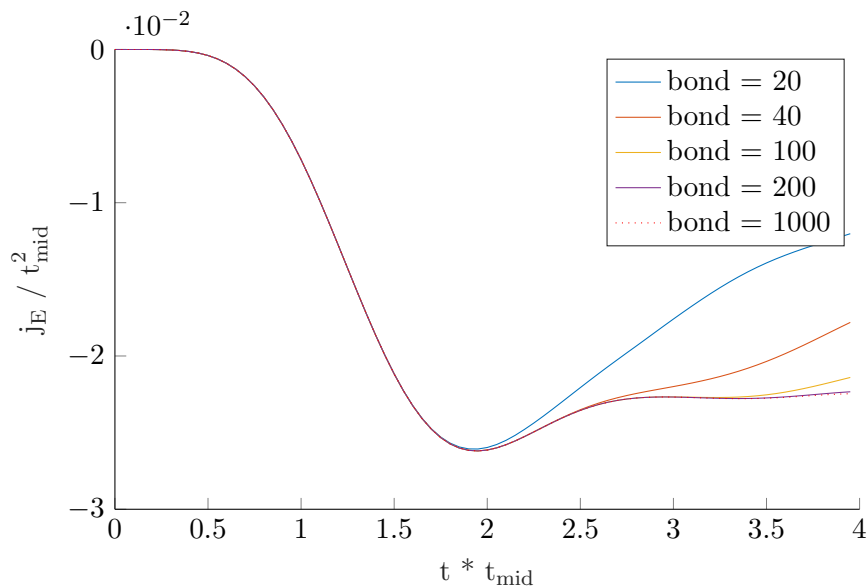
Figure 46: Thermal current for a small test system with 12 bath sites ($\beta_L = 0.5$ and $\beta_R = 0.0$) and 3 sites in the middle chain. The thermal current was calculated with TEBD with maximum bond dimensions 20, 40, 100, 200 and 1000.

As expected, TEBD also delivers inaccurate results for insufficient bond dimensions. One can also see that for such a small system and at short times, the TEBD algorithm can as well deliver results of comparable accuracy to the results obtained by TDVP although the maximum bond dimension was restricted.

Finally, the computation times for the three algorithms and the respective bond dimensions were compared. The results can be found in fig. 47

Figure 47: Computation time for the calculations in figures 44, 45 and 46.

In fig. 47 one can see that the calculations for TDVP1 take an order of magnitude longer than the TDVP2 calculations for the same bond dimensions. This is due to the fact that the TDVP2 algorithm time evolves two sites of the chain at 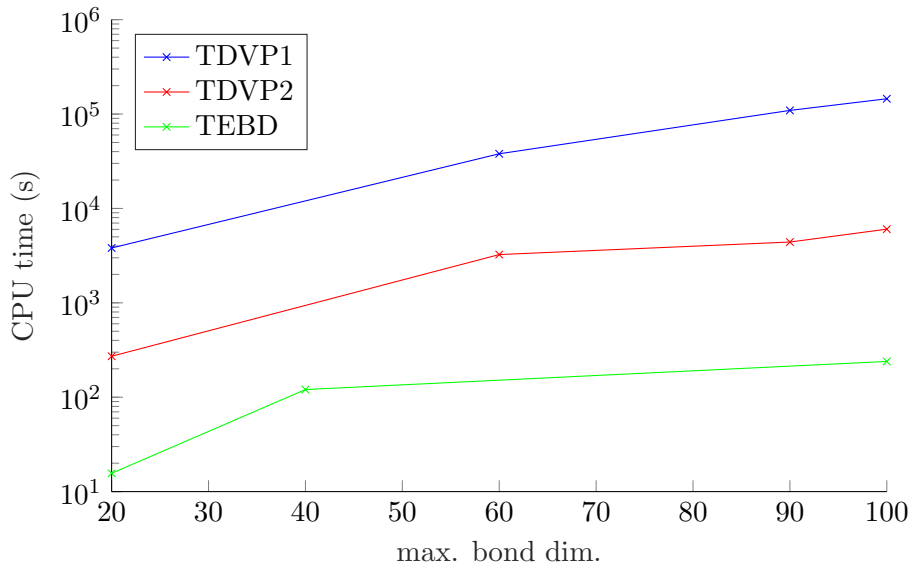once. This is done by multiplying two sites together and separating them with an SVD after the time evolution was performed. Therefore, the TDVP2 algorithm is able to change the bond dimension. However, the TDVP1 algorithm only acts on a single site and can therefore not change any bond dimension. This means that if one chooses a maximum bond dimension of 100, every single bond has to be initialized at bond dimension 100 which massively slows down the calculations.

One can also see that the TEBD algorithm is another order of magnitude faster than the TDVP2 algorithm. This can be understood from fig. 41: While the maximum bond dimension is almost instantly reached in the case of the TDVP2 algorithm, the TEBD algorithm uses way smaller bond dimensions at low times which explains the difference in computation times. Therefore, for small times and small systems, the TEBD algorithm is definitely the better choice. For larger times and larger systems, the TDVP2 algorithm can get more advantageous as it needs smaller bond dimensions while the bond dimensions are exponentially increasing in the case of the TEBD algorithm.

To sum up, the claim by Leviatan et al. that certain quantities are conserved for time evolution applying TDVP even for very small bond dimensions could not be replicated in the case of steady state thermal energy currents flowing between thermal baths. However, both the TDVP1 and TDVP2 algorithm require lower bond dimensions than the TEBD algorithm in order to achieve results at the same accuracy.

In a very recent paper, Kloss et al. also discuss the long time behaviour of TDVP in the context of MPS.[39] They study the convergence of long time observables in integrable

systems and come to the conclusion "that convergence of long time observables is subtle and needs to be examined carefully." However, they conclude that the method "might still be asymptotically accurate for a class of nonintegrable quantum systems." To study such systems, they considered the spreading of a spin-excitation in the one-dimensional XXZ model as a function of time. The results are then averaged over a few hundred initial spin configurations, hoping that the method will on average produce correct results due to the properties of the TDVP algorithm discussed above. They further conclude that the apparent convergence of long time observables like the diffusion coefficient obtained by TDVP does not indicate that the method is accurate and might even be very misleading. They could also find examples where the method failed to deliver correct results, although in other cases like the disordered XXZ model in the ergodic subdiffusive phase, very accurate results for the long time behaviour could be obtained. They finally conclude that one should be very careful when studying the convergence of long time properties within the MPS-TDVP approach. Although the correct long time dynamics could be obtained in a special case, in general one can not draw reliable conclusions from the apparent convergence of transport behaviour. This claim is supported by the results obtained in this chapter.

7   Conclusions

In this thesis, the particle current and the thermal energy current in one-dimensional systems were studied.

The discussion of particle currents can be found in chapter 4.2, where both Wilson chain and star geometries were applied to model baths which were then coupled onto tight-binding and Hubbard chains. Regarding the DOS of the baths, either a constant or a semi-circular DOS were considered. The particle current can either be induced by a different initial filling of the two baths or by applying a bias voltage (see [23]). The growth of the von Neumann entanglement entropy on the first bond of the chain (see figs. 14 and 15) was studied as well as the entanglement entropy throughout the whole system (see figs. 16 and 17). On the first bond of the chain, a linearly growing entanglement entropy could be observed for both geometries. For a bath consisting of a tight-binding chain with constant hopping parameter t, a plateau in time of the entanglement entropy could be observed in fig. 19.

The steady state values for both current and occupation numbers can be seen in figs. 27 and 28. After a short time, the particle current reaches a steady state value which grows with the area of the DOS and is the same for all sites of the chain. The steady state occupation numbers differ throughout the system. The convergence of the entanglement entropy for different bath sizes and bandwidths of the DOS can be seen in fig. 29 for a chain geometry bath and in fig. 30 for star geometry baths.

The steady state current and the entropy for a Hubbard chain on which a bias voltage is applied can bee seen in figs. 31 and 32.

Thermal currents between two baths were studied in [22]. However, instead of applying the commonly used method of purification, in this thesis the thermal baths were modelled by applying a thermofield approach on star geometry baths as presented in [2]. Steady state thermal currents flowing through tight-binding chains for different temperatures of the left bath can be found in fig. 34 and show that the steady state value is only a function of the temperatures of the left bath and the right bath of the form $f(\beta_L) - f(\beta_R)$. After a thermalization time, the steady state is reached but this convergence rate heavily depends on the area of the DOS of the system and therefore on the coupling strength of the bath to the system as shown in fig. 37. In the case of Hubbard chains, due to the presence of particles with both spins, the maximum bond dimensions showed an even faster, exponential growth (see fig. 38) and therefore, the steady state thermal energy current could not be reached within the simulation time which was limited by the maximum bond dimensions (see fig. 39).

Finally, the capability of TDVP1 and TDVP2 to capture thermal currents at (compared to TEBD) small bond dimensions was investigated. Generally, due to the optimal representation of a state at a given bond dimension, TDVP needs smaller bond dimensions for an accurate time evolution as it was shown in fig. 40 and fig. 41, respectively.

However, very small bond dimensions on the order of $\chi = 10$ were insufficient of capturing thermal current steady states as was shown in fig. 42. This was not even possible for small systems as shown in figs. 44 and 45. Thus, the claim by Leviatan et al. [17] that TDVP conserves certain quantities at very small bond dimensions could not be replicated in the case of steady state thermal energy currents flowing through tight-binding chains between two thermal baths. Both the TDVP1 and the TDVP2 algorithm can obtain accurate results for bond dimensions smaller than those needed by the exponentially growing bond dimensions in the case of TEBD. On the other hand, TEBD needs an order of magnitude less computation time than the TDVP2 algorithm as can be seen in fig. 47. TDVP1 needs another order of magnitude more computation time than TDVP2 at the same bond dimension and accuracy, respectively. Therefore, the TEBD algorithm is more advantageous, especially for small systems and short simulation times.

8   Acknowledgements

First of all, I would like to thank my supervisor, Hans Gerd Evertz, for giving me the chance to work on this interesting topic, patiently answering my questions and for ensuring such a pleasant and cooperative atmosphere in our group. I really enjoyed working on my thesis in such a friendly and collegial environment. This is also due to my roommates Daniel Bauernfeind and Florian Maislinger, who are great colleagues and also answered so many questions. I would also like to thank Viktor Eisler for many interesting discussions and Andreas Hirczy for his great support in all IT-related problems.

Thank you to Mama and Papa for making all this possible, for your unconditional love and support and for ensuring such a worriless environment for me which allowed me to focus on physics as much as I wanted to.

And finally, I would like to thank my wonderful girlfriend Antonia. Thank you for your love and for always being there for me.

A   Appendix

A.1   List of appreviations

- **DMRG**: Density Matrix Renormalization Group

- **DOS**: Density Of States

- **MPS**: Matrix Product State

- **MPO**: Matrix Product Operator

- **SIAM**: Single Impurity Anderson Model

- **SVD**: Singular Value Decomposition

- **SvN**: von Neumann entanglement entropy

- **TEBD**: Time-Evolving Block Decimation

- **TDVP**: Time Dependent Variational Principle

- **TDVP1**: One-Site Time Dependent Variational Principle

- **TDVP2**: Two-Site Time Dependent Variational Principle

A.2 Bogoliubov transformation I

We want to calculate expressions of the form

$$e^X Y e^{-X} \tag{144}$$

For these expressions, a serial expansion exists:

$$e^X Y e^{-X} = \sum_{m=0}^{\infty} \frac{1}{m!}[X, Y]_m \tag{145}$$

with

$$[X, Y]_m = [X, [X, Y]_{m-1}] \\ [X, Y]_0 = Y \tag{146}$$

In our case, $X = -iG$ and $Y = b_k$ with $G = i \sum_k \theta_k (b_k^\dagger c_k^\dagger - c_k b_k)$.

Using $[-iG, b_k] = \theta_k c_k^\dagger$ and $[iG, c_k^\dagger] = -\theta_k b_k$, the following results can be obtained

$$[X, Y]_0 = Y$$
$$[X, Y]_1 = [X, [X, Y]_0] = [X, Y] = [-iG, b_k] = -\theta_k c_k^\dagger$$
$$[X, Y]_2 = [X, [X, Y]_1] = [-iG, -\theta_k c_k^\dagger] = \theta_k[iG, c_k^\dagger] = -\theta_k^2 b_k$$
$$[X, Y]_3 = [X, [X, Y]_2] = [-iG, -\theta_k^2 b_k] = \theta_k^2[iG, b_k] = \theta_k^3 c_k^\dagger \tag{147}$$
$$[X, Y]_4 = [X, [X, Y]_3] = [-iG, \theta_k^3 c_k^\dagger] = \theta_k^3[-iG, c_k^\dagger] = \theta_k^4 b_k$$
$$[X, Y]_5 = [X, [X, Y]_4] = [-iG, \theta_k^4 b_k] = \theta_k^4[-iG, b_k] = -\theta_k^5 c_k^\dagger$$
$$[X, Y]_6 = [X, [X, Y]_5] = [-iG, -\theta_k^5 c_k^\dagger] = \theta_k^5[iG, c_k^\dagger] = -\theta_k^6 b_k$$

Putting the results from eq. 147 into eq. 145, one obtains the final result:

$$e^X Y e^{-X} = \sum_{m=0}^{\infty} \frac{1}{m!}[X, Y]_m$$
$$= b_k - \theta_k c_k^\dagger - \frac{1}{2!}\theta_k^2 b_k + \frac{1}{3!}\theta_k^3 c_k^\dagger + \frac{1}{4!}\theta_k^4 b_k - \frac{1}{5!}\theta_k^5 c_k^\dagger - \frac{1}{6!}\theta_k^6 b_k \tag{148}$$
$$= b_k(1 - \frac{1}{2!}\theta_k^2 + \frac{1}{4!}\theta_k^4 - \frac{1}{6!}\theta_k^6 + ...) - c_k^\dagger(\theta_k - \frac{1}{3!}\theta_k^3 + \frac{1}{5!}\theta_k^5 - ...)$$
$$\boxed{e^{-iG} b_k e^{iG} = b_k \cos(\theta_k) - c_k^\dagger \sin(\theta_k)}$$

A.3 Bogoliubov transformation II

Starting from the transformed Hamiltonian

$$\tilde{H} = H_S + \sum_k \omega_k(a_{1k}^\dagger a_{1k} - a_{2k}^\dagger a_{2k}) +$$
$$\sum_k g_{1k}(L^\dagger a_{1k} + a_{1k}^\dagger L) + \sum_k g_{2k}(L a_{2k} + a_{2k}^\dagger L^\dagger) \tag{149}$$

we will transform it backwards using

$$a_{1k} = e^{-iG} b_k e^{iG} = \cos(\theta_k) b_k - \sin(\theta_k) c_k^\dagger$$
$$a_{2k} = e^{-iG} c_k e^{iG} = \cos(\theta_k) c_k + \sin(\theta_k) b_k^\dagger \tag{150}$$

where $g_{1k} = g_k \cos(\theta_k)$ and $g_{2k} = -g_k \sin(\theta_k)$. Transformation of the first part gives

$$a_{1k}^\dagger a_{1k} - a_{2k}^\dagger a_{2k} = (\cos(\theta_k) b_k^\dagger - \sin(\theta_k) c_k)(\cos(\theta_k) b_k - \sin(\theta_k) c_k^\dagger) -$$
$$(\cos(\theta_k) c_k^\dagger + \sin(\theta_k) b_k)(\cos(\theta_k) c_k + \sin(\theta_k) b_k^\dagger)$$
$$= \cos^2(\theta_k)(b_k^\dagger b_k - c_k^\dagger c_k) + \sin^2(\theta_k)(c_k c_k^\dagger - b_k b_k^\dagger) +$$
$$\sin(\theta_k)\cos(\theta_k)(-b_k^\dagger c_k^\dagger - c_k b_k + c_k^\dagger b_k^\dagger + b_k c_k) \tag{151}$$

Using the fermionic commutator relations, namely $c_k c_k^\dagger = 1 - c_k^\dagger c_k$,

$$\cos^2(\theta_k)(b_k^\dagger b_k - c_k^\dagger c_k) + \sin^2(\theta_k)(b_k^\dagger b_k - c_k^\dagger c_k) =$$
$$b_k^\dagger b_k - c_k^\dagger c_k \tag{152}$$

This gives the final transformation of the first part:

$$\boxed{\sum_k \omega_k(a_{1k}^\dagger a_{1k} - a_{2k}^\dagger a_{2k}) = \sum_k \omega_k(b_k^\dagger b_k - c_k^\dagger c_k)} \tag{153}$$

The transformation of the second part gives

$$g_{1k}(L^\dagger a_{1k} + a_{1k}^\dagger L) + g_{2k}(L a_{2k} + a_{2k}^\dagger L^\dagger) =$$
$$g_k \cos(\theta_k)(L^\dagger(\cos(\theta_k) b_k - \sin(\theta_k)) c_k^\dagger + (\cos(\theta_k) b_k^\dagger - \sin(\theta_k) c_k) L) -$$
$$g_k \sin(\theta_k)(L(\cos(\theta_k) c_k + \sin(\theta_k) b_k^\dagger) + (\cos(\theta_k) c_k^\dagger + \sin(\theta_k) b_k) L^\dagger) =$$
$$g_k(\cos^2(\theta_k)(L^\dagger b_k + b_k^\dagger L) + \sin^2(\theta_k)(L b_k^\dagger + b_k L^\dagger) +$$
$$\sin(\theta_k)\cos(\theta_k)(-L^\dagger c_k^\dagger - c_k L + L c_k + c_k^\dagger L^\dagger) =$$
$$g_k(L^\dagger b_k + b_k^\dagger L) \tag{154}$$

Therefore,

$$\boxed{\sum_k g_{1k}(L^\dagger a_{1k} + a_{1k}^\dagger L) + \sum_k g_{2k}(L a_{2k} + a_{2k}^\dagger L^\dagger) = \sum_k g_k(L^\dagger b_k + b_k^\dagger L)} \tag{155}$$

A.4 Thermal vacuum verification

The thermal vacuum is given by

$$|\Omega\rangle \propto e^{-\beta H_B/2} |I\rangle \tag{156}$$

where $|I\rangle = \sum_n |n\rangle_b |n\rangle_c = |0\rangle_b |0\rangle_c + |1\rangle_b |1\rangle_c$ for fermions. H_B is given by

$$H_B = \sum_k \omega_k b_k^\dagger b_k \tag{157}$$

For this proof, we will only consider a fixed k value and show that applying a_{1k} to that state is equal to zero. Using only one k value, the thermal vacuum reads

$$e^{-\beta \omega_k b_k^\dagger b_k/2}(|0\rangle_b |0\rangle_c + |1\rangle_b |1\rangle_c) =$$
$$(1 + \sum_{m=1}^{\infty} (-\frac{\beta}{2}\omega_k b_k^\dagger b_k)^m)(|0\rangle_b |0\rangle_c + |1\rangle_b |1\rangle_c) \tag{158}$$

Now we can apply the two parts of $a_{1k} = cos(\theta_k)b_k - sin(\theta_k)c_k^\dagger$:

$$\cos(\theta_k)b_k |\Omega\rangle =$$
$$\cos(\theta_k)b_k(1 + \sum_{m=1}^{\infty}(-\frac{\beta}{2}\omega_k b_k^\dagger b_k)^m)(|0\rangle_b |0\rangle_c + |1\rangle_b |1\rangle_c) =$$
$$\cos(\theta_k)b_k(1 - \frac{\beta}{2}\omega_k b_k^\dagger b_k + 1/2(-\frac{\beta}{2}\omega_k b_k^\dagger b_k) + ...)(|0\rangle_b |0\rangle_c + |1\rangle_b |1\rangle_c) =$$
$$\cos(\theta_k)b_k(|0\rangle_b |0\rangle_c + |1\rangle_b |1\rangle_c - \frac{\beta}{2}\omega_k |1\rangle_b |1\rangle_c + 1/2(-\frac{\beta}{2}\omega_k)^2 |1\rangle_b |1\rangle_c + ...) = \tag{159}$$
$$\cos(\theta_k)b_k(|0\rangle_b |0\rangle_c + e^{-\frac{\beta}{2}\omega_k} |1\rangle_b |1\rangle_c) =$$
$$\cos(\theta_k)b_k e^{-\frac{\beta}{2}\omega_k} |1\rangle_b |1\rangle_c =$$
$$\cos(\theta_k)e^{-\frac{\beta}{2}\omega_k} |0\rangle_b |1\rangle_c$$

$$\sin(\theta_k)c_k^\dagger |\Omega\rangle =$$
$$\sin(\theta_k)c_k^\dagger(|0\rangle_b |0\rangle_c + e^{-\frac{\beta}{2}\omega_k} |1\rangle_b |1\rangle_c) =$$
$$\sin(\theta_k)c_k^\dagger |0\rangle_b |0\rangle_c = \tag{160}$$
$$\sin(\theta_k)c_k^\dagger |0\rangle_b |1\rangle_c$$

Combining these two parts, we obtain

$$
\begin{aligned}
a_{1k} \left| \Omega \right\rangle &= \left(\cos(\theta_k) e^{-\frac{\beta}{2}\omega_k} - \sin(\theta_k) \right) \left| 0 \right\rangle_b \left| 1 \right\rangle_c \\
&= \left(\sqrt{1 - n_k} e^{-\frac{\beta}{2}\omega_k} - \sqrt{n_k} \right) \left| 0 \right\rangle_b \left| 1 \right\rangle_c \\
&= \left(\sqrt{1 - \frac{1}{e^{\beta\omega_k} + 1}} e^{-\frac{\beta}{2}\omega_k} - \sqrt{\frac{1}{e^{\beta\omega_k} + 1}} \right) \left| 0 \right\rangle_b \left| 1 \right\rangle_c \\
&= \left(\sqrt{e^{-\beta\omega_k} - \frac{e^{-\beta\omega_k}}{e^{\beta\omega_k} + 1}} - \sqrt{\frac{1}{e^{\beta\omega_k} + 1}} \right) \left| 0 \right\rangle_b \left| 1 \right\rangle_c \\
&= \left(\sqrt{\frac{e^{-\beta\omega_k} + 1}{e^{\beta\omega_k} + 1} - \frac{e^{-\beta\omega_k}}{e^{\beta\omega_k} + 1}} - \sqrt{\frac{1}{e^{\beta\omega_k} + 1}} \right) \left| 0 \right\rangle_b \left| 1 \right\rangle_c \\
&= \left(\sqrt{\frac{1}{e^{\beta\omega_k} + 1}} - \sqrt{\frac{1}{e^{\beta\omega_k} + 1}} \right) \left| 0 \right\rangle_b \left| 1 \right\rangle_c
\end{aligned}
\tag{161}
$$

$$\boxed{a_{1k} \left| \Omega \right\rangle = 0}$$

As the different k values commute with each other, showing this relation for a single k is sufficient to show that eq. 156 is also a representation of the thermal vacuum.

Appendix

A.5 Energy current calculation

The energy current is defined by

$$j_{E,n} = i[h_{n+1}, h_n] \tag{162}$$

If we only consider the tight binding contribution in eq. 118, h_n is given by

$$\begin{aligned}
h_n &= -\frac{t_0}{2}(c_{n\uparrow}^\dagger c_{n+1\uparrow} + c_{n\downarrow}^\dagger c_{n+1\downarrow} + H.c.) \\
&= -\frac{t_0}{2}\sum_\sigma(\underbrace{c_{n\sigma}^\dagger c_{n+1\sigma}}_{:=M_{n\sigma}} + H.c.) \\
&= -\frac{t_0}{2}\sum_\sigma(M_{n\sigma} + M_{n\sigma}^\dagger)
\end{aligned} \tag{163}$$

Therefore, the energy current reads

$$j_{E,n} = i[h_{n+1}, h_n] = \sum_{\sigma\sigma'} i\frac{t_0^2}{4}[M_{n+1\sigma} + M_{n+1\sigma}^\dagger, M_{n\sigma'} + M_{n\sigma'}^\dagger] \tag{164}$$

The first contribution to j_n reads

$$[M_{n+1\sigma}, M_{n\sigma'}] = [c_{n+1\sigma}^\dagger c_{n+2\sigma}, c_{n\sigma'}^\dagger c_{n+1\sigma'}] \tag{165}$$

Using $[AB, C] = [A, C]B + A[B, C]$ and $[C, AB] = \{C, A\}B - A\{C, B\}$, this leads to

$$\begin{aligned}
[c_{n+1\sigma}^\dagger c_{n+2\sigma}, c_{n\sigma'}^\dagger c_{n+1\sigma'}] &= \\
[c_{n+1\sigma}^\dagger, c_{n\sigma'}^\dagger c_{n+1\sigma'}]c_{n+2\sigma} + c_{n+1\sigma}^\dagger \underbrace{[c_{n+2\sigma}, c_{n\sigma'}^\dagger c_{n+1\sigma'}]}_{=0} &= \\
(\underbrace{\{c_{n+1\sigma}^\dagger, c_{n\sigma'}^\dagger\}}_{=0} c_{n+1\sigma'} - c_{n\sigma'}^\dagger \underbrace{\{c_{n+1\sigma}^\dagger, c_{n+1\sigma'}\}}_{\delta_{\sigma\sigma'}})c_{n+2\sigma} &= \\
[M_{n+1\sigma}, M_{n\sigma'}] = -c_{n\sigma'}^\dagger c_{n+2\sigma}\delta_{\sigma\sigma'} &
\end{aligned} \tag{166}$$

If $[A, B] = C$ then $[A^\dagger, B^\dagger] = -C^\dagger$ and therefore

$$[M_{n+1\sigma}^\dagger, M_{n\sigma'}^\dagger] = c_{n+2\sigma}^\dagger c_{n\sigma'}\delta_{\sigma\sigma'} \tag{167}$$

A similar calculation leads to

$$\begin{aligned}
[M_{n+1\sigma}^\dagger, M_{n\sigma'}] &= [c_{n+2\sigma}^\dagger c_{n+1\sigma}, c_{n\sigma'}^\dagger c_{n+1\sigma'}] \\
&= \underbrace{[c_{n+2\sigma}^\dagger, c_{n\sigma'}^\dagger c_{n+1\sigma'}]}_{=0} c_{n+1\sigma} + c_{n+2\sigma}^\dagger[c_{n+1\sigma}, c_{n\sigma'}^\dagger c_{n+1\sigma'}] \\
&= c_{n+2\sigma}^\dagger(\underbrace{\{c_{n+1\sigma}, c_{n\sigma'}^\dagger\}}_{=0} c_{n+1\sigma'} - c_{n\sigma'}^\dagger \underbrace{\{c_{n+1\sigma}, c_{n+1\sigma'}\}}_{=0}) \\
&= 0
\end{aligned} \tag{168}$$

84

Appendix

Therefore, $[M_{n+1\sigma}, M^{\dagger}_{n\sigma'}] = 0$ and eq. 164 simplifies to

$$
\begin{aligned}
j_{E,n} &= i\frac{t_0^2}{4}[h_{n+1}, h_n] \\
&= \sum_{\sigma\sigma'} i[M_{n+1\sigma} + M^{\dagger}_{n+1\sigma}, M_{n\sigma'} + M^{\dagger}_{n\sigma'}] \\
&= \sum_{\sigma\sigma'} i\frac{t_0^2}{4}([M_{n+1\sigma}, M_{n\sigma'}] + [M^{\dagger}_{n+1\sigma}, M^{\dagger}_{n\sigma'}]) \\
&= \sum_{\sigma\sigma'} i\frac{t_0^2}{4}(-c^{\dagger}_{n\sigma'}c_{n+2\sigma}\delta_{\sigma\sigma'} + c^{\dagger}_{n+2\sigma}c_{n\sigma'}\delta_{\sigma\sigma'}) \\
&= \sum_{\sigma} i\frac{t_0^2}{4}(c^{\dagger}_{n+2\sigma}c_{n\sigma} - c^{\dagger}_{n\sigma}c_{n+2\sigma})
\end{aligned}
\tag{169}
$$

$$
\boxed{j_{E,n} = \sum_{\sigma} i\frac{t_0^2}{4}(c^{\dagger}_{n+2\sigma}c_{n\sigma} - H.c.)}
$$

The same result can be found for example in [25].
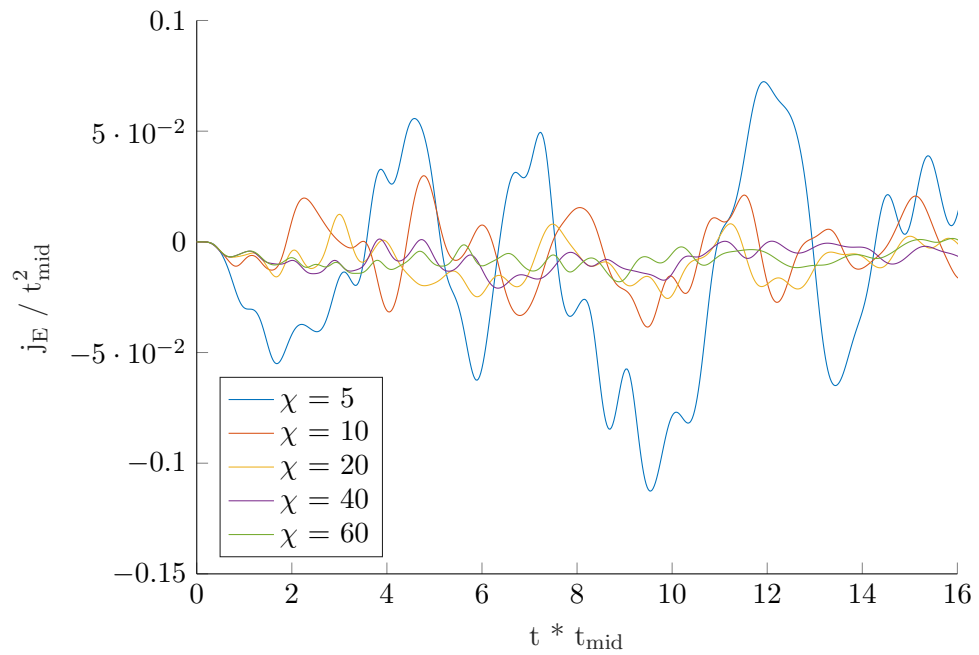
A.6 Thermal current at small bond dimensions

Figure 48: Thermal current for a system with $\beta_L = 0.5$ and $\beta_R = 0.0$ simulated with TDVP2 at very low bond dimensions for long times. Clearly, no steady state current is reached, even for longer simulation times.

References

[1] U. Schollwöck. The density-matrix renormalization group in the age of matrix product states. *Annals of Physics* 326, 96 (2011).

[2] I. de Vega and M.-C. Bañuls. Thermofield-based chain-mapping approach for open quantum systems. *Physical Review A* 92, 052116 (2015).

[3] G. Vidal. Efficient classical simulation of slightly entangled quantum computations. *Physical Review Letters* 91, 147902 (2003).

[4] J. Haegeman, C. Lubich, I. Oseledets, B. Vandereycken, and F. Verstraete. Unifying time evolution and optimization with matrix product states. *Physical Review B* 94, 165116 (2016).

[5] R. Baxter. Exactly Solved Models in Statistical Mechanics, 1982 Academic Press. *San Diego.*

[6] T. Giamarchi. *Quantum physics in one dimension* (Oxford university press, 2004).

[7] F. H. Essler, H. Frahm, F. Göhmann, A. Klümper, and V. E. Korepin. *The one-dimensional Hubbard model* (Cambridge University Press, 2005).

[8] W. Nolting. *Grundkurs Theoretische Physik 7: Viel-Teilchen-Theorie* (Springer-Verlag, 2014).

[9] P. Calabrese and J. Cardy. Entanglement entropy and quantum field theory. *Journal of Statistical Mechanics: Theory and Experiment* 2004, P06002 (2004).

[10] F. Heidrich-Meisner, A. E. Feiguin, and E. Dagotto. Real-time simulations of nonequilibrium transport in the single-impurity Anderson model. *Physical Review B* 79, 235336 (2009).

[11] Z. He and A. J. Millis. Entanglement entropy and computational complexity of the Anderson impurity model out of equilibrium: Quench dynamics. *Phys. Rev. B* 96, 085107 (2017).

[12] V. Alba and F. Heidrich-Meisner. Entanglement spreading after a geometric quench in quantum spin chains. *Phys. Rev. B* 90, 075144 (2014).

[13] S. R. White. Density matrix formulation for quantum renormalization groups. *Physical Review Letters* 69, 2863 (1992).

[14] M. J. Ganahl. Dynamics of Strongly Correlated One-Dimensional Quantum Systems using Matrix Product States. PhD thesis (Graz University of Technology, 2014).

[15] G. Vidal. Efficient simulation of one-dimensional quantum many-body systems. *Physical Review Letters* 93, 040502 (2004).

[16] F. Maislinger. A Comparison of Recently Developed Time-Evolution Algorithms for One-Dimensional Systems with Long-Range Interactions. MA thesis (Graz University of Technology, 2016).

[17] E. Leviatan, F. Pollmann, J. H. Bardarson, and E. Altman. Quantum thermalization dynamics with matrix-product states. *arXiv preprint arXiv:1702.08894* (2017).

[18] F. A. Wolf, I. P. McCulloch, and U. Schollwöck. Solving nonequilibrium dynamical mean-field theory using matrix product states. *Physical Review B* 90, 235131 (2014).

[19] K. G. Wilson. The renormalization group: Critical phenomena and the Kondo problem. *Reviews of Modern Physics* 47, 773 (1975).

[20] R. Bulla, T. A. Costi, and T. Pruschke. Numerical renormalization group method for quantum impurity systems. *Reviews of Modern Physics* 80, 395 (2008).

[21] D. Bauernfeind, M. Zingl, R. Triebl, M. Aichhorn, and H. G. Evertz. Fork Tensor-Product States: Efficient Multiorbital Real-Time DMFT Solver. *Physical Review X* 7, 031013 (2017).

[22] C. Karrasch. Nonequilibrium thermal transport and vacuum expansion in the Hubbard model. *Physical Review B* 95, 115148 (2017).

[23] F. Heidrich-Meisner, I. González, K. Al-Hassanieh, A. Feiguin, M. Rozenberg, and E. Dagotto. Nonequilibrium electronic transport in a one-dimensional Mott insulator. *Physical Review B* 82, 205110 (2010).

[24] C. A. Büsser and F. Heidrich-Meisner. Inducing Spin Correlations and Entanglement in a Double Quantum Dot through Nonequilibrium Transport. *Phys. Rev. Lett.* 111, 246807 (2013).

[25] X. Zotos, F. Naef, and P. Prelovsek. Transport and conservation laws. *Physical Review B* 55, 11029 (1997).

[26] C. Karrasch, R. Ilan, and J. Moore. Nonequilibrium thermal transport and its relation to linear response. *Physical Review B* 88, 195129 (2013).

[27] C. Karrasch, J. Bardarson, and J. Moore. Reducing the numerical effort of finite-temperature density matrix renormalization group calculations. *New Journal of Physics* 15, 083031 (2013).

[28] R. Vasseur, C. Karrasch, and J. E. Moore. Expansion Potentials for Exact Far-from-Equilibrium Spreading of Particles and Energy. *Phys. Rev. Lett.* 115, 267201 (2015).

[29] A. Sologubenko, T. Lorenz, H. Ott, and A. Freimuth. Thermal conductivity via magnetic excitations in spin-chain materials. *Journal of Low Temperature Physics* 147, 387 (2007).

[30] N. Hlubek, P. Ribeiro, R. Saint-Martin, A. Revcolevschi, G. Roth, G. Behr, B. Büchner, and C. Hess. Ballistic heat transport of quantum spin excitations as seen in SrCuO 2. *Physical Review B* 81, 020405 (2010).

[31] N. Motoyama, H. Eisaki, and S. Uchida. Magnetic susceptibility of ideal spin 1/2 Heisenberg antiferromagnetic chain systems, Sr 2 CuO 3 and SrCuO 2. *Physical Review Letters* 76, 3212 (1996).

REFERENCES

[32] L. Arrachea, G. S. Lozano, and A. Aligia. Thermal transport in one-dimensional spin heterostructures. *Physical Review B* 80, 014425 (2009).

[33] A. Dhar. Heat transport in low-dimensional systems. *Advances in Physics* 57, 457 (2008).

[34] F. Jin, R. Steinigeweg, F. Heidrich-Meisner, K. Michielsen, and H. De Raedt. Finite-temperature charge transport in the one-dimensional Hubbard model. *Physical Review B* 92, 205103 (2015).

[35] C. Karrasch, D. Kennes, and F. Heidrich-Meisner. Thermal conductivity of the one-dimensional Fermi-Hubbard model. *Physical Review Letters* 117, 116401 (2016).

[36] G. Edge, R. Anderson, D. Jervis, D. McKay, R. Day, S. Trotzky, and J. Thywissen. Imaging and addressing of individual fermionic atoms in an optical lattice. *Physical Review A* 92, 063406 (2015).

[37] L. W. Cheuk, M. A. Nichols, K. R. Lawrence, M. Okan, H. Zhang, and M. W. Zwierlein. Observation of 2D fermionic Mott insulators of K 40 with single-site resolution. *Physical Review Letters* 116, 235301 (2016).

[38] F. Schwarz, I. Weymann, J. von Delft, and A. Weichselbaum. Nonequilibrium Steady-State Transport in Quantum Impurity Models: a Thermofield and Quantum Quench Approach using Matrix Product States. *arXiv preprint arXiv:1708.06315* (2017).

[39] B. Kloss, Y. B. Lev, and D. Reichman. Time-dependent variational principle in matrix-product state manifolds: pitfalls and potential. *arXiv preprint arXiv:1710.09378* (2017).